

Ph.D. DISSERTATION / TESIS DOCTORAL

**CHARACTERIZATION OF ATMOSPHERIC
AEROSOL PARTICLES USING IN-SITU
TECHNIQUES: OPTICAL, CHEMICAL AND
HYGROSCOPIC PROPERTIES.**

Author:

GLORIA TITOS VELA



Universidad de Granada

Programa de Doctorado en Física y Ciencias del Espacio



Grupo Física de la Atmósfera



Centro Andaluz de Medio Ambiente

UNIVERSIDAD DE GRANADA
DEPARTAMENTO DE FÍSICA APLICADA
GRUPO DE FÍSICA DE LA ATMÓSFERA
TESIS DOCTORAL

**CHARACTERIZATION OF ATMOSPHERIC AEROSOL PARTICLES
USING IN-SITU TECHNIQUES: OPTICAL, CHEMICAL AND
HYGROSCOPIC PROPERTIES.**

Tesis presentada por Gloria Titos Vela para optar al grado de Doctor.

Directores de Tesis:

Dr. Lucas Alados Arboledas
Catedrático de la UGR
Dep. Física Aplicada
Univ. de Granada

Dr. Hassan Lyamani
Investigador de la UGR
Dep. Física Aplicada
Univ. de Granada

Dra. Inmaculada Foyo Moreno
Profesora Titular de la UGR
Dep. Física Aplicada
Univ. de Granada

Granada, Diciembre de 2014

El trabajo de investigación que se expone en la presente memoria, titulado: **CHARACTERIZATION OF ATMOSPHERIC AEROSOL PARTICLES USING IN-SITU TECHNIQUES: OPTICAL, CHEMICAL AND HYGROSCOPIC PROPERTIES**, para aspirar al grado de Doctor en Física que presenta Gloria Titos Vela, ha sido realizado en la Universidad de Granada gracias a la beca concedida por el Ministerio de Economía y Competitividad “Formación de Personal Investigador” (convocatoria 2011), bajo la dirección de:

VºBº los Directores:

Dr. LUCAS ALADOS ARBOLEDAS

Dr. HASSAN LYAMANI

Dra. INMACULADA FOYO MORENO

La doctoranda:

Lda. GLORIA TITOS VELA

La doctoranda Gloria Titos Vela y los directores de la tesis Lucas Alados Arboledas, Hassan Lyamani e Inmaculada Foyo Moreno garantizamos, al firmar esta tesis doctoral, que el trabajo ha sido realizado por la doctoranda bajo la dirección de los directores de la tesis y hasta donde nuestro conocimiento alcanza, en la realización del trabajo, se han respetado los derechos de otros autores a ser citados, cuando se han utilizado sus resultados o publicaciones.

Granada, Diciembre de 2014

Directores de la Tesis

Fdo.: Dr. Lucas Alados Arboledas

Fdo.: Dr. Hassan Lyamani

Fdo.: Dra. Inmaculada Foyo
Moreno

Doctoranda:

Fdo.: Gloria Titos Vela

A mi familia

Success is not the key to happiness.

Happiness is the key to success.

If you love what you are doing, you will be successful

Albert Schweitzer

Acknowledgments / Agradecimientos

Creo que no ha habido ni una sola tesis que haya leído (u ojeado, todo hay que decirlo) en los últimos años y que no empiece los agradecimientos diciendo lo difícil que resulta escribir estas líneas (incluso más que la propia tesis!!!). Anda, anda... ¿Serán exagerados? Es lo que siempre pensaba al leerlo. Pues bien, aquí estoy yo, después de un par de horas, con sólo 5 líneas escritas... y encima cayendo en los tópicos...

Lo primero es lo primero, y allá voy: quiero dar las gracias a mis directores de tesis Lucas, Hassan e Inma, sin ellos esta tesis no hubiese sido posible. A Lucas le quiero agradecer que confiara en mí desde el primer momento y me acogiese en la familia del GFAT. Admiro tu devoción y dedicación infatigable por la investigación y la enseñanza y que sepas sacar tiempo de donde no lo hay para todos los GFATies, especialmente para tus becarios. A Hassan quiero agradecerle todo lo que me ha enseñado sobre la instrumentación y sobre los aerosoles, pero sobre todo le agradezco el haberme enseñado a mirar con ojo crítico cada dato y cada palabra de un artículo, a cuestionarme cada afirmación de cada trabajo, en definitiva, a ser mejor científica. A Inma le quiero agradecer su alegría y optimismo en el día a día, y sobre todo, que hace aproximadamente 4 años me propusiese hacer el doctorado. Era una opción que no contemplaba, y gracias a eso estoy hoy aquí.

Mis directores han sido las personas más vinculadas al desarrollo de esta tesis, pero no las únicas. Quiero darles las gracias a los Profesores Andrés Alastuey y Xavier Querol así como al resto de su grupo del IDAEA-CSIC por su colaboración a lo largo de estos años, especialmente a Andrés por estar

siempre disponible para echar una mano con la química y contestar mis infinitas preguntas. También quiero dar las gracias al Dr. Marco Pandolfi por su ayuda en esta tesis con la técnica PMF. I switch to English to thank Prof. Alfred Wiedensohler for offering me the opportunity to join his group for a few months and improve the humidified nephelometer at TROPOS. I am greatly acknowledged for his help and kindness. I would like to thank also the AERO group of ESRL-NOAA (Dr. Patrick Sheridan, Dr. John Ogren, Dr. Betsy Andrews, Dr. Anne Jefferson and Derek Hageman). They kindly hosted me during my 4 months stay in Boulder as if I were one of their team. Special thanks to John for our extended and regular discussion about aerosol hygroscopicity and for offering me the opportunity to join him for the annual maintenance at Storm Peak. During my stay in Boulder I grew up both scientifically and personally. Aunque no directamente relacionado con esta tesis, pero sí con mi formación investigadora, quiero dar las gracias a los integrantes de la REDMAAS. Durante las campañas he aprendido muchísimo sobre SMPS, DMA, secadores...etc, pero sobre todo hemos reído, disfrutado y pasado muy buenos momentos.

Llega el turno de darle las gracias a mis queridos GFATies. Sin ellos, indudablemente, esta tesis no hubiese sido posible. Son los que han hecho que venir al CEAMA cada día haya sido mucho más que venir a trabajar. Las comidas, las sobremesas y los seminarios de los viernes (bien hayan sido en la sala de seminarios o en la Cabaña) son los que hacen del GFAT esa gran familia que es, y que espero que siga siendo por muchos años. Las comidas no serían lo que son sin Juan Antonio: mil gracias por alargarme la vida con tus chistes, bromas y risas, y por estar siempre disponible para ayudarme con el Word y el Matlab y evitar que el ordenador (o yo) acabásemos precipitándonos por la ventana... Gracias Penélope por tu optimismo y buen hacer, ya te lo he dicho

otras veces, eres mi modelo de mujer-investigadora y, aunque seas de ambientales, de mayor quiero ser como tú. Gracias a Juanlu, Enrique, Ana y Antonio por estar siempre disponibles para echar una mano (y unas buenas risas). Quiero dar las gracias a Andy, Paco Pepe e Inma Alados, por aportar su experiencia y sus buenos comentarios y consejos durante los seminarios. Gracias a Mar por su colaboración y por los buenos momentos que hemos pasado tanto en Granada como en El Arenosillo. No me olvido de los GFATies que están fomentando la «movilidad exterior»: Fran, Óscar y Dani. Con Fran lo que me une no es simplemente compañerismo, es amistad. Han sido muchos, muchísimos, los buenos momentos que hemos compartido dentro y fuera del CEAMA. Hablar de buenos momentos sin hablar de Manuel Antón, es imposible. Manuel instauró los famosos «san manueles», que tantos dolores de cabeza (en el sentido literal) nos causaron. Manuel, te echamos de menos, pero hemos ganado en salud. Quiero darle las gracias a Ana Calvo, por hacer que la estancia en Leipzig fuese más llevadera, lo que nos pudimos reír... Agradecer a los que han pasado por el GFAT a lo largo de estos años, especialmente a Roberto, y a los nuevos fichajes, Pablo y Juan Andrés. Quiero agradecer a Marian, Luis y Juan Alfredo su ayuda burocrática, administrativa e informática a lo largo de estos años y al equipo de mantenimiento de la UGR, especialmente a Fran, por estar siempre disponibles para echar una mano acompañada de alegría y buen humor. Como bien dicen, lo bueno se reserva para el final: quiero agradecer a María José, mi flor, su apoyo y amistad incondicional desde que nos conocemos. Venir a trabajar cada día, y a la vez estar con tu mejor amiga, no tiene precio.

La familia es un pilar fundamental en mi vida. Como Fran siempre me decía: «soy muy familiar». Por eso quiero agradecer y dedicar este trabajo a mi familia, que son los que me han apoyado y acompañado a lo largo de toda mi

existencia. Aunque muchas veces no hayan entendido muy bien mis decisiones, mis padres y mi hermana siempre han estado a mi lado apoyándome de forma incondicional. No puedo dejar de dedicarle unas líneas a mi sobrino, Mario, que ha llenado nuestras vidas de una alegría y felicidad inimaginables.

Más de uno leyendo estas líneas se habrá dado cuenta de dos cosas: la primera y obvia, que tengo mucho rollo, y la segunda, que parece como que falta alguien en estos agradecimientos. Y así es, falta Alberto, y la verdad es que no sabía muy bien dónde ponerlo... y es que Alberto es mi compañero de trabajo, mi amigo y mi familia. Gracias por ayudarme con esta tesis, por tu ayuda con Matlab y con el inglés. Pero sobre todo, gracias por estar siempre a mi lado, por comprenderme siempre y apoyarme en todo momento.

Contents

Abstract.....	1
Resumen	5
1 Introduction	9
1.1 Objectives and outline	16
2 Fundamentals	19
2.1 Atmospheric aerosols: Types, sources and processes affecting aerosol particles.	21
2.2 How anthropogenic aerosols affect visibility, human health and climate?	24
2.3 Interactions of light with particles.....	27
2.4 Water uptake by aerosol particles	31
2.5 History and development of humidified nephelometers	33
2.6 Parameterizations of $f(RH)$	39
2.7 Possible sources of discrepancy among $f(RH)$ measurements	41
2.7.1 Losses in the humidification system	41
2.7.2 Effect of RH measurements on $f(RH)$	42
2.7.3 Different set point and reference RH values	44
3 Experimental site and instrumentation.....	45
3.1 Site description.....	47
3.2 Integrating nephelometer: working principle and calibration procedure.....	48
3.2.1 Nephelometer data correction	51
3.3 Custom-built humidified nephelometer	52
3.4 Multi-Angle Absorption Photometer	57
3.5 High-Volume samplers and chemical analysis	60
4 Characterization of aerosol sources in Granada.....	63

Contents

4.1	Methodology: Positive Matrix Factorization technique	65
4.2	PM concentration: major and trace elements.....	71
4.3	Apportionment and seasonality of the sources identified by PMF technique	76
4.4	Working versus non-working days variability.....	83
4.5	Daily exceedances: natural or anthropogenic?	85
4.6	Conclusions.....	86
5	Relationship between aerosol optical properties and chemical composition.....	89
5.1	Methodology: aerosol mass efficiencies.....	91
5.2	Overview: Chemical composition and aerosol optical properties	93
5.3	Mass scattering and absorption efficiencies	99
5.3.1	Measurement Method	99
5.3.2	Scattering and absorption efficiencies for coarse and fine particles applying MLR method.....	101
5.3.3	Scattering and absorption efficiencies for chemical species applying MLR Method	103
5.4	Conclusions.....	106
6	Aerosol Hygroscopicity.....	109
6.1	Study of the relative humidity dependence of aerosol light-scattering at Granada	111
6.1.1	Overview: Winter and spring campaigns.....	111
6.1.2	Diurnal cycles	119
6.1.3	Humidograms.....	121
6.1.4	Relationship between $f(RH)$ and other measured variables	125
6.1.5	Implication for climatic relevant variables	129
6.1.6	Conclusions.....	132
6.2	Aerosol light-scattering enhancement due to water uptake during the TCAP campaign.....	135
6.2.1	Site description	135
6.2.2	Instrumentation	136
6.2.3	Methodology	139
6.2.4	Overview of the campaign.....	140

6.2.5	Influence of wind speed and direction on the aerosol hygroscopicity	146
6.2.6	Air-mass trajectories classification	150
6.2.7	Relationship between γ and ω_0 and SAE	152
6.2.8	Conclusions	155
7	General conclusions and perspectives	157
	Conclusiones generales y perspectivas	163
	Quick finder	171
	References	181
	List of scientific contributions.....	199

Abstract

This PhD dissertation focuses on the characterization of atmospheric aerosol particles by means of ground-based in-situ techniques. To this end, a complete analysis of aerosol chemical and optical properties, including aerosol hygroscopicity, has been done.

A complete chemical analysis has been performed for the period 2006-2010 with special focus on the seasonality of fine and coarse fractions. A significant decreasing trend in PM₁₀ levels has been observed related with a decrease in most of its constituents, specially marked in mineral matter levels and non-mineral carbon. In addition, the main aerosol sources contributing to the fine and coarse aerosol mass concentration were identified and apportioned by means of the Positive Matrix Factorization technique. This analysis resulted in the identification of five sources in the coarse fraction and four in the fine fraction. In spite of being relatively uncommon, the use of fine and coarse PM in the PMF analysis separately was found to be very useful to discriminate additional sources.

Chemical composition of aerosol particles contributes, among other factors, to the aerosol optical properties observed. In order to find the relationship between aerosol optical properties and the chemical composition, the total scattering and absorption coefficients and speciated PM₁₀ and PM₁ data were combined for a period of one year to calculate the mass scattering and absorption efficiencies. Different existing methodologies (measurement method and Multiple Linear Regression method) were applied to determine the mass efficiencies of fine and coarse aerosol particles and of the different chemical constituents. This contributes to a better knowledge of the scattering properties

Abstract

of the different species since many previous works used only sulphate or bulk PM to account for the total scattering coefficient. Fine particles were found to extinct light more efficiently than coarse particles. Among the different aerosol constituents, $\text{SO}_4^{2-}\text{nm}$ exhibited the largest mass scattering efficiency and dust aerosols presented the lowest mass scattering efficiency. On the other hand, the absorption process was found to be mainly dominated by carbonaceous particles.

The ability of aerosol particles to take up water also affects the aerosol optical properties observed. Aerosol particles can take up water depending on their size, chemical composition and ambient relative humidity, RH. They become larger in size than their dry counterparts, and hence, scatter more light. This change in the scattering coefficient results also in changes in the radiative forcing estimations. Since the aerosol scattering coefficient is typically measured at dry conditions, knowledge of the scattering enhancement due to water uptake is of great importance in order to convert dry measurements into more relevant ambient data. For measuring the scattering enhancement due to water uptake, a humidification system was developed and built in the frame of this thesis for an integrating nephelometer. After successfully testing the humidifier in the laboratory, two measurement campaigns were conducted in Granada during winter and spring seasons. The results obtained during these measurement campaigns are presented in this thesis. The scattering enhancement factor, $f(\text{RH}=85\%)$, was found to undergo a clear diurnal pattern. The two $f(\text{RH}=85\%)$ minima were connected to the relative increase of the non-hygroscopic fraction (such as black carbon and road dust) due to traffic emissions during the traffic rush hours. The chemical composition was found to be very important in determining the aerosol hygroscopic properties. The $f(\text{RH}=85\%)$ decreased for increasing mass fraction of particulate organic

matter. Finally, the effect of RH on the radiative forcing estimations was accounted for.

The RH dependency of the scattering coefficient was also investigated at a different location, Cape Cod (Massachusetts, USA). The $f(\text{RH}=85\%)$ was found to be higher than in Granada mainly because of the influence of marine aerosols. The aerosol deliquescence was studied by investigating the differences in the $f(\text{RH})$ versus RH curve for RH above and below 65%. A clear relationship between the single scattering albedo, ω_0 , and the scattering Ångström exponent, SAE , with aerosol hygroscopicity was observed. In this sense, we propose an exponential equation that successfully estimates aerosol hygroscopicity as a function of ω_0 at Cape Cod.

Resumen

Esta tesis doctoral se centra en la caracterización de las partículas del aerosol atmosférico utilizando técnicas de medida in-situ desde superficie. Para ello se ha realizado un análisis completo de las propiedades químicas y ópticas de las partículas del aerosol atmosférico, incluyendo los efectos de higroscopidad.

Se ha realizado un análisis químico completo para el periodo 2006-2010 con especial énfasis en la estacionalidad de las fracciones fina y gruesa del aerosol atmosférico. Durante el periodo de estudio, se ha observado un descenso significativo en los valores de PM₁₀ y de la mayoría de sus constituyentes, estando este descenso especialmente marcado en los niveles de materia mineral y de carbón de origen no mineral. Además, las principales fuentes emisoras que contribuyen a las fracciones fina y gruesa del aerosol atmosférico se han identificado y cuantificado por medio de la técnica *Positive Matrix Factorization* (PMF) o factorización matricial positiva. Con este análisis se identificaron cinco fuentes en el modo grueso y cuatro en el fino. A pesar de no ser muy común, el uso de la fracción fina y gruesa de forma independiente en el análisis de PMF resultó ser de gran utilidad para discriminar fuentes adicionales de aerosol.

La composición química de las partículas del aerosol atmosférico contribuye, entre otros factores, a sus propiedades ópticas. Con el objetivo de estudiar la relación existente entre las propiedades ópticas del aerosol y su composición química, se han combinado los coeficientes de dispersión y absorción de aerosoles con la composición química de las fracciones PM₁₀ y PM₁ para calcular las eficiencias másicas de dispersión y absorción durante un periodo de un año. Se han aplicado diferentes metodologías existentes para determinar las eficiencias másicas de las fracciones fina y gruesa así como de

los principales componentes químicos del aerosol. Este estudio contribuye a un mejor conocimiento de las propiedades dispersantes de los diferentes compuestos atmosféricos ya que muchos trabajos previos han considerado sólo el sulfato o el PM total para dar cuenta del coeficiente de dispersión de aerosoles. Se ha encontrado que las partículas finas extinguen la radiación de forma más eficiente que las partículas gruesas, y entre los constituyentes del aerosol atmosférico estudiados, el sulfato de origen no marino es el que tiene una mayor eficiencia mísica de dispersión mientras que el polvo mineral es el que presenta la menor eficiencia mísica de dispersión. Por otro lado, el proceso de absorción se encuentra dominado por las partículas carbonosas.

La habilidad de las partículas del aerosol atmosférico para captar agua también afecta las propiedades ópticas del mismo. Las partículas de aerosol pueden captar agua dependiendo de su tamaño, composición química y de la humedad relativa ambiente. Al hacerlo, crecen en tamaño y dispersan más radiación. Este cambio en el coeficiente de dispersión implica cambios en las estimaciones de forzamiento radiativo. Puesto que el coeficiente de dispersión se mide normalmente en condiciones secas (humedad relativa inferior al 40%), conocer el realce en el coeficiente de dispersión debido al crecimiento higroscópico es de gran importancia para poder convertir las medidas realizadas en condiciones secas en datos a humedad relativa ambiente, de mayor importancia climática. Para medir el factor de realce en el coeficiente de dispersión, $f(RH=85\%)$, se ha desarrollado y construido en el marco de esta tesis doctoral un sistema de humidificación para el nefelómetro integrante. Una vez verificado el correcto funcionamiento del humidificador en el laboratorio, se han llevado a cabo dos campañas de medida en Granada durante el invierno y la primavera. Los resultados obtenidos durante las campañas de medida se presentan en esta tesis. Se ha encontrado que el factor $f(RH=85\%)$ posee un

marcado patrón diurno caracterizado por dos mínimos durante las horas de tráfico intenso, asociado con el aumento de la fracción no higroscópica (carbono negro y polvo) debido al tráfico rodado. La composición química es un factor determinante en las propiedades higroscópicas del aerosol. En este sentido, se ha encontrado que el factor $f(RH=85\%)$ decrece conforme aumenta la fracción de materia orgánica. Finalmente, el efecto de la humedad relativa en las estimaciones de forzamiento radiativo ha sido evaluado.

La dependencia del coeficiente de dispersión con la humedad relativa se ha investigado también en un lugar de estudio de características muy diferentes a las encontradas en Granada (Cape Cod, Massachusetts). El factor $f(RH=85\%)$ en Cape Cod es considerablemente más alto que en Granada, debido fundamentalmente a la influencia del aerosol marino. El fenómeno de delicuescencia se ha estudiado a través de las diferencias en la curva $f(RH)$ -RH para humedades relativas por encima y por debajo de 65%. Finalmente, se ha encontrado una relación entre el albedo de dispersión simple y el exponente de Ångström de dispersión con la higroscopicidad del aerosol. En este sentido, se propone una ecuación exponencial capaz de estimar de forma satisfactoria la higroscopicidad del aerosol atmosférico como función del albedo de dispersión simple en Cape Cod.

1 Introduction

In recent years, interest in better understanding the factors affecting the Earth's radiation budget, and hence the global climate has increased considerably. Aerosol particles, both natural and anthropogenic, are radiatively active components of the Earth's atmosphere. They play relevant roles in scattering and absorbing solar and infrared radiation and being at the same time able to act as cloud condensation and/or ice nuclei. During past years, a huge effort has been done in order to characterize the effects of atmospheric aerosols on climate. These effects are usually characterized by their influence on the radiative forcing (RF), considered as a measure of the influence a given factor has in altering the balance of incoming and outgoing energy in the Earth-atmosphere system [IPCC, 2007]. Thanks to this effort the uncertainties in the aerosol radiative forcing have been reduced with respect to the Fourth Assessment Report of the IPCC 2007 (Intergovernmental Panel for Climate Change) [IPCC, 2013]. However, atmospheric aerosol still contributing with the largest uncertainty to the total radiative forcing estimate, even though the level of confidence on the effects of the atmospheric aerosol has increased from low to medium for the indirect effect and from medium to high for the direct effect [IPCC, 2013]. Scattering aerosols with negative RF (e.g., sulphate, nitrate, and organic carbon) and absorbing aerosols with positive RF (e.g., black carbon) affect the radiation budget in the opposite way [Kopp and Mauzerall, 2010]. Assessing the role of aerosols in radiative forcing and visibility degradation often requires reducing their physicochemical properties to a set of variables that describe their optical properties as a function of the wavelength, λ . Among these variables, we would like to highlight the importance of the mass extinction efficiency (α_{ext}) of the different aerosol chemical species, which is the ratio of the aerosol extinction coefficient and particle mass. Estimates of the mass scattering and absorption efficiencies (α_{sp} and α_{ap}) are important in

aerosol modules of global circulation and chemical transport models that compute the radiative forcing effects of aerosols [Seinfeld and Pandis, 1998]. Typically, aerosol radiative properties are computed by converting an aerosol mass to aerosol optical depth using the mass extinction efficiency as a function of aerosol species and relative humidity [Hand and Malm, 2007]. The agreement of optical depths derived using different models and observational data (i.e., remote sensing) is dependent (among many factors) on the values of α_{sp} and α_{ap} applied in the models.

As we mentioned previously, mass extinction efficiencies are not measured directly; they are derived from measurements of aerosol optical and physicochemical properties. In this sense, there are several approaches used to derive them, depending on the data available. Estimates of α_{sp} and α_{ap} can be computed by applying Mie theory to aerosol size distributions with assumptions of optical and chemical properties, or from bulk mass measurements and measured light scattering or extinction coefficients from nephelometry or transmissometry, or using multilinear regression techniques and speciated or size segregated mass data. Different methodologies, among other factors, contribute to large uncertainties in the determination of the mass extinction efficiency [Hand and Malm, 2007].

Many previous estimations of α_{sp} have been made using only sulphate to represent particle mass [Vrekoussis *et al.*, 2005; Bryant *et al.*, 2006], while other components, such as mineral matter, nitrate or organic aerosols, were not considered. This assumption is not valid and it is clear that other aerosols species play an important role in the scattering process [Andreae *et al.*, 2002; Hand and Malm, 2007; Cheng *et al.*, 2008] that need to be quantified. In particular, Hand and Malm [2007] reported larger mass scattering efficiencies for fine nitrate and fine particulate organic matter than for fine sulphate

particles (average over a survey of approximately 60 studies) and the largest mass scattering efficiency was found for fine sea salt particles although large differences exist among studies. In general, fine particles were found to extinct light more efficiently than coarse particles [*Hand and Malm*, 2007]. Due to their importance in climate models, *Hand and Malm* [2007] emphasized the need of performing measurements over extended periods of time to obtain representative estimations of mass extinction (scattering and absorption) efficiencies.

Depending on the ambient relative humidity and the aerosol chemical composition and size, aerosol particles can take up water become larger in size than their dry counterparts, and scatter more light. Wet particles may also have different angular scattering properties and refractive indices than their dry equivalents. Deliquescent aerosol particles can exist in two phases at the same relative humidity (RH), known as hysteresis [*Orr Jr. et al.*, 1958]. For increasing RH, pure deliquescent aerosol particles experience a sudden phase transition from solid to liquid at a defined RH that is called deliquescence relative humidity (DRH). Once the RH is above the DRH and the particle is liquid, a decrease in RH does not make the particle to recrystallize at the DRH. The recrystallization RH is known as efflorescence relative humidity. As shown by *Tang and Munkelwitz* [1993] mixed deliquescent aerosol particles can exhibit one or more phase changes. If the particles are not deliquescent but hygroscopic, they grow or shrink monotonically with increasing or decreasing RH. All these effects present a direct influence in the radiative forcing of aerosol particles being of great scientific importance its quantitative determination.

Numerous works have investigated the change in size of aerosol particles due to water uptake by means of Humidified Tandem Differential

Mobility Analyzers (HTDMAs) [Massling *et al.*, 2007; Meier *et al.*, 2009; Wu *et al.*, 2013, and references therein]. Some of these works include theoretical calculations using Mie theory to quantify the effect that this growth in size may have in the scattering coefficient, which is of more climatic relevance. However, it is possible to measure directly the enhancement in the scattering coefficient due to water uptake by means of a tandem of nephelometer set-up [e.g., Covert *et al.*, 1972; Fierz-Schmidhauser *et al.*, 2010a]. Typically, one of the nephelometers measures the particle light scattering coefficient at a reference RH (usually between 20-40%) while the second nephelometer measures the particle light scattering coefficient at a high RH (up to 90%). The combination of both measurements allows the determination of the scattering enhancement factor, $f(\text{RH})$, defined as the aerosol particle scattering coefficient at a certain RH divided by its dry value. This factor quantifies the amount of change in the particle light scattering coefficient due to water uptake. Quantitative knowledge of the scattering enhancement is very important when comparing remote sensing measurements such as lidar or sun photometers with in-situ measurements [e.g. Estéve *et al.*, 2012; Zieger *et al.*, 2011; 2012], as well as for climate models. Most measurement stations, like those involved in the ACTRIS (Aerosols, Clouds, and Trace gases Research InfraStructure Network, <http://www.actris.net/>) or GAW (Global Atmospheric Watch, <http://www.wmo.int>; WMO/GAW, 2003) networks, perform routine measurements of the aerosol optical and physical properties at dry conditions ($\text{RH} < 40\%$). In order to use these measurements at low RH in climate studies, the influence of ambient RH must be taken into account. Typical measured ambient values of $f(\text{RH})$ for different aerosol types are: $f(\text{RH}=85\%) = 2.2$ [Fierz-Schmidhauser *et al.*, 2010c] and $f(\text{RH}=85\%) = 3.5$ [Zieger *et al.*, 2010] for marine aerosols in Ireland and the Arctic, respectively, $f(\text{RH}=85\%) = 1.83$

for continental aerosols [Sheridan *et al.*, 2001], $f(\text{RH}=80\%) = 1.2$ [Pan *et al.*, 2009], $f(\text{RH}=85\%) = 1.72$ [Fierz-Schmidhauser *et al.*, 2010b] and $f(\text{RH}=85\%) = 1.59$ [Sheridan *et al.*, 2001] for dust dominated aerosols and $f(\text{RH}=80\%) = 1.26$ [Yan *et al.*, 2009] for urban aerosols. Hygroscopic properties of laboratory generated aerosols have been also reported in the literature [e.g. Kus *et al.*, 2004; Garland *et al.*, 2007; Fierz-Schmidhauser *et al.*, 2010a]. Large scattering enhancement factors were observed for inorganic salts such as sodium chloride with $f(\text{RH}=80\%)$ around 8 or ammonium sulphate with $f(\text{RH}=80\%)$ around 3-4 [Kus *et al.*, 2004]. The scattering enhancement due to water uptake was found to decrease with increasing organic content in inorganic-organic mixtures [Garland *et al.*, 2007]. This fact was also evidenced by Quinn *et al.* [2005] for ambient aerosols. These authors observed a decrease in the scattering enhancement for increasing the fraction of organic matter (OM) in sulphate-OM mixtures.

Apart of the effects of aerosol particles on the Earth's radiative balance and visibility, they also have harmful effects on human health. For these reasons, European directive 2008/50/EC regulates the levels of PM₁₀ (particles with an aerodynamic diameter <10 µm) setting the daily limit in 50 µg/m³ that cannot be exceed more than 35 times per year and the annual limit in 40 µg/m³. In addition to PM₁₀, PM_{2.5} (particles with an aerodynamic diameter <2.5 µm) is also regulated in the European directives (annual limit value of 25 µg/m³ mandatory for 2015), however, there is no regulation concerning PM₁ (particles with an aerodynamic diameter <1 µm). This fact evidences a gap in the European legislation because it is well known that most anthropogenic pollutants tend to accumulate in the finer fractions and that fine particles present harmful effects on human health [Pope and Dockery, 2006]. The concentration of PM at a specific location depends on a large number of factors,

such as local and regional PM sources as well as the meteorological conditions and geographical situation. Thus, the design of strategies to reduce the concentrations of PM and meet the European targets is a very difficult task. Several studies were conducted during the past years in order to assess the main sources affecting PM concentration at different environments by applying different methodologies. Receptor models, like Positive Matrix Factorization (PMF, *Paatero and Tapper*, 1994], Principal Component Analysis (PCA, *Thurston and Spengler*, 1985], Chemical Mass Balance (CMB; US-EPA, 1987] or COnstrain Physical REceptor Model (COPREM, *Wahlin et al.*, 2003] are widely used to identify the main sources affecting PM from its chemical composition [e.g. *Tauler et al.*, 2009; *Viana et al.*, 2008a]. In this sense, sensitivity studies have been conducted in last years to evaluate the comparability between different receptor models [e.g. *Pandolfi et al.*, 2008; *Viana et al.*, 2008a; *Viana et al.*, 2008b; *Calvo et al.*, 2013]. These authors concluded that the models agreed well in most cases both in the identification and in the interpretation of sources, although differences were also observed among models. Furthermore, the computation requirements also differ among models. *Viana et al.* [2008b] pointed out that more investigation should be done in this field to ensure that the different methodologies for source apportionment studies are robust enough to assess PM health effects. Furthermore, a better characterization of aerosols sources can be achieved by applying receptor models in size fractionated particulate matter as suggested by *Pant et al.*, [2012].

1.1 Objectives and outline

The main objective of this thesis is to improve the knowledge on atmospheric aerosol research, with special focus on the issues that are still quite open and are

a source of uncertainty in the atmospheric and climate studies. For this purpose, the study was approached from different points of view. The first one is the characterization of the aerosol chemical composition and the identification of the main aerosol sources affecting the study area by means of receptor models applied to chemical composition data. The second one considers the analysis of the aerosol optical properties, the link between aerosol chemical composition and their optical properties and the effects of aerosol hygroscopic growth on the aerosol optical properties obtained by means of ground-based in-situ techniques.

The thesis dissertation is organized in several chapters, as indicated in the following outline:

Chapter 2 is devoted to the basic concepts behind the aerosol science with special emphasis on the hygroscopic growth effects.

Chapter 3 is a brief overview of the experimental station where the majority of the measurements used in this thesis were performed, together with a short description of the main instrumentation employed, namely the integrating nephelometer (reference and humidified), the multi-angle absorption photometer and the high-volume samplers and consequent chemical analyses procedure.

Chapter 4 presents the main results concerning the characterization of the aerosol chemical composition over the period 2006-2010 in Granada. Positive Matrix Factorization technique was applied in order to identify and apportion the main sources contributing to the aerosol mass concentration observed.

Chapter 5 deals with the relationship between aerosol chemical composition and their optical properties. For this purpose, the mass scattering

and absorption efficiencies were calculated for a period of one year applying different existing methodologies, using measurements gathered in Granada.

Chapter 6 analyses the effects of the aerosol hygroscopic growth on the aerosol scattering coefficient by means of nephelometers tandem. The first part of this chapter is focused on the study of the aerosol light scattering enhancement factor in Granada. For this study, a custom built humidification system was specifically developed in the frame of this thesis (technical aspects of the experimental set-up are presented in Chapter 3) and the main results are presented here. The second part of this chapter continues with the study of the effects of hygroscopic growth in the scattering coefficient but at a different location (Cape Cod, Massachusetts, USA) influenced by very distinct aerosol conditions compared to Granada.

Finally, Chapter 7 presents a summary of the main conclusions of this thesis together with an outline of future research activities.

2 Fundamentals

2.1 Atmospheric aerosols: Types, sources and processes affecting aerosol particles.

The Earth's atmosphere is defined as the layer of gases surrounding the planet that is retained by Earth's gravity. The Earth's atmosphere is mainly composed of two groups of gases. The first group consists of those gases with nearly steady concentrations, whereas the second one consists of gases with variable concentrations. Among other atmospheric components clouds and atmospheric aerosol particles, which are highly variable in space and time, are included. An aerosol is technically defined as a suspension of liquid or solid particles in a gas [*Seinfeld and Pandis, 1998*]. Aerosol particles originate from different sources, are exposed to different kinds of processes in the atmosphere, and are removed from it by a variety of sinks. Their lifetime can span from a few days to a few weeks, which contrasts with the lifetime of greenhouse gases that can range up to years. The combination of specific sources and short lifetimes of aerosol particles explains their highly non-uniform distribution around the globe. The size of aerosol particles is also highly variable, ranging from a few nanometers to several hundreds of micrometers. In general, the aerosol size distribution is characterized by different size modes, which are specific concerning their sources, their different transformation and the removal processes. Figure 2-1 shows a schematic three modal surface size distribution with an overview on the relevant processes and example images of typical aerosol particles found in these modes.

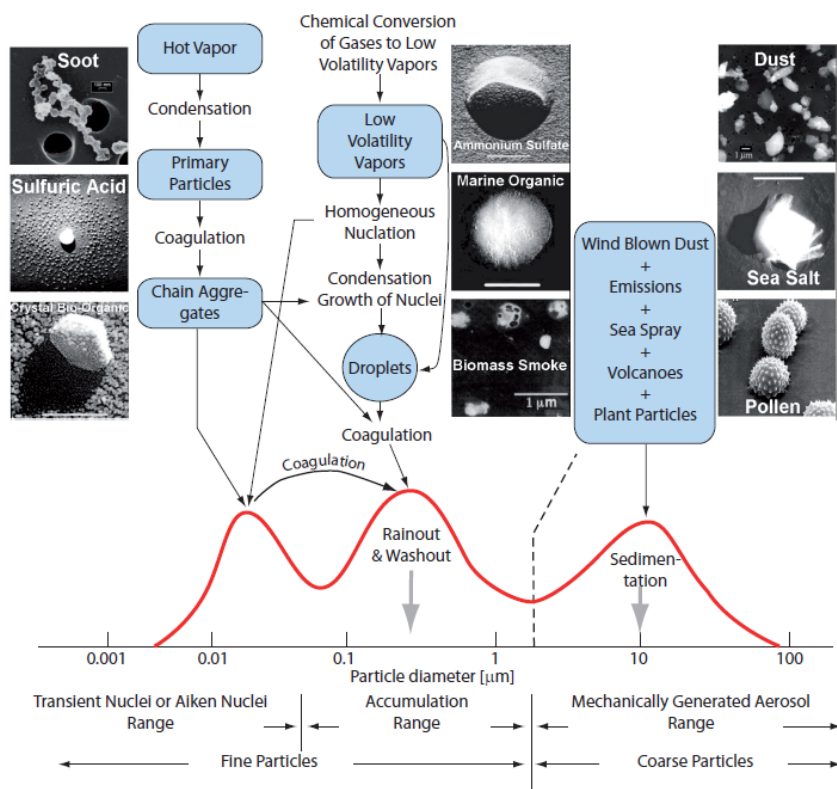


Figure 2-1: Idealized scheme of the distribution of particle surface area of an atmospheric aerosol. Principal modes, sources and particle formation and removal mechanisms are also indicated (Figure taken from Zieger [2011], originally adapted from Whitby and Cantrell, 1976; Seinfeld and Pandis, 1998; Heintzenberg et al., 2003].

The main separation is made between the fine mode (particle diameter $D_p < 2.5 \mu\text{m}$) and the coarse mode ($D_p > 2.5 \mu\text{m}$). The more important removal process of the coarse mode is gravitational settling due to their larger size and mass. Therefore, this mode is usually characterized by short residence times in the atmosphere. A further division of the fine mode involves the separation between the nucleation, Aitken and accumulation modes. The nucleation mode refers to very small particles ($D_p < 10 \text{ nm}$) that are freshly nucleated particles. The Aitken mode, which comprises particles with diameter between 10 nm and 0.1 μm , is characterized by a high number concentration of particles that mainly

originate from gas-to-particle conversion of hot vapors (e.g. from combustion processes) and are transformed through coagulation into particles of the accumulation mode. The accumulation mode ($0.1 < D_p < 2.5 \mu\text{m}$) comprises particles characterized by low removal efficiency and contains particles either from coagulated particles from the nucleation mode or through growth by condensation of vapors on existing particles. In this mode, the main removal mechanism is rain-out (in-cloud scavenging, e.g. by forming cloud droplets) or washout (collision with rain droplets or snowflakes).

Sources of atmospheric aerosol particles can be split into natural and anthropogenic. According to their origin, it is possible to differentiate between primary (emitted directly into the atmosphere) and secondary aerosol particles (formed in the atmosphere through gas-to-particle conversion). The main natural primary particle is sea salt, which is emitted from the oceans by evaporated sea spray. Mineral dust, originating from arid and semi-arid regions of the world, is the second important contributor of natural primary particles. Because mineral desert dust can be transported over thousands of kilometers, it is not only a regional phenomenon, but has a global climate effect. The chemical composition of mineral particles is highly variable and depends on the source region and transport pathways. The main constituents are silicon oxides (SiO_2), carbonates like calcite (CaCO_3) and dolomite ($\text{CaMg}(\text{CO}_3)_2$), sulphates, phosphates and iron oxides (e.g. hematite) [Castillo, 2006]. Volcanic dust and biogenic particles (e.g. pollen or other plant material) are other natural primary particles. All these natural primary particles are mainly found in the coarse mode of the aerosol size distribution (see Figure 2-1). Typical natural sources of secondary aerosols are the biosphere and volcanoes that emit sulfur (e.g. in form of dimethyl sulfide, DMS, and sulfur dioxide into the atmosphere) which can be oxidized to sulphate and form new particles. The biosphere can also emit

volatile organic compounds (VOCs) that can be oxidized and are able to form new particles. Anthropogenic emissions of primary particles include black carbon from incomplete combustion and organic material. Dust emissions also have a significant anthropogenic component mainly originating from agricultural, industrial practices and road traffic. Secondary aerosol sources of anthropogenic origin include sulphates from SO₂ emissions, biomass burning, organics from anthropogenic VOCs, ammonia emissions, and nitrates from nitrogen oxides. These gases can be emitted, for example, through domestic heating systems based on coal or wood combustion, industrial plants, vehicle emissions and agricultural activities. Although the global emissions are dominated by the natural sources (*Seinfeld and Pandis* [1998] give an estimate of 3100 Tg/year), they are mainly related to contributions from the coarse mode, while the emissions from anthropogenic sources (*Seinfeld and Pandis* [1998] estimate 450 Tg/year) are mainly contributions from the fine mode (with correspondingly higher number concentrations).

2.2 How anthropogenic aerosols affect visibility, human health and climate?

Anthropogenic emissions of aerosol particles have many effects on the environment. These are for example linked with visibility degradation [e.g., *Malm et al.*, 1994], which can be downgraded under the presence of aerosols (which causes additional scattering and absorption of light) to a few kilometers or even to a few hundreds of meters in very polluted areas. Also the water uptake ability of the aerosol has a major influence on the visibility.

Another effect of aerosol particles is related to their adverse health effects on humans, since particles can enter the human respiratory and cardiovascular system, where they may cause damage on cells and organs.

Several studies [e.g., *Pope and Dockery*, 2006] have shown the relationship between air pollution and an increased rate of mortality.

Aerosol particles also produce perturbations in the Earth's energy balance. The radiative forcing is defined as a measure of the influence that a factor has in altering the balance of incoming and outgoing energy in the Earth-atmosphere system [IPCC, 2007]. The radiative effects of atmospheric aerosol particles are highly important for the Earth's climate, as indicated by the Fifth Assessment Report (AR5) of the IPCC [2013]. Only the atmospheric aerosol from anthropogenic origin is considered as an external cause of climate change [Charlson *et al.*, 1992; IPCC, 2007]. According to the AR5, the total anthropogenic radiative forcing for 2011 relative to 1750 is 2.29 [1.13 to 3.33] $\text{W}\cdot\text{m}^{-2}$ (Figure 2-2), and it has increased more rapidly since 1970. The total anthropogenic radiative forcing best estimate for 2011 is 43% higher than that reported in IPCC 2007 AR4 (Fourth Assessment Report) for the year 2005. This is caused by a combination of continued growth in most greenhouse gas concentrations and improved estimates of radiative forcing by aerosols indicating a weaker net cooling effect (negative radiative forcing).

The radiative forcing of the total aerosol effect in the atmosphere, which includes cloud adjustments due to aerosols (the so-called indirect effect in the AR4), is -0.9 [-1.9 to -0.1] $\text{W}\cdot\text{m}^{-2}$ (medium confidence), and results from a negative forcing from most aerosols and a positive contribution from solar radiation absorption by black carbon. Aerosols still contribute to the largest uncertainty to the total radiative forcing estimate, even though this is considerably reduced due to the increase in the knowledge of the aerosol properties in the last years.

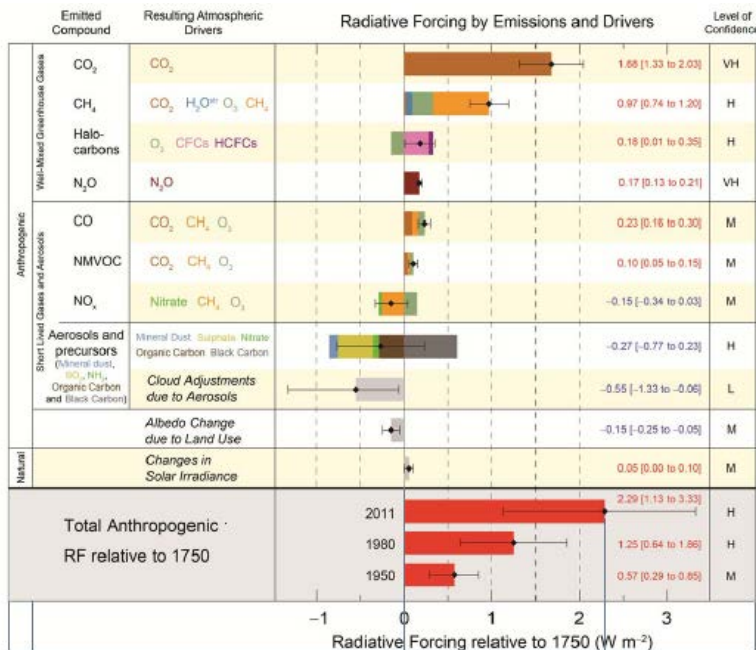


Figure 2-2: Radiative forcing estimates in 2011 relative to 1750 and aggregated uncertainties for the main drivers of climate change taken from IPCC [2013]. Values are global average radiative forcing. The best estimates of the net radiative forcing are shown as black diamonds with corresponding uncertainty intervals; the numerical values are provided on the right of the figure, together with the confidence level in the net forcing (VH – very high, H – high, M – medium, L – low, VL – very low). Total anthropogenic radiative forcing is provided for three different years relative to 1750.

The above mentioned influence of the atmospheric aerosol on the Earth's energy budget may be caused in two different ways: direct and indirect. The so-called direct effect is the mechanism by which aerosol particles scatter and absorb shortwave and longwave radiation altering the radiative balance of the Earth-atmosphere system [IPCC, 2007]. The indirect effect is the mechanism by which aerosol particles influence cloud properties through their role as cloud condensation nuclei (CCN) and/or ice forming nuclei. The increase in aerosol particle concentrations may increase the ambient concentration of CCN and/or ice forming nuclei, therefore affecting cloud properties. A CCN increase can lead to more cloud droplets so that, for fixed

cloud liquid water content, the cloud droplet size will decrease. This effect leads to brighter clouds (the so-called “cloud albedo effect”, “Twomey effect” or “first indirect effect”). The term “second indirect effect” is applied to the microphysically induced effect on the liquid water content, cloud height, and lifetime of clouds [Ramaswamy *et al.*, 2001]. It is also called the “cloud lifetime effect” [Lohmann and Feichter, 2005] or the “Albrecht effect” [Albrecht, 1989]. Because of this effect, aerosol particles can also affect clouds by suppressing drizzle, increasing cloud lifetime and height and hence increasing the amount of solar radiation reflected from clouds. Such effect can change precipitation patterns as well as cloud extent and optical properties. The semi-direct effect [Menon *et al.*, 2002; Cook and Highwood, 2004; Johnson *et al.*, 2004] is defined as the mechanism by which absorption of shortwave radiation by tropospheric aerosols leads to heating of the troposphere that in turn changes the relative humidity and the stability of the troposphere and thereby influences cloud formation and lifetime.

2.3 Interactions of light with particles

In the atmosphere, a parallel beam of light passing a distance dx through a layer of aerosol is attenuated due to scattering and absorption of radiation by particles and gas molecules. The possible interactions of light with particles are defined as follows:

- Absorption is a process where the incident energy becomes part of the internal energy of the particles with which they interact.
- Scattering is a process where the incident energy transported by an electromagnetic wave is dispersed in all directions at the same wavelength as a result of the interaction of the particles with this electromagnetic wave. Thus, in this process, the incident energy never became part of the internal energy of

particles.

- Extinction is used to describe the attenuation of light by particles due to a combination of scattering and absorption processes.

For the general treatment of the extinction let us consider a well collimated beam of monochromatic light $L_{0\lambda}$ entering a homogeneous medium, as in Figure 2-3. L_λ is the radiance after traversing a distance x in the direction of its propagation.

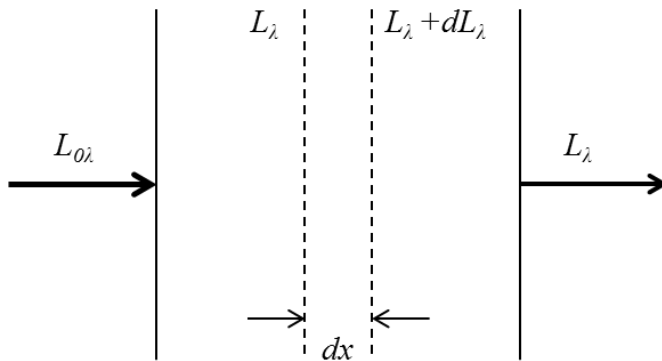


Figure 2-3: Attenuation of radiation

The amount attenuated in passing through the medium can be evaluated by Beer-Bouguer-Lambert law as shown in Eq. 2.1:

$$L_\lambda = L_{0\lambda} e^{-\sigma_{ext}(\lambda)x} \quad \text{Eq. 2.1}$$

where $\sigma_{ext}(\lambda)$ is the extinction coefficient (Eq. 2.2) for radiation of wavelength λ , which is the sum of the scattering coefficient $\sigma_{sca}(\lambda)$ and the absorption coefficient $\sigma_{abs}(\lambda)$.

$$\sigma_{ext}(\lambda) = \sigma_{sca}(\lambda) + \sigma_{abs}(\lambda) \quad \text{Eq. 2.2}$$

Since the exponent of an exponential function must be dimensionless, the extinction, scattering and absorption coefficients must have the unit of an inverse length (typically, Mm^{-1}). In the case of atmospheric air the light

extinction is caused by light absorption and light scattering caused by air molecules and by the particles within the air. The total scattering and absorption coefficients are the sum of these properties as can be seen in the following expressions:

$$\sigma_{sca} = \sigma_{rg} + \sigma_{sp} \quad \text{Eq. 2.3}$$

$$\sigma_{abs} = \sigma_{ag} + \sigma_{ap} \quad \text{Eq. 2.4}$$

where σ_{rg} , σ_{sp} , σ_{ag} and σ_{ap} refer to the scattering by gases or Rayleigh scattering, scattering by particles, absorption by gases and absorption by particles, respectively.

The scattering process is highly dependent on the size parameter, x , defined as the relation between the particle radius and the wavelength of the incident wave ($x=2\pi r/\lambda$) and also on the refractive index m , which depends on the particle chemical composition. If $x < 0.6/n$, with n the real part of the complex refractive index of the particles, the scattering process is described by Rayleigh theory. The Rayleigh's theory, which describes the scattering of solar radiation by air molecules, is based on the assumption that the scattering particles are spherical with radii less than 0.2 times the wavelength of the incident radiation. It only considers single-scattering processes. A key feature of this theory is that the monochromatic optical extinction varies approximately as λ^{-4} , what has been verified experimentally. If $0.6/n < x < 5$, the scattering is explained by Mie theory. It is applied when the size of the particles is comparable to the incident wavelength ($x \sim 1$). Figure 2-4 shows the differences between Rayleigh and Mie scattering. Rayleigh scattering is symmetric respect to the plane perpendicular to the propagation direction with minimum at the scattering angle $\theta = \pm 90^\circ$, being its maximums at $\theta = 0^\circ$ and $\theta = 180^\circ$. On the

other hand, Mie scattering presents an asymmetry pattern, with a strong forward scattering compared to Rayleigh pattern.

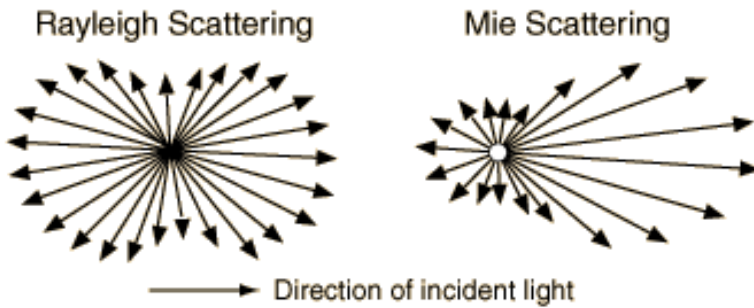


Figure 2-4: Rayleigh scattering and Mie scattering.

When the radiation interacts with particles, the processes of scattering and absorption occur simultaneously. The relative importance of the scattering and absorption processes is characterized by the single scattering albedo, defined as:

$$\omega_0(\lambda) = \frac{\sigma_{sp}(\lambda)}{\sigma_{sp}(\lambda) + \sigma_{ap}(\lambda)} = \frac{\sigma_{sp}(\lambda)}{\sigma_{ep}(\lambda)} \quad \text{Eq. 2.5}$$

It mainly depends on the relative source apportionment of the various aerosol substances and on aging during transport. Absorption of solar radiation by atmospheric aerosols mainly results from elemental carbon originated from biomass burning and fuel combustion, which absorbs light strongly in the visible spectrum, and from organic carbon and hematite (from mineral dust), that absorb light mostly in the ultraviolet range.

The wavelength dependence of σ_{sp} is characterized through the scattering Ångström exponent, SAE, according to the following formula for $\lambda_1 = 700$ nm and $\lambda_2 = 450$ nm.

$$SAE(\lambda_1 - \lambda_2) = -\frac{\log \sigma_{sp}(\lambda_1) - \log \sigma_{sp}(\lambda_2)}{\log \lambda_1 - \log \lambda_2} \quad \text{Eq. 2.6}$$

This variable increases with decreasing particle size and takes values around 2 when the scattering process is dominated by fine particles, while it is close to 0 when the scattering process is dominated by coarse particles [Seinfeld and Pandis, 1998; Delene and Ogren, 2002].

2.4 Water uptake by aerosol particles

An important factor that can modify the role of aerosols in the global energy budget is the relative humidity (RH). Aerosol particles can take up water, become larger in size than their dry equivalents, and hence, scatter more light because of the increase in the particle cross section. Wet particles may also have different refractive indices and angular scattering properties than their dry counterparts. To quantify the amount of change in the particle light scattering coefficient due to water uptake, the scattering enhancement factor, $f(RH)$, is introduced. This factor is calculated as the ratio between the scattering coefficient at a certain RH to the scattering coefficient at reference RH conditions (typically, RH<40%). This factor is dependent on the aerosol chemical composition and the size distribution. Particle composition is important because it determines the refractive index (particles with a higher refractive index scatter more light), and its hygroscopic properties.

Aerosol particles can be split into three categories according to their hygroscopic growth patterns. Some aerosol species like soot or mineral dust are insoluble and do not grow significantly in diameter with increasing RH [Weingartner *et al.*, 1997; Sjogren *et al.*, 2007]. On the contrary, some aerosol species like H₂SO₄ and some organics are soluble and they are able to take up water and grow or shrink smoothly as the RH increases or decreases (Figure

2-5). These aerosol species are hygroscopic but do not show hysteresis behavior (hysteresis refers to when an aerosol particle exists in two phases at the same RH, [Orr Jr. et al., 1958]). The third group of aerosol species is also hygroscopic but shows hysteresis behavior, they are named as deliquescent aerosols. NH_4HSO_4 , $(\text{NH}_4)_2\text{SO}_4$ and NaCl are examples of deliquescent substances (Figure 2-5).

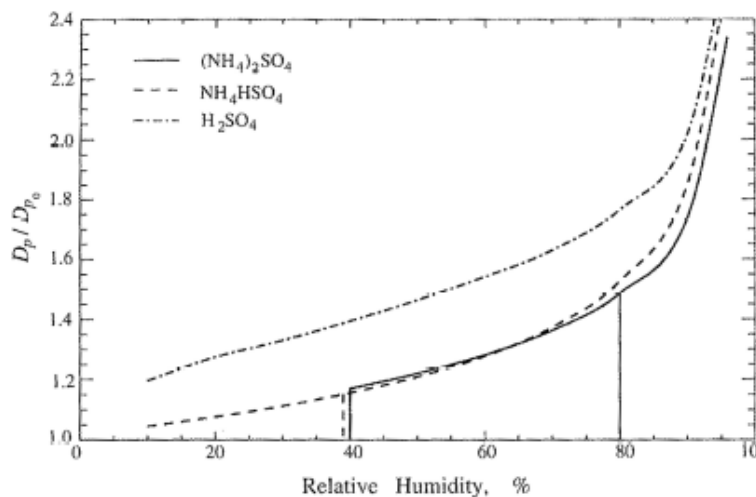


Figure 2-5: Diameter change of $(\text{NH}_4)_2\text{SO}_4$, NH_4HSO_4 , and H_2SO_4 particles as a function of relative humidity. D_{p0} is the diameter at 0% RH [from Seinfeld and Pandis, 1998].

For increasing RH, pure deliquescent aerosols experienced a sudden phase transition from solid to liquid at a defined RH named as deliquescence relative humidity (DRH) which is characteristic of the chemical compound. Once the RH is above the DRH and the particle is liquid, decreasing RH does not make the particle recrystallize at the DRH. The RH at which recrystallization occurs is called efflorescence relative humidity (ERH). As shown by Tang and Munkelwitz [1993] mixed deliquescent aerosols can exhibit one or more phase changes. The RH history of an air parcel and thus the knowledge of the DRH and ERH points are of great importance because they

define which fraction of the atmospheric aerosol is present purely as liquid droplets. This liquid fraction scatters much more light than the fraction that is solid [Toon *et al.*, 1976; Sloane, 1984].

Although most chemical transport and radiative transfer models have incorporated empirically derived $f(\text{RH})$ values [Massoli *et al.*, 2009], some difficulties still exist in modeling the changes of aerosol optical properties with water uptake for aerosol mixtures involving species such as dust and soot, and specially organic aerosols [Malm and Kreidenweis, 1997; Mircea *et al.*, 2005]. Knowledge of the scattering enhancement due to water uptake is of great importance in order to convert dry measurements into more relevant ambient measurements, especially when comparing in-situ with remote sensing measurements [e.g., Estéve *et al.*, 2012; Shinozuka *et al.*, 2013] or for satellite retrievals [e.g., Wang and Martin, 2007].

Aerosol scattering enhancement factors can be directly measured or they can be derived from measurements of aerosol physicochemical properties. There are several approaches to derive $f(\text{RH})$, depending on the data available. Estimates of $f(\text{RH})$ can be computed by applying Mie theory to aerosol size distributions with assumptions of optical and chemical properties [e.g. Zieger *et al.*, 2014], or from measurements of visibility at ambient RH and dry scattering measurements [e.g. Liu *et al.*, 2008], or from combined nephelometry measurements at different RH values [e.g. Covert *et al.*, 1972]. In this thesis, we will focus on measurements of ambient aerosol particles scattering coefficients at varying RH obtained with nephelometry techniques.

2.5 History and development of humidified nephelometers

Pilat and Charlson [1966] built the first humidified nephelometer. This device was used to measure the RH dependency of polydisperse NaCl in the

laboratory. The aerosol sample is humidified in a heated chamber and then the aerosol is mixed with a stream of moist air and a stream of dry air. By changing the flow rates of both streams the desired humidity is achieved.

Another humidification system for a nephelometer was developed by *Covert et al.* [1972]. As in the device of *Pilat and Charlson* [1966], the variation of the RH of the aerosol sample is achieved by addition of a controlled, warm and moist air stream. This air stream is then introduced in a mixing chamber under highly turbulent flow conditions in order to increase uniformly the RH. After the mixing chamber, the aerosol pass through a series of chambers of different volumes to allow aging of the humidified aerosol and the growth to equilibrium sizes at a given RH, before measuring the scattering coefficient with a nephelometer. The RH in the nephelometer is calculated from a temperature and dew point sensors located in the scattering chamber. The system of *Covert et al.* [1972] scans the relative humidity from 20 to 90% in 4 minutes. This short scan time is appropriate in order to sample homogeneous atmospheric aerosol, especially when using only one nephelometer. However, for such large changes in RH in such a small time the RH sensors need to have a very fast time response, which is difficult to achieve even using dew point sensors [*Fierz-Schmidhauser et al.*, 2010a].

Rood et al. [1985] used a humidified nephelometer to determine the atmospheric aerosol scattering enhancement combined with a thermidograph which estimates the aerosol chemical composition [*Larson et al.*, 1982]. *Rood et al.* [1985] found that the mixing of the dry and moist air streams leads to a brief exposure of the particles to a RH greater than the final RH value measured inside the nephelometer. This results in marginal resolution of the deliquescent step. Another inconvenient of dilution is that reduces the aerosol concentration which decreases the detection signal in case of low aerosol concentrations as it

might happen in remote or background environments. In order to avoid dilution of the aerosol sample with dry and moist air, in the humidifier of *Rood et al.* [1985], the sample air is passed through a hollow cylinder in which the inside wall is covered with nylon mesh and wetted with a H_2SO_4 solution. The wetted wall is gradually heated such that the amount of heat flux through the wall controls the increasing dew point temperature of the aerosol. The air stream exiting the humidifier is rapidly heated to a peak temperature of 60°C and then cooled to ambient temperature prior to entering the nephelometer. In the heating section, the RH decreases to <20% due to the increased temperature. Such a decrease in RH is sufficient to effloresce the previously deliquesced particles. Subsequent cooling increases the aerosol RH to its final value. Particles passing through the cooler experience a range of RH values depending on the cooler's temperature. Near the exit of the cooler chamber, the temperature of the aerosol sample returns to room temperature but does not drop below that temperature. Therefore nowhere in the cooler chamber have the particles been exposed to a RH greater than that within the nephelometer [*Rood et al.*, 1985]. This prevents that some particles deliquesce before reaching the nephelometer.

In order to examine the response of particles to decreasing RH, *Rood et al.* [1985] replaced this humidification system by a humidifier consisting of two concentric wetted walls. As the aerosol particles pass through this humidifier, they are exposed to a RH greater than 80% and also experience RHs below 80% downstream of the humidifier. Enhanced RH within this humidifier, compared to the nephelometer, results from a reduction in the temperature due to evaporative cooling. Therefore, this humidification system is able to expose deliquescent aerosol particles to a RH above their DRH and then expose them to a gradually decreasing RH, allowing the study of the hysteresis loop. *Rood et*

al. [1987] further improved their set-up by using three nephelometers, which allowed them to study ambient metastability of hygroscopic aerosol particles.

In the set-up of *Koloutsou-Vakakis* [1996] and *Koloutsou-Vakakis et al.* [2001] two nephelometers are run in parallel. One nephelometer measures the scattering coefficient of the ambient aerosol at RH<40% and the second nephelometer at scanning RH. The humidifier consists of a Teflon membrane that allows transport of water vapor to the aerosol, which is inside a stainless steel tube. The amount of water vapor that passes into the aerosol stream is determined by controlling the temperature of the water. This humidifier represents a great improvement with respect to previous designs since it eliminates direct contact of liquid water with the aerosol flow, avoids the need of dilution to control the RH of the aerosol particles, and thus prevents exposure of the aerosol particles to air that is not of the same composition as the ambient air. Currently, ESRL-NOAA (Earth System Research Laboratory, National Oceanic and Atmospheric Administration) runs a very similar humidified nephelometer at several baseline stations in the USA and at mobile or cooperative platforms all over the world. NOAA runs the nephelometers in series (separated by the humidifier system) instead of in parallel.

Carrico et al. [2000] further improved the humidification system developed by *Koloutsou-Vakakis* [1996] by using Peltier thermoelectric coolers. These coolers allow RH>80% to be achieved locally upstream of the RH-scanning nephelometer while performing decreasing RH scans within the nephelometer to investigate the decreasing RH branch of the hysteresis loop.

The system of *Day et al.* [2000], based on a different working principle, consists of a group of Perma Pure® drying tubes that is used to control the RH of the sample air. The aerosol sample enters an array of 23 Perma Pure® diffusion drying tubes, which are mounted in parallel. The sample's RH is

brought to the desired value, using the drying tubes. The Perma Pure® diffusion drying tubes, used to control sample RH, consist of an inner tube of Nafion through which the aerosol sample flows and an outer tube of stainless steel through which purge air flows. The RH of the aerosol sample can be increased or decreased depending on the RH of the purge air. Finally, the aerosol sample is drawn into a plenum where the RH and temperature of the aerosol sample are continuously monitored and then is passed to the nephelometer. This humidification system is able to achieve relative humidity values in the range 5-95%. In order to have accurate measurements of RH, *Day et al.* [2000] kept the temperature of the aerosol sample nearly constant. To this end, the array of dryers was housed in an insulated aluminum cylinder that was filled with water.

Recently, *Fierz-Schmidhauser et al.* [2010a] have built a humidification system that is able to measure aerosol metastability. In their system, the aerosol first enters a humidifier, which consists of a Gore-Tex® tube surrounded by a thin water layer in a heatable metal tube. Secondly, the aerosol enters a dryer that consists of a single Nafion tube. The aerosol flows through the inner part of the tube and is dried by adjusting the flow. Then, the scattering coefficient is measured by the nephelometer at a controlled RH. A second nephelometer measures the scattering coefficient at dry conditions. Combined temperature and capacitive RH sensors are used throughout the system and inside both nephelometers to measure air temperature and RH, respectively. In addition, these authors have installed a dew point sensor inside the nephelometer to accurately calculate the RH inside the nephelometer. Nevertheless, due to the relatively long time response of this sensor (up to several minutes) these RH readings are only applicable during stationary RH conditions. These authors observed a temperature difference of about 4.5 °C between the inlet and the sensing volume of the nephelometer at 16.6 lpm caused by the halogen lamp

(75 W) heating. Consequently, the RH decreases from e.g. 90% RH in the nephelometer inlet to about 70% RH in the sensing volume. In order to reduce this temperature difference, *Fierz-Schmidhauser et al.* [2010a] placed an air-cooled infrared filter between the lamp and the sensing volume. In addition, on the outside of the sensing volume they placed cooling fins to enlarge the surface, where four additional blowers adjusted the nephelometer's temperature close to room temperature. In the system of *Fierz-Schmidhauser et al.* [2010a] the highest RH is achieved before the drier. As a consequence, substances that may exist in two phases deliquesce if their DRH has been exceeded before the dryer. These particles remain liquid even if the RH is subsequently lowered on the way to the nephelometer. Thus, in laboratory studies they observed that the deliquescence step change appears at a lower RH than in the literature. In addition, due to the limited drying capability of the dryer, the ERH could not be observed during their laboratory and ambient measurements [*Fierz-Schmidhauser et al.*, 2010a; 2010b; 2010c; *Zieger et al.*, 2011; 2013].

The systems described above have been widely used for ground-based measurements. Several research groups have extensively deployed humidification systems for nephelometers on airborne platforms [*Hegg et al.* 2008; *Sheridan et al.* 2012]. Due to long scan times, scanning humidigraph systems are not practical for airborne applications. Thus, airborne measurements are usually performed with fixed humidity systems, where two or three nephelometers measure aerosol scattering at fixed RH levels [*Hegg et al.* 2002]. *Pekour et al.* [2013] have recently developed a new airborne humidification system in which three integrating nephelometers measure the scattering coefficient at three different fixed RH. The system of *Pekour et al.* [2013] consists of a number of specially designed exchanger cells (driers or humidifiers), that enables to measure $f(RH)$ under hydration or dehydration

conditions (always starting with the aerosol in a known state) with a simple system reconfiguration [*Pekour et al.*, 2013; *Shinozuka et al.*, 2013].

2.6 Parameterizations of $f(\text{RH})$

When scanning measurements are available it is possible to fit $f(\text{RH})$ versus RH curve (see Figure 2-6 as an example). Many different equations have been used in previous studies, being the simplest and most used equation the one-fit parameter equation [e.g., *Kotchenruther and Hobbs*, 1998; *Gassó et al.*, 2000] initially introduced by *Kasten* [1969]:

$$f(\text{RH}) = (1 - \text{RH} / 100)^{-\gamma} \quad \text{Eq. 2.7}$$

where γ parameterizes the magnitude of the scattering enhancement. *Sheridan et al.* [2002] used a variation of the equation proposed by *Kasten* [1969] based also in the γ parameter:

$$f(\text{RH}) = \left(\frac{1 - \text{RH}_{\text{wet}} / 100}{1 - \text{RH}_{\text{low}} / 100} \right)^{-\gamma} \quad \text{Eq. 2.8}$$

The two-fit parameters equation [e.g., *Clarke et al.*, 2002; *Carrico et al.*, 2003; *Zieger et al.*, 2011] introduces an additional parameter, a , that represents the intercept at RH=0%:

$$f(\text{RH}) = a(1 - \text{RH} / 100)^{-\gamma} \quad \text{Eq. 2.9}$$

Expressing $f(\text{RH})$ in terms of γ as shown in Eq. 2.7- Eq. 2.9 allows to extrapolate $f(\text{RH})$ to a broader range of RH values. *Zieger et al.* [2011] show that fitting the $f(\text{RH})$ -RH curve (so-called humidogram) for different RH ranges offers additional information about aerosol deliquescence state.

A different variation of the two-fit parameters equation can be found in the literature [*Kotchenruther and Hobbs*, 1998; *Carrico et al.*, 2003]:

$$f(RH) = 1 + a(RH / 100)^b \quad \text{Eq. 2.10}$$

More advanced multi-parameter equations have been proposed in the literature such as the three-fit parameters equation used by *Sheridan et al.* [2001] (Eq. 2.11) and by *Day et al.* [2000] (Eq. 2.12):

$$f(RH) = a(1 + b(RH / 100)^c) \quad \text{Eq. 2.11}$$

$$f(RH) = (d + eRH) / (1 + hRH) \quad \text{Eq. 2.12}$$

Kotchenruther et al. [1999] proposed the use of different fitting equations depending on the observed curve structure of the humidograms. For monotonic curves in which $f(RH)$ varies smoothly with RH and follows similar pathways on the upper and lower branches of the hysteresis loop they proposed the use of Eq. 2.10. For deliquescent curves, separate curve fits for the lower (Eq. 2.13) and upper branches of the hysteresis loop (Eq. 2.9) were proposed by these authors.

$$\begin{aligned} f(RH) = & \left[1 + a \left(\frac{RH}{100} \right)^b \right] \cdot \\ & \left[1 - \frac{1}{\pi} \left(\frac{\pi}{2} + \arctan(1 \times 10^{24} \left\langle \frac{RH}{100} - \frac{d}{100} \right\rangle) \right) \right] \\ & + c \left(1 - \frac{RH}{100} \right)^{-g} \cdot \\ & \left[\frac{1}{\pi} \left(\frac{\pi}{2} + \arctan(1 \times 10^{24} \left\langle \frac{RH}{100} - \frac{d}{100} \right\rangle) \right) \right] \end{aligned} \quad \text{Eq. 2.13}$$

The IMPROVE (Interagency Monitoring of PROtected Visual Environments) network (<http://vista.cira.colostate.edu>), recommends the following best-fit formula for the hygroscopic enhancement of aerosol scattering coefficient as a function of RH:

$$f(RH) = b_0 + b_1(1 - RH)^{-1} + b_2(1 - RH)^{-2} \quad \text{Eq. 2.14}$$

Koloutsou-Vakakis et al. [2001] proposed a polynomial fitting of $f(RH)$ as a function of RH as follows:

$$f(RH) = 1 + A_1RH + A_2RH^2 + A_3RH^3 \quad \text{Eq. 2.15}$$

As can be seen, many different choices are available in the literature for fitting $f(RH)$ as a function of RH. For many studies, the one or two fit-parameters equations were enough to describe the hygroscopic curve [*Kotchenruther and Hobbs*, 1998; *Sheridan et al.*, 2002, *Zieger et al.*, 2010; 2011] with no need of more complicated multi-parameter equations.

2.7 Possible sources of discrepancy among $f(RH)$ measurements

The measurements of the scattering enhancement factor are usually performed by custom-made humidifier systems and, as can be extracted from previous sections, differences in the experimental set-ups and measurement procedures may lead to differences in the reported $f(RH)$ values. In this section, we discuss possible sources of discrepancy between different $f(RH)$ measurements performed with different humidification systems for nephelometers and their influence on the calculated $f(RH)$.

2.7.1 Losses in the humidification system

Most published works have reported a good agreement between the reference and the humidified nephelometers when measuring at dry conditions (typically $RH < 40\text{-}50\%$), however, these differences ranged from below 2% up to 10% for PM_{10} scattering coefficients at ~ 550 nm wavelength, depending on the study. Usually, the differences were attributed to sampling losses in the humidification system that are thought to be size-dependent. Sampling losses are typically higher for PM_{10} than for PM_1 [e.g., *Carrico et al.*, 2000; *Carrico et al.*, 2003],

evidencing higher losses for larger particles. Apart of the losses in the humidification system, if the nephelometers are running in series instead of in parallel the losses may be even higher. In this sense, *Anderson and Ogren* [1998] observed differences around 7% and 1% for PM₁₀ and PM₁ size fractions for nephelometers running in series (without humidification system). Correcting for losses may be a very difficult task for RH higher than 40-50% due to water uptake by particles and different growth rates. Empirical corrections based on the comparison between both nephelometers at low RH have been used by some authors [e.g., *Pan et al.*, 2009; *Fierz-Schmidhauser et al.*, 2010b; 2010c]. Other authors reported a good agreement between both nephelometers at dry conditions but did not apply any corrections to the data [*Carrico et al.*, 2000; *Carrico et al.*, 2003], whilst other authors did not even report any comparison between the nephelometers. Corrected versus non-corrected measurements from sampling losses may result in discrepancies up to 10% (depending on the correction factors) in the reported $f(\text{RH})$ values. This discrepancy can be avoided if the fitting parameter γ is used to quantify the hygroscopic enhancement since this parameter does not change if a multiplicative correction factor is applied.

2.7.2 Effect of RH measurements on $f(\text{RH})$

It is clear that very accurate measurements of RH are needed in order to obtain accurate estimations of $f(\text{RH})$. For scanning RH measurements, the response time of the RH sensor should be taken into account. For TSI integrating nephelometers, the sample RH sensor has been proven to disagree with co-located RH sensors. In particular, *Fierz-Schmidhauser et al.* [2010a] reported an overestimation of 15% at high RH between the TSI sensor and a co-located sensor placed inside the nephelometer chamber. To illustrate the importance of

accurate RH measurements, Figure 2-6 shows a humidograph example of $f(RH)$ versus RH for 7 May 2014 10:00-10:30 GMT measured at Granada. The RH was measured inside the nephelometer (RH_TSI refers to the original TSI RH sample sensor and RH_wet refers to the co-located Rotronic sensor). The RH_TSI (accuracy $\pm 5\% \text{RH}$) was factory calibrated in July 2012 and the RH_wet (Rotronic Probes HC2-C04, accuracy $\pm 1.5\% \text{RH}$) sensor was calibrated and intercompared with a reference factory-calibrated RH sensor (Rotronic HygroClips HC2-S, accuracy of $\pm 0.8\% \text{RH}$) in April 2014.

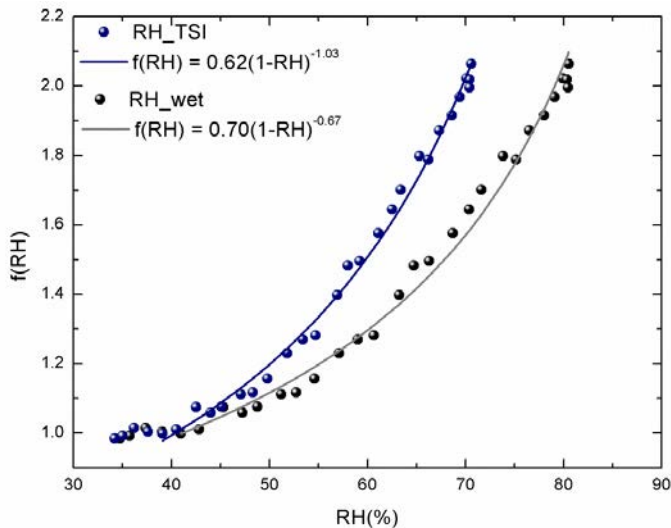


Figure 2-6: Humidograph example of $f(RH)$ versus RH for 7 May 2014 10:00-10:30 GMT. The RH was measured inside the nephelometer (RH_TSI refers to the original TSI RH sample sensor and RH_wet refers to the co-located Rotronic sensor).

Depending on the RH considered, the $f(RH)$ values changed from 2.06 using the RH measured with the RH_wet sensor to 3.07 using the RH measured with RH_TSI sensor. Concerning the γ parameter, differences up to 50% were observed depending on the RH sensor used (Figure 2-6), which evidences the high sensitivity of this parameter to RH sensor accuracy. Thus, a proper calibration of the internal RH sensor or co-locating additional more accurate

RH sensors inside the nephelometer chamber is highly recommended in order to obtain accurate estimations of the hygroscopic enhancement effect.

2.7.3 Different set point and reference RH values

The scattering enhancement factor is calculated as the ratio between the scattering coefficient at high (RH_{high}) and at low RH (RH_{low}). The choice of the high and low RH values depends on the specific work and has to be taken into account when comparing $f(\text{RH})$ values reported in the literature. The reference nephelometer is typically kept at RH below 40% although a constant RH in time is difficult to achieve. In this sense, some of the published works calculate $\sigma_{sp}(\text{RH}_{\text{low}})$ using the lower branch of the fitting curve and the derived fitting parameters [e.g., *Sheridan et al.*, 2001]. Other authors use as a reference the σ_{sp} measured below a certain RH_{low} value which is typically between 20-40% [e.g., *Carrico et al.*, 1998; *Pan et al.*, 2009; *Fierz-Schmidhauser et al.*, 2010b; 2010c; *Zieger et al.*, 2013]. This choice assumes that there is no scattering enhancement from 0 to 40% RH but it has the advantage that can be used when no scanning measurements are available. Concerning the RH_{high} value, the scattering enhancement factor is typically referred to 80, 82 or 85% RH, depending on the specific work. Apart of the different RH_{high} values that can be used, how the $f(\text{RH}_{\text{high}})$ values were calculated may also differ among works. In this sense, some authors adjusted the σ_{sp} to RH_{high} by using the upper branch of the $f(\text{RH})$ versus RH curve and the corresponding fitting parameters [e.g., *Sheridan et al.*, 2001; *Fierz-Schmidhauser et al.*, 2010b; 2010c], whilst other works used the σ_{sp} values for $\text{RH}_{\text{high}} \pm 2\%$ [e.g., *Fierz-Schmidhauser et al.*, 2010a]. In any case, the differences in the $f(\text{RH})$ using RH_{high} values from 80 to 85% RH are expected to be small, depending on the aerosol type, but within the uncertainty range of the measurements.

3 Experimental site and instrumentation

3.1 Site description

The station of the Atmospheric Physics Group (GFAT) is situated in the Andalusian Institute for Earth System Research, IISTA-CEAMA, located in Granada (37.16° N, 3.61° W, 680 m a.s.l.). Most of the measurements presented in this thesis were registered at this measurement station. Granada, located in South-eastern Iberian Peninsula, is a non-industrialized medium-sized city with a population of 240000 inhabitants that increases up to 350000 if the whole metropolitan area is considered [source: www.ine.es]. The city is situated in a natural basin surrounded by mountains with elevations between 1000 and 3500 m a.s.l. The near continental conditions prevailing at this site are responsible for large seasonal temperature differences, providing cool winters and hot summers. The area also experiences periods of low humidity regimes especially in summer. The study area is also at a short distance, about 200 km away, from the African continent and approximately 50 km away from the western Mediterranean basin. Due to its location in the Mediterranean basin, Granada is influenced by two major aerosol source regions: Europe as a major source of anthropogenic pollution and North Africa as a principal source of natural dust [*Lyamani et al., 2005; Lyamani et al., 2006*]. Furthermore, the Mediterranean area is characterized by a complex meteorology that favors the aging of polluted air masses in the basin and induces high level of airborne particles [*Lyamani et al., 2006; Lyamani et al., 2012*]. Thus, the Mediterranean basin can represent an additional source of atmospheric aerosol for the study area. In summer, the study area is isolated from travelling lows and associated frontal systems, and the intensification of the Azorean high during the warm season induces a very weak pressure gradient and strong subsidence that reduces entrainment from the free troposphere. In addition, local aerosol sources,

especially road traffic and domestic heating, contribute to the aerosol load over Granada.

At the station, air sampling for all the in-situ instruments is obtained from the top of a stainless steel tube of 20 cm diameter and 5 m length located at about 15 m above the ground. Measurements were performed neither with particle size cut-off and heating of sampled air. Inside this main stack, there are several stainless steel pipes that drive the sampling air to the different instruments. Different diameters of the pipes have been selected in order to optimize the efficiency of the system in terms of iso-kinetic sampling [Baron and Willeke, 2001].

3.2 Integrating nephelometer: working principle and calibration procedure.

(Adapted from TSI manual, 2009)

The integrating nephelometer (model TSI 3563) is able to measure particle light scattering (σ_{sp}) and back scattering (σ_{bsp}) coefficients at three wavelengths 450, 550 and 700 nm. A schematic representation of the TSI 3563 integrating nephelometer is shown in Figure 3-1. In this instrument, a small turbine blower draws an air sample (particle + gas) through the inlet into the measurement volume. There, the sample is illuminated over an angle of 7 to 170° with a quartz-halogen lamp (75 watt) equipped with a built-in elliptical reflector. The reflector focuses the light onto one end of an optical pipe where the light is carried into the internal cavity of the instrument. The optical pipe is used to thermally isolate the lamp from the sensing volume. The output end of the optical light pipe is an opal glass diffuser that acts as a cosine (Lambertian) light source. The sample volume is viewed by three photomultiplier tubes (PMT) through a series of apertures set along the axis of the main instrument

body. Scattered light is viewed against the backdrop of a very efficient light trap. The light trap, apertures, and a highly light-absorbing coating on all internal surfaces of the instrument combine to give a very low scatter signal from the walls of the instrument. The nephelometer design limits the angular integration of the scattered light to the 7° - 170° scattering angle range, leading to underestimations of scattering and backscattering coefficients, since part of forward (0° - 7°) and backward (170° - 180°) signals are not measured. For correction of this artifacts see section 3.2.1.

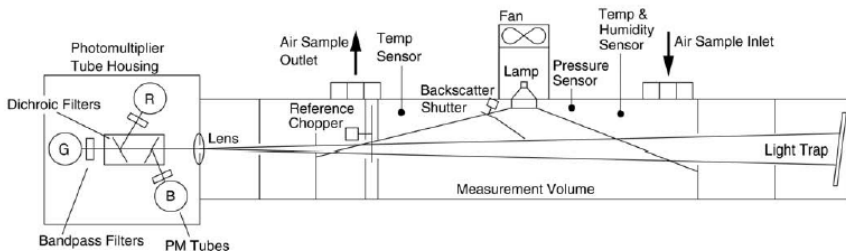


Figure 3-1: Schematic representation of the TSI 3563 integrating nephelometer.

Dichroic filters, in front of the PMT tubes, split and direct the light, which has been scattered by the sample. The light is directed into three bandpass filters: blue, green and red. A constantly rotating reference chopper which consists of three separate areas provides three types of signal detection (Figure 3-2). The first area gives a measure of the light-scattered signal. The second area blocks all light and prevents it to reach detectors. This area gives a measurement of the PMT dark current that is subtracted from the measurement signal. The third area is a translucent portion of the chopper, illuminated by the halogen lamp, which provides a measure of the light-source signal. This allows compensations for changes in the light source intensity and PMT detection efficiency.

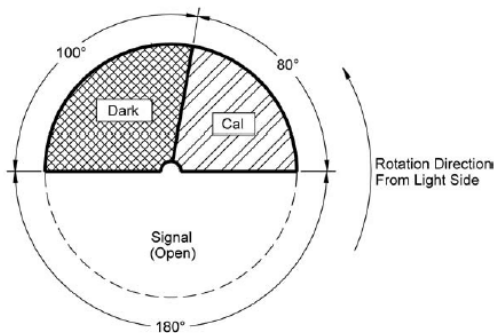


Figure 3-2: Schematic of the reference chopper

In backscatter mode, the backscatter shutter rotates under the lamp to block light in the 7 to 90° range. When light is blocked, only light scattered in the backward direction is transmitted to the PMT detectors. The backscatter signal can be subtracted from the total signal to calculate forward-scattering signal data. When this measurement is not of interest, the backscatter shutter can be “parked” in the total scatter position.

Periodically, an automated valve built into the inlet is activated to draw the air sample (aerosol + gas) through a high-efficiency (HEPA) filter. This gives a measure of the clean-air signal for the local environment. This signal is subtracted, along with the PMT dark-current signal, from the sample-scattered signal to give the aerosol scattered signal.

In the nephelometer, particles and gas molecules scatter photons that are detected and counted using highly sensitive photomultiplier tubes. The PMT produces electrical signals proportional to the intensity of the incident light. Hence the signal produced by the photomultiplier tube is proportional to the scattering coefficient of the air sample. The signals produced by PMTs are converted into scattering coefficients using calibration constants. These calibration constants are determined by filling the nephelometer with gases of

known but different scattering coefficients. The nephelometers used in this thesis were periodically calibrated using CO₂ and filtered air.

3.2.1 Nephelometer data correction

There are two main factors contributing to bias nephelometer sensitivity away from near-forward scattering: truncation error (the geometrical blockage of near-forward-scattered light for scattering angles below about 7° and above 170°) and nonlambertian error (the slightly noncosine-weighted intensity distribution of illumination light provided by the opal glass diffusor). With this in mind, it is clear that nephelometer measurements of σ_{sp} and σ_{bsp} contain systematic errors that must be corrected.

Several approaches have been proposed to correct nephelometer data [e.g. *Quirantes et al.*, 2008]. One of the most used correction scheme is the proposed by *Anderson and Ogren* [1998]. For correcting nephelometer data, these authors have defined a correction factor, C , as,

$$C = \sigma_{true} / \sigma_{neph} \quad \text{Eq. 3.1}$$

where σ_{true} is the Mie-calculated 0-180° or 90-180° scattering coefficient and σ_{neph} derives from a modified Mie-integral [Heintzenberg, 1978] using the measured angular sensitivity of the nephelometer. The correction method proposed by *Anderson and Ogren* [1998] involves the parameterization of the correction factor for total scattering as a linear function of the experimentally determined Ångström exponent (Table 3-1). Correction factor for total scattering coefficient exhibits a good relationship with Ångström exponent because both parameters are strong functions of particle size [*Anderson and Ogren*, 1998]. In contrast, correction factor for backscattering coefficient is close to unity (~0.98) and does not depend on Ångström exponent (i.e on particle size).

Nephelometer correction factors proposed by *Anderson and Ogren* [1998] for total scattering coefficient, and their associated uncertainties, are given in Table 3-1. These authors have calculated these corrections factors by assuming homogeneous spherical particles and bimodal, lognormal size distributions with geometric standard deviations of 1.8 and geometric volume mean diameters between 0.2 and 0.4 μm for the fine mode and 2 and 4 μm for the coarse mode. In addition, they assumed refractive indices ranging from 1.40 to 1.52 for the real part and from 0 to 0.01 for the imaginary part. These assumptions cover most aerosol populations outside of direct source plumes [*Anderson and Ogren*, 1998].

Table 3-1: Correction factors for total scattering as a function of the Angström exponent using $C = a + b \cdot SAE$ [Anderson and Ogren, 1998].

	450 nm		550 nm		700 nm	
	a	b	a	b	a	b
No cut	1.365	-0.156	1.337	-0.138	1.297	-0.113
Sub- μm	1.165	-0.046	1.152	-0.044	1.120	-0.035

3.3 Custom-built humidified nephelometer

(Adapted from Section 2 of “Study of the relative humidity dependence of aerosol light-scattering in southern Spain” by G. Titos, H. Lyamani, A. Cazorla, M. Sorribas, I. Foyo-Moreno, A. Wiedensohler and L. Alados-Arboledas, Published in Tellus B, 66, 24536, 2014).

The nephelometer tandem developed in the frame of this thesis and operated at the station of the Atmospheric Physics Group (GFAT), Andalusian Institute for Earth System Research (IISTA-CEAMA) in Granada, consists of two TSI 3563 integrating nephelometers running in parallel. A schematic representation of the experimental set-up is shown in Figure 3-3. One of the nephelometers measures the particle light scattering coefficient at dry conditions (reference nephelometer) and the second one measures at high RH with a humidification

system attached to the inlet (humidified nephelometer). Both nephelometers draw the ambient air at a flow rate of 15 l/min.

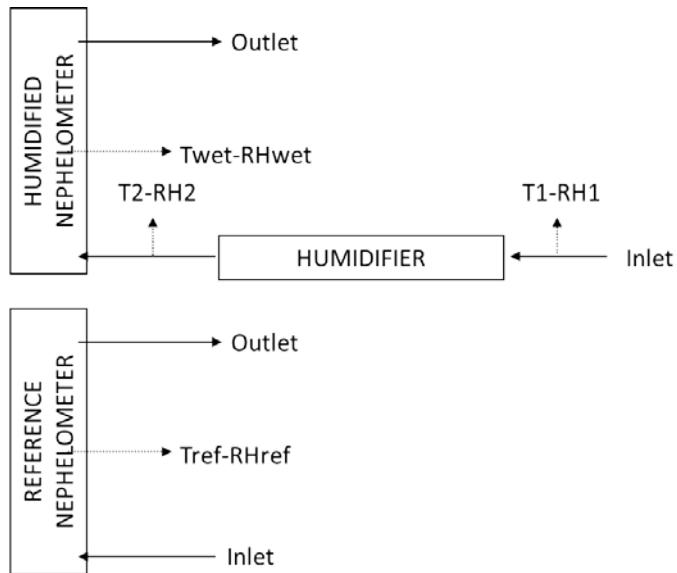


Figure 3-3: Schematic representation of the experimental set-up.

The humidifier consists of two concentric tubes: the inner one is a high density porous PTFE (polytetrafluoroethylene) tube of 15.5 ± 0.5 mm of inner diameter and 30 cm length (Figure 3-4). The pore size is large enough to allow the transfer of water molecules across the membrane, but too small for larger molecules to cross the barrier. The outer tube is made up of stainless steel and is wrapped in a cable heater (Figure 3-5) and insulation. There is a closed loop of water that circulates between the PTFE and the outer tube. As the water temperature increases, the RH of the sample air increases. The temperature of the water is regulated via a feedback system between the RH sensor, the PID (proportional-integral-derivative) controller and the heater. If the measured RH after the humidifier is below the set point the PID controller sends a signal to send current to the heater. The PID regulates the amount of current and heating rate of the humidifier heater until the desired set point is attained.



Figure 3-4: Outer and inner tubes constituting the humidifier. The inner one is a high density porous PTFE (polytetrafluoroethylene) tube and the outer tube is made up of stainless steel.

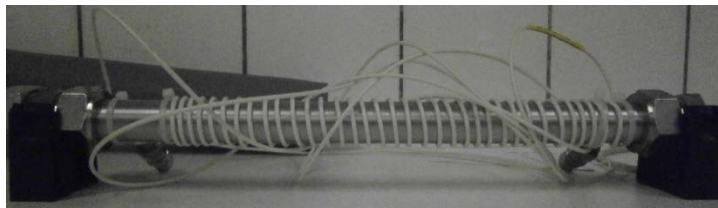


Figure 3-5: The outer stainless steel tube wrapped by a cable heater.

Figure 3-6 shows the control box of the humidifier system (frontal and upper views). In addition to the aforementioned PID controller to regulate RH values, another PID controller was installed as a safety feature to prevent overheating of the humidifier. This second PID acts as a cut-off switch on the humidifier heating. Above a certain set-point (typically, 50 °C) this switch will open and prevent current from passing through the heater. Another safety feature implemented in the control box is the use of a transformer that converts 220 Vac into 24 Vac, minimizing risks. In Figure 3-6 the red figure refers to the actual value and the green figure to the set-point. This set-point value can be fixed at a certain RH or can be scanned from low to high RH and vice versa. During the first year of operation, 2013, the set-point was set to a constant RH of 85%. In 2014, the control box was improved and connected with the NOAA LiveCPD software (Figure 3-7) to perform automatic scanning RH measurements. To this end, the software sends every minute a new set-point value to the PID controller based on a pre-defined schedule. Every hour the RH

measurement cycle starts with a zero measurement in the nephelometer and then the RH is increased stepwise to 80-85% within 30 min, and then decreased back to RH values of about 40% or below during the second half of the hour.

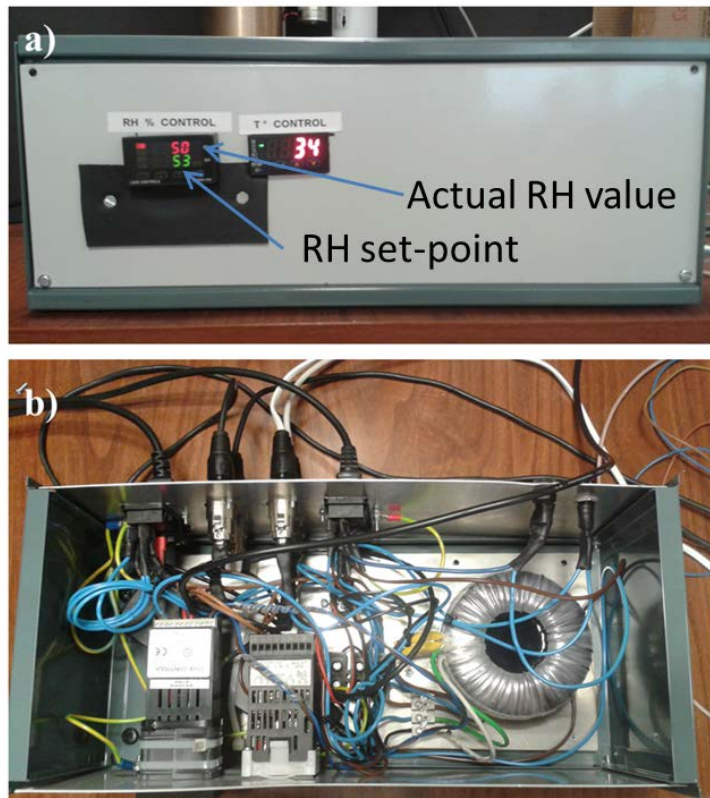


Figure 3-6: Control box for the humidifier system (frontal, a, and upper, b, views).

Temperature and relative humidity sensors (Rotronic HygroClips HC2-S, accuracy of $\pm 0.8\%$ RH and ± 0.1 K) are placed before and after the humidifier to measure air temperature and RH, before and after humidification, respectively (Figure 3-1). These T and RH measurements are recorded using a datalogger CR1000 (Campbell Sci.) that is also connected with the NOAA LiveCPD software. Since very precise measurements of the RH are needed for this study, two additional sensors (Rotronic Probes HC2-C04, accuracy ± 1.5

%RH and ± 0.3 K) have been placed inside the nephelometers' chamber, side by side to the original TSI sensor (sample sensor according to the TSI 3563 manual). Since the temperature measured by the TSI sensor is needed for calibration, the original sensor was also kept in the nephelometer. The Rotronic sensors were inter-compared prior to their installation in the nephelometers and in the humidification system showing a good agreement. The comparison between RH TSI and Rotronic sensors showed a good agreement for low relative humidity values while relative differences up to 12% were observed for $RH > 75\%$. Concerning the temperature measurements, the TSI sensor showed differences lower than 1% compared with the Rotronic sensor in the reference nephelometer whereas differences up to 6% were observed in the humidified nephelometer, probably due to more abrupt changes in temperature caused by heating in the humidifier. However, this difference in the temperature has a very small effect in the calculated particle light scattering coefficient. In fact, assuming a temperature difference of 6% at 300 K, this would cause an error smaller than 0.1 Mm^{-1} in the Rayleigh scattering at 550 nm, which can be considered as negligible. It is necessary to highlight that the temperature of the sampled air was kept below 34°C in order to minimize losses of volatile compounds [Bergin *et al.*, 1997; ten Brink *et al.*, 2000].

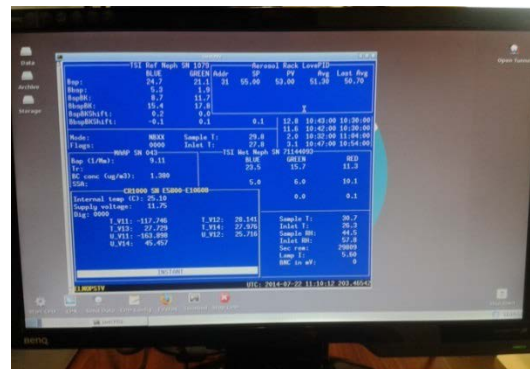


Figure 3-7: Main screen of the NOAA LiveCPD software.

The humidified and reference nephelometers measured at a frequency of 1 min and non-idealities due to truncation errors and non-Lambertian light source were corrected according to *Anderson and Ogren* [1998] as explained in Section 3.2.1. The uncertainty in σ_{sp} is about 7% [*Heintzenberg et al.*, 2006].

Laboratory measurements of well-defined monodisperse ammonium sulphate and sodium chloride particles were performed in order to test the capabilities of the humidification system. These measurements were performed at the facilities of the Leibniz Institute for Tropospheric Research (TROPOS) in Leipzig, Germany, and showed a good agreement between the experimental results and literature values. In this sense, the deliquescence relative humidity (DRH) was found to be 78% for $(\text{NH}_4)_2\text{SO}_4$ in comparison with literature values of 80% [*Tang*, 1996] and 79.5% [*Kus et al.*, 2004]. In the case of NaCl, the experimental DRH point was 75% which is in agreement with the values of 75% and 75.2% reported by *Tang* [1996] and *Kus et al.* [2004], respectively.

3.4 Multi-Angle Absorption Photometer

The particle light absorption coefficient, σ_{ap} , was measured with a Multi-Angle Absorption Photometer (MAAP) (Thermo ESM Andersen Instruments, Erlangen, Germany). Figure 3-8 shows the arrangement of the light source and the detectors in the MAAP optical sensor (left) and the physical realization of the instrument (right). In this instrument, particles are deposited on a quartz fiber filter and a continuous 637 nm laser [*Müller et al.*, 2011] illuminates the filter matrix perpendicularly. The decrease in the transmitted light through the filter is due to two factors: (1) absorption by the particles on the filter and (2) scattering by the particles and the filter matrix. The measurement of the radiation penetrating through the filter at the scattering angle $\theta = 0^\circ$, and the simultaneous measurement of the radiation scattered back from the filter at two

detection angles $\theta = 130^\circ$ and $\theta = 165^\circ$, permits the full determination of the irradiances in the forward and back hemisphere relative to the incident light beam [Petzold and Schönlinner, 2004].

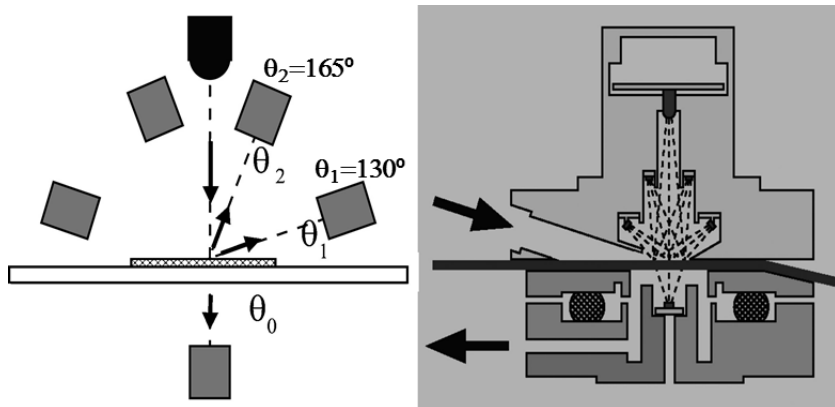


Figure 3-8: Optical sensor of the MAAP. Left: Position of the photodetectors at detection angles $\theta_0 = 0^\circ$, $\theta_1 = 130^\circ$ and $\theta_2 = 165^\circ$ with respect to the incident light beam. **Right:** Layout of the MAAP sensor unit, the arrows indicate the airflow through the sensor unit across the filter tape.

In the MAAP the determination of the particle light absorption coefficient of the deposited aerosol particles uses radiative transfer calculations and explicitly includes a treatment of backscattering effects from the filter matrix and the light scattering aerosol component [Petzold and Schönlinner, 2004]. The particle-loaded filter is treated as a two-layer system: the aerosol-loaded layer of the filter and the particle-free filter matrix. Radiative processes inside the layer of deposited aerosol and between this layer and the particle-free filter matrix are taken separately into account. Figure 3-9 gives a schematic representation of the main interaction processes that occurs in the system. The two reflectivity measurements allow correction for multiple scattering processes involving the deposited particles and the filter matrix.

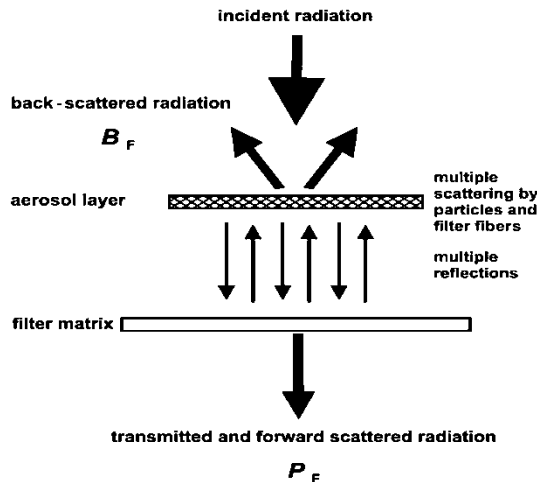


Figure 3-9: Schematic representation of radiation processes considered in the two-layer system consisting of an aerosol loaded filter layer and the particle-free filter matrix.

The MAAP draws the ambient air at constant flow rate of 16.7 l/min and provides 1 min values. *Petzold et al.* [2005] showed that the absorption coefficients measured by the MAAP are in good agreement with those measured simultaneously by photoacoustic spectrometry and by extinction minus scattering method. Furthermore, the MAAP filter based method does not require calibration for the measurement of the aerosol absorption coefficient and does not need co-located measurements of the aerosol light scattering coefficient [*Petzold and Schonlinner*, 2004; *Petzold et al.*, 2005] as occur with instruments like the aethalometer or the Particle Soot Absorption Photometer (PSAP). The total method uncertainty for the particle light absorption coefficient inferred from MAAP measurement is around 12% [*Petzold and Schonlinner*, 2004]. Mass absorption efficiency of $6.6 \text{ m}^2\text{g}^{-1}$, recommended by the manufacturer, is used in the MAAP internal computations to convert the measured absorption coefficient to Black Carbon (BC) concentration.

3.5 High-Volume samplers and chemical analysis

For sampling PM₁₀ and PM₁, two high-volume samplers (CAV-A/MSb and Digitel DHA-80) with a flow rate of 30 m³ h⁻¹ were used with quartz fibre filters at 24 hour time resolution. The sampling was carried out each 8 days in order to obtain a homogenous dataset, even though the sampling was more frequent during dedicated campaigns or special events. The filters were conditioned and treated pre- and post-sampling. For this end, the filters were placed in desiccators during 48 hours prior to weighting. The weighting was carried out at stabilized conditions (23 °C and 50% RH) using gravimetric technique.

A complete chemical analysis was performed for all samples following the procedure of *Querol et al.* [2001]. A fraction of each filter was acid digested (HF HNO₃:HClO₄, 5:2.5:2.5 ml) and the resulting solution was used to determine major and trace elements by Inductively Coupled Plasma Atomic Emission Spectrometry (ICP-AES) and Mass Spectrometry (ICP-MS). Another portion of the filter was water leached with de-ionized water in order to determine the concentration of different ions (Cl⁻, SO₄²⁻, and NO₃⁻) by ion chromatography and NH₄⁺ mass concentration by colorimetry (Flow Injection Analysis). A third portion of the filter was used to determine total carbon (C_t) content. From 2006 to July 2007 the total carbon mass concentration was determined using a LECO [*Querol et al.*, 2001], whilst since July 2007 the organic carbon (OC) and elemental carbon (EC) mass concentrations were determined separately by means of a thermo-optical transmission method using a Sunset Laboratory OCEC Analyser following the EUSAAR2 thermal protocol [*Cavalli et al.*, 2010]. For the first period, the non-mineral carbon (nmC) was estimated by subtracting the C associated to carbonates from the total carbon

content and for the second period it was calculated as the sum of EC and OC. OM+EC was estimated assuming a carbon multiplier of 1.4 to the measured OC ($1.4 \times OC + EC$) [Turpin *et al.*, 2000]. SiO_2 and CO_3^{2-} were indirectly determined on the basis of empirical factors ($SiO_2 = 3 \times Al_2O_3$ and $CO_3^{2-} = 1.5 \times Ca$; Querol *et al.*, 2001]. Marine sulphate ($SO_4^{2-}m$) concentration was calculated taking into account the Na/SO_4^{2-} molar ratio determined for seawater [Drever, 1982]. Non marine sulphate ($SO_4^{2-}nm$) was calculated as the difference between total sulphate and marine sulphate. PM_{10-1} mass concentrations were calculated as the difference between PM_{10} and the corresponding PM_1 mass concentrations. PM components were grouped as follows: mineral (ΣAl_2O_3 , SiO_2 , CO_3 , Ca, Fe, Mg, K), secondary inorganic aerosols, SIA, ($\Sigma SO_4^{2-}nm$, NO_3^- , NH_4^+), salt (ΣNa , Cl, $SO_4^{2-}m$), OC, EC and trace elements (ΣLi , P, Sc, Ti, V, Cr, Mn, Co, Ni, Cu, Zn, Ga, Ge, As, Se, Rb, Sr, Cd, Sn, Sb, Cs, Ba, La, Ce, Lu, Hf, Ta, W, Tl, Pb, Bi, Th and U).

4 Characterization of aerosol sources in Granada

In this chapter, the chemical composition of PM₁₀ and PM₁ samples collected at Granada during the period 2006-2010 is analyzed in detail. The chemical composition was obtained for all samples following the procedure of *Querol et al.* [2001]. The main goal of this study is to identify and apportion the main sources contributing to the aerosol coarse, PM₁₀₋₁, and fine, PM₁, fractions. To this end, the Positive Matrix Factorization technique was applied. This chapter is adapted from “*Identification of fine (PM₁) and coarse (PM₁₀₋₁) sources of particulate matter in an urban environment*” by G. Titos, H. Lyamani, M. Pandolfi, A. Alastuey, and L. Alados-Arboledas. Published in Atmospheric Environment, 89, 593-602, 2014.

4.1 Methodology: Positive Matrix Factorization technique

The fundamental principle of source/receptor relationships is that mass conservation can be assumed and a mass balance analysis can be used to identify and apportion sources of airborne particulate matter in the atmosphere. This methodology has generally been referred to as receptor modeling [*Hopke, 1985; 1991*]. A set of natural physical constraints must be considered in developing any model for identifying and apportioning the sources of airborne particle mass [*Henry, 1991*]. The fundamental, natural physical constraints that must be obeyed are:

- 1) The original data must be reproduced by the model.
- 2) The predicted source compositions must be non-negative; a source cannot have a negative percentage of an element.
- 3) The predicted source contributions to the aerosol must all be non-negative; a source cannot emit negative mass.
- 4) The sum of the predicted elemental mass contributions for each source must be less than or equal to total measured mass for each element.

The multivariate data analysis methods that are used to solve this problem are named as factor analysis. The most common form of factor analysis is Principal Components Analysis (PCA). *Paatero and Tapper* [1994] show that in PCA, there is scaling of the data by column or by row and that this scaling lead to distortions in the analysis. They further show that the optimum scaling of the data would be to scale each data point individually in order to have more precise data having more influence on the solution than points that have higher uncertainties. This problem was solved by an alternative formulation of the factor analysis called Positive Matrix Factorization (PMF). PMF model provides the chemical profile and contribution of the identified sources by decomposing the data matrix X ($n \times m$) where n and m are the number of samples and species, respectively, in two matrices of factor scores (source contribution), G ($n \times p$), and factor loading (source profile), F ($p \times m$), according to Eq. 4.1 [*Paatero and Tapper*, 1994; *Paatero*, 1997]:

$$X_{ij} = \sum_{k=1}^p f_{kj} g_{ik} + e_{ij} \quad \text{Eq. 4.1}$$

where p is the number of factors extracted and e_{ij} are the elements of the matrix of residuals E (difference between measured and calculated species concentrations), X_{ij} is the j_{th} elemental concentration measured in the i_{th} sample, f_{kj} is the fractional concentration ($\mu\text{g}/\mu\text{g}$) of species j_{th} in the emissions from the k_{th} source, and g_{ik} is the airborne mass concentration ($\mu\text{g}/\text{m}^3$) of material from the k_{th} source contributing to the i_{th} sample.

The task of PMF is to minimize the objective function Q with respect to G and F with the constraint that each of the elements of G and F is to be non-negative and where σ_{ij} are the elements of the uncertainty matrix.

$$Q = \sum_{i=1}^n \sum_{j=1}^m \frac{e_{ij}^2}{\sigma_{ij}^2} \quad \text{Eq. 4.2}$$

The minimization of Q is based on the error-weighted least squares method. The calculation of the matrix σ is a crucial point so that the model gives the right weight to the input data and consequently the most reliable results. There are several sources of error contributing to the overall uncertainty of the ambient measurements but the one associated with the analytical procedure is likely to be one of the most important sources of uncertainty [Amato *et al.*, 2009a]. In the present study, the matrix σ for PM₁ and PM₁₀ fractions was calculated following the procedure described by Amato *et al.* [2009a] and Escrig *et al.* [2009] which is a similar methodology than the one described by Thompson and Howarth [1978], obtaining the fitting equation:

$$\sigma_a^2 = \sigma_0^2 + (\alpha m)^2 \quad \text{Eq. 4.3}$$

where σ_a is the uncertainty associated with analytical procedure, m is the mass of analyte in the filter and σ_0 and α are fitting parameters [Thompson, 1988]. In addition, the analytical determination also includes the subtraction of blank filters that were different filters from the sampled ones. The blanks cause an additional source of uncertainty σ_{blk} that has to be propagated jointly with σ_a to obtain the analytical determination uncertainty σ_A :

$$\sigma_A^2 = \sigma_a^2 + \sigma_{blk}^2 \quad \text{Eq. 4.4}$$

In order to include additional sources of uncertainty apart from the analytical ones, the overall uncertainty was expanded by the following formula:

$$\sigma_{ij}^2 = \sqrt{\frac{\sigma_A^2}{V_i^2} + (\beta x_{ij})^2} \quad \text{Eq. 4.5}$$

where V_i is the air volume sampled and β is a coefficient that was estimated to be 0.15 which might accounts for any other additional sources of uncertainty [Amato *et al.*, 2009a]. The uncertainty estimate (Eq. 4.5) provides a criterion to separate the species which retain a significant signal from the ones dominated

by noise. The applied formula gives higher relative errors for small concentration data near the limit of detection. The uncertainties for the PM₁₀₋₁ fractions were calculated by propagating the errors calculated for the PM₁ and PM₁₀ fractions with the above described methodology. The number of species used within the PMF model was selected by looking at their signal-to-noise ratio (S/N) which provides a criterion to separate the species which retain a significant signal from the ones dominated by noise. The S/N was calculated as described by *Paatero and Hopke*, [2003], considering the matrix N as the uncertainty matrix σ :

$$S/N = \sqrt{\frac{\sum x_i^2}{\sum \sigma_i^2}} \quad \text{Eq. 4.6}$$

Only species with S/N values higher than 2 were selected for the present study, thus species with weak signal were not introduced in the model [*Paatero and Hopke*, 2003]. Moreover, the percentage of data above detection limit (%ADL) was used as complementary criterion for species selection. The combination of both criteria resulted in the selection of 24 species in PM₁ and 22 species in PM₁₀₋₁. Two species (As and NH₄⁺) were included in PM₁ and removed from PM₁₀₋₁ given that these two elements were found mainly in the finest fraction. In order to avoid bias in the results the data matrix was uncensored, i.e. negative values and data below detection limits were included as such in the analysis without substituting them with below detection limit indicators [*Paatero*, 1997]. The PM₁ matrix included 163 cases and 24 variables whilst the PM₁₀₋₁ matrix consisted of 130 cases and 22 variables. Table 4-1 reports means, standard deviations, medians, percentage of data above detection limit (% ADL) and signal-to-noise ratios (S/N) for the selected elements.

Table 4-1: Mean, standard deviation (SD), percentage of data above detection limit (% ADL) and uncensored signal-to-noise ratio (S/N) for the elements in the PM₁₀₋₁ and PM₁ fractions included in the PMF analyses.

	PM ₁				PM ₁₀₋₁			
	Mean ($\mu\text{g}/\text{m}^3$)	SD ($\mu\text{g}/\text{m}^3$)	%ADL	S/N	Mean ($\mu\text{g}/\text{m}^3$)	SD ($\mu\text{g}/\text{m}^3$)	%ADL	S/N
Al ₂ O ₃	0.2	0.5	37	3.8	2	3	100	8.1
Ca	0.2	0.2	46	2.4	3	2	98	8.4
K	0.3	0.2	57	3.4	0.5	0.4	73	5.4
Na	0.1	0.2	26	2.3	0.5	0.5	69	5.6
Mg	0.05	0.07	44	1.9	0.7	0.6	98	7.8
Fe	0.06	0.10	66	6.3	0.8	0.8	100	8.7
Mn	0.002	0.003	18	2.7	0.02	0.02	88	7.8
Ti	0.005	0.010	42	5.8	0.07	0.09	98	8.7
V	0.004	0.002	100	8.2	0.01	0.01	98	8.4
Ni	0.003	0.003	26	2.1	0.002	0.003	56	2.0
Cu	0.004	0.004	96	7.2	0.02	0.02	100	8.3
As	0.0003	0.0002	28	1.9				
Rb	0.0003	0.0003	39	2.7	0.002	0.002	88	7.6
Sr	0.001	0.002	18	2.2	0.02	0.03	93	8.1
Sn	0.0005	0.0002	26	1.6	0.003	0.001	98	7.0
Sb	0.0005	0.0006	90	8.1	0.003	0.002	100	8.4
Pb	0.004	0.003	100	7.7	0.005	0.006	98	8.1
Se	0.0002	0.0001	86	6.2	0.0003	0.0002	87	7.3
La	0.0001	0.0002	55	2.0	0.0006	0.0007	29	3.2
SO ₄ ²⁻	2	1	100	7.9	2	2	98	7.9
NO ₃ ⁻	1	1	99	7.9	2	1	99	7.9
Cl	0.1	0.3	42	2.1	0.3	0.5	45	2.0
NH ₄ ⁺	0.6	0.6	100	4.8				
Ct	5	3	99	2.4	4	3	89	5.3

The PMF2 model was run in robust mode [Paatero, 1997] for source identification and apportionment. The optimal number of sources was selected by inspecting the variation of object function Q from PMF with varying number of sources (from 3 to 6) and by studying the physical meaningfulness of the calculated factors. In the present work, 5 and 4 sources were selected for PM₁₀₋₁

and PM_1 , respectively. The theoretical value of Q should be approximately equal to the number of degrees of freedom of the system $[n \times m - (p \times (n+m))]$ [Paatero *et al.*, 2002] where n, m and p are the number of samples, species and factors respectively. In PM_1 (with p=4) and PM_{10-1} (with p=5) the degrees of freedom were 3356 and 2320, respectively, close to the calculated Q (3626 and 2586 for PM_1 and PM_{10-1} , respectively). Moreover, in PM_1 and PM_{10-1} the solution with 5 and 6 factors, respectively, led to additional factors without a meaningful chemical profile both being loaded with almost all used species. One additional criteria used to evaluate the meaningfulness of the calculated sources was the inspection of the scaled residuals. In both fractions the selected number of factors led to solutions with 90–100% of the scaled residuals located between the optimal range –2 and +2 [Juntto and Paatero, 1994]. In general, this type of bilinear factor analysis has rotational ambiguity: there will not be a unique solution even though there will be a global minimum in the least-squares fitting process. The addition of constraints can reduce the rotational freedom in the system, but non-negativity alone does not generally result in a unique solution. One of the key features of PMF is that the rotations are part of the fitting process and are not applied after the extraction of the factors. One of the ways that rotations can be controlled in PMF2 is by using the parameter FPEAK. The FPEAK rotations were made in order to explore alternative solutions. Thus, once the number of sources was selected, the rotational ambiguity was handled by means of this FPEAK parameter by studying the variation in the Q values by varying FPEAK from –0.8 and +0.8.. The issue of local minimum was assessed by running 20 times the FPEAK=0 solution with different pseudorandom initializations. After regression of the factor scores from PMF (G matrix) to PM mass the model was able to simulate on average

100% and 97 % of measured PM_{10-1} and PM_1 mass, respectively, with coefficients of correlation of 0.97 (PM_{10-1}) and 0.75 (PM_1).

4.2 PM concentration: major and trace elements

Mean (\pm standard deviation) PM levels measured at Granada urban station for the entire observation period 2006-2010 were $40 \pm 30 \mu\text{g}/\text{m}^3$ and $17 \pm 9 \mu\text{g}/\text{m}^3$ for PM_{10} and PM_1 , respectively. The PM_{10} levels obtained in our site were within the range observed in other urban background stations across Spain (30-46 $\mu\text{g}/\text{m}^3$) by *Querol et al.* [2008] for the period 1999-2005; but slightly higher compared to other European cities [*Putaud et al.*, 2010]. Usually, PM_{10} mass concentrations were higher in Southern Europe than in Northwestern and Central Europe and in kerbside and urban stations than in other stations [*Querol et al.*, 2008; *Putaud et al.*, 2010]. The coarse (PM_{10-1}) mass concentration was determined as the difference between the PM_{10} and PM_1 mass concentrations for simultaneous samples. PM_{10-1} was mainly composed by mineral matter (around 62%) and non mineral carbon, nmC, (12%) whilst PM_1 was composed mainly by nmC (32%) and secondary inorganic aerosols, SIA, that contributed around 20%. The mineral matter concentration obtained in this work was larger than those found by *Querol et al.* [2008] at different Spanish stations. The contribution of mineral particles to PM_{10} levels in Granada was slightly higher than the contribution obtained at road side sites (26 - 36%) and at urban sites in the Iberian Peninsula (20 - 33%) [*Querol et al.*, 2008]. Lower contributions of mineral particles to the PM_{10} fraction were also reported for urban and kerbside stations across Europe [*Putaud et al.*, 2010].

Figure 4-1 shows the chemical speciation of PM_{10-1} and PM_1 fractions during winter (November-February) and summer (May-August). This separation can offer an insight in the possible sources and processes affecting

coarse and fine PM. Also the partitioning between PM_1 and PM_{10-1} (expressed through the ratio $\text{PM}_1/\text{PM}_{10}$) can help to elucidate the origin of the elements analyzed (Figure 4-2). Mineral matter was mainly in the coarse mode and its contribution to this fraction was higher in summer than in winter (Figure 4-1). Figure 4-2 also evidences this fact; most of the crustal elements presented low $\text{PM}_1/\text{PM}_{10}$ ratios denoting that those elements are mainly in the coarse fraction. The higher contribution of mineral matter to PM_{10-1} in summer can be due to the drier conditions that favor re-suspension of dust from roads and soils as well as to the dust intrusions from North Africa that are very frequent in Granada during summer season [Valenzuela *et al.*, 2012].

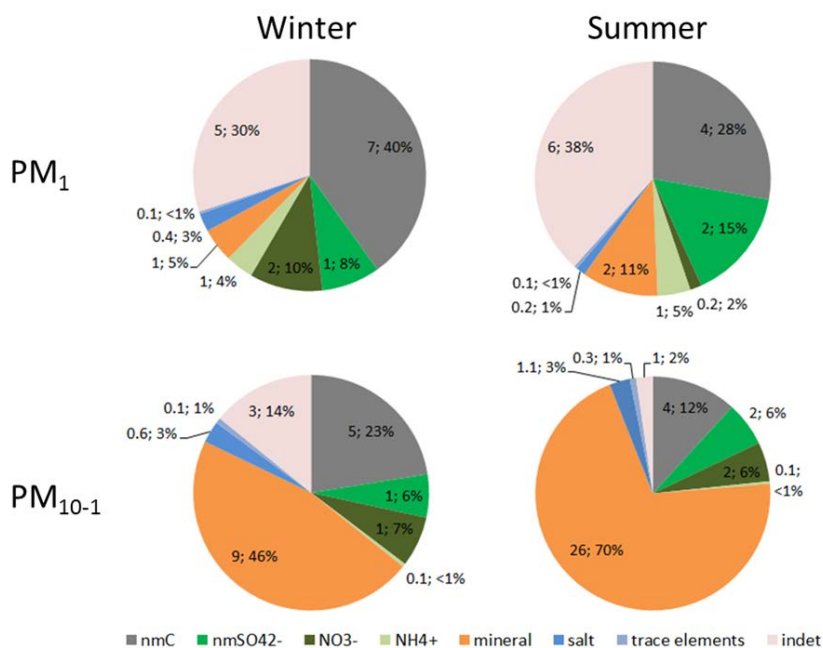


Figure 4-1: Chemical composition of PM_{10-1} (lower panel) and PM_1 (upper panel) in winter and in summer expressed in $\mu\text{g}/\text{m}^3$ and percentage (%).

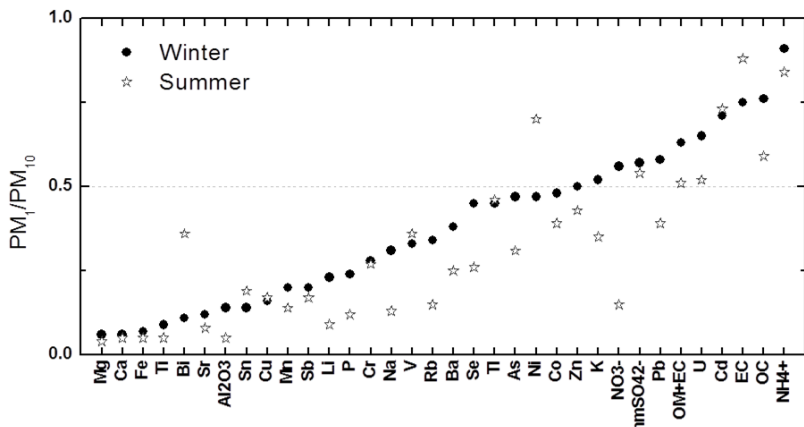


Figure 4-2: PM₁/PM₁₀ ratios of the major and some trace elements.

The contribution of nmC to PM₁ fraction was higher than the contribution to PM₁₀₋₁ and also higher in winter than in summer. This seasonality of carbonaceous material is typical of urban sites and may be due to the increase in anthropogenic emissions (fuel based domestic heating) and lower mixing layer heights during winter season [Granados-Muñoz *et al.*, 2012] that favor accumulation of particles near urban sources. In addition, during winter time, stagnant episodes associated with thermal inversions and low wind speeds are also very frequent producing a large increase in particle matter load near the ground [Lyamani *et al.*, 2012].

Non marine sulphate was present in both PM fractions, with slightly higher contribution in PM₁ than in PM₁₀₋₁. This constituent doubled its contribution to PM₁ during summer due to the higher SO₂ oxidation rates under high insolation conditions and low regional air mass renovation in summer [Pey *et al.*, 2009]. On the contrary, nitrate contribution to PM₁ decreased considerably during summer due to the thermal instability of the ammonium nitrate in summer [Harrison and Pio, 1983; Querol *et al.*, 2008]. Nitrate contribution to PM₁₀₋₁ did not vary significantly between seasons compared with its contribution to PM₁ and presented a PM₁/PM₁₀ ratio around 0.56 in

winter and 0.15 in summer denoting that in summer nitrate was mainly in the coarse fraction whilst in winter was predominantly in the fine one. Coarse nitrate is formed by interaction between HNO_3 and coarse marine (sodium chloride) or mineral (calcium carbonate) particles giving rise to the formation of Na and/or Ca nitrates explaining the higher concentrations of coarse nitrate observed in summer [Tobo *et al.*, 2010].

Most trace elements presented relatively low concentrations compared with the typical values observed in other Spanish urban stations [Querol *et al.*, 2008]. Elements associated with road traffic such as Cu and Sb from brake abrasion [Schauer *et al.*, 2006], Ba and Zn from tire abrasion [Wahlin *et al.*, 2006] and Ti, Li, and Rb, among others, from road pavement abrasion [Querol *et al.*, 2008; Amato *et al.*, 2011] tended to accumulate in the coarse fraction (50 to 90%). On the other hand, Ni presented a higher $\text{PM}_1/\text{PM}_{10}$ ratio ranging from 0.5 during winter to 0.7 in summer. Other elements associated with industrial processes like As, Pb, Cd and U [Querol *et al.*, 2008] mostly accumulate in the fine fraction. Most elements presented higher $\text{PM}_1/\text{PM}_{10}$ ratios during winter compared with summer, except Bi, Sn, V, Ni and EC. A different seasonality in the $\text{PM}_1/\text{PM}_{10}$ ratio may suggest differences in the sources contributing to these compounds in winter and in summer (see next section). A similar seasonal behavior for the $\text{PM}_1/\text{PM}_{10}$ ratios for Ni, Sn, EC and V was also observed in Switzerland by Minguillón *et al.* [2012].

Mean PM_{10} annual levels decreased from $50 \pm 30 \text{ } \mu\text{g/m}^3$ in 2006 to $40 \pm 30 \text{ } \mu\text{g/m}^3$ in 2010. Meteorological conditions and emissions are competitive processes determining the magnitude of PM concentrations in the atmosphere. Thus, the year to year variability observed in PM_{10} levels could be related to inter-annual variations in emissions sources or to changes in the meteorological and synoptic conditions, or to both. In order to detect possible trends in PM_{10}

and PM₁ component levels, the Mann-Kendall test has been applied to the annual average values. This test reveals a significant decreasing trend (at 0.1 significance level) in PM₁₀ and mineral matter concentrations. Saharan dust intrusions over Granada have a large impact on the PM₁₀ and PM₁ levels and their constituents [Calvo *et al.*, 2010; Mladenov *et al.*, 2011]. Thus, part of the observed year to year variations in PM₁₀ and PM₁ component levels could be due to the inter-annual variation in the frequency and intensity of Saharan dust events. In order to discard the variability caused by African dust events, the samples collected under those conditions have been excluded. A total of 134 PM₁₀ samples were collected under African dust free conditions (www.calima.ws). Under these conditions, significant decreasing trends at 0.05 significance level were obtained for PM₁₀ mass concentration, mineral matter, nmC and V and at 0.1 significance level for SIA, Cu and Pb. No trends were obtained for trace elements such as Ni, Sn, Sb, Co, Zn or Cr. Lyamani *et al.* [2011] reported that equivalent black carbon mass concentrations decreased on 2008 due to the decrease in anthropogenic activities in Granada. The current work shows that this decrease has continued until 2010 and that other anthropogenic pollutants have also decreased. On the other hand, annual PM₁ levels did not experience any significant temporal trend according to the Mann-Kendall test. Recent studies of Barmpadimos *et al.* [2012] and Cusack *et al.* [2012] have reported a decreasing trend in PM_{2.5} levels at regional stations across Europe for the periods 1998-2010 and 2002-2010, respectively. In the study of Barmpadimos *et al.* [2012] the decrease observed in PM_{2.5} was more pronounced than the decrease observed for PM₁₀ levels. However, in Granada, the decrease was mainly observed in the PM₁₀ fraction. This discrepancy could be ascribed to different sampling sites between studies (regional versus urban) and to different size fractions (PM_{2.5} versus PM₁). Thus, we believe that the

observed decrease in PM₁₀ and its constituents may be related, in large part, to a decrease in the anthropogenic activities although part of the observed decrease may be also due to the inter-annual change in the meteorological conditions.

4.3 Apportionment and seasonality of the sources identified by PMF technique

Five PM₁₀₋₁ and four PM₁ sources were identified by PMF analysis. Figure 4-3 and Figure 4-4 show the profiles of each source in the coarse and fine fractions, respectively, and the percentages of species apportioned by each source. The sources identified in the coarse fraction were named as mineral dust, regional re-circulation, aged regional, road dust and celestite mines. Fine PM sources were mineral dust, regional re-circulation, traffic exhaust and road dust. Although some sources were identified in both fractions the use of fine and coarse PM in the PMF analysis allows us to identify additional sources.

- **Mineral dust:** The mineral source was identified in both fractions and was characterized by crustal elements (Al₂O₃, Ca, Mg, Fe, Ti, Sr). This source might have contribution of both local (re-suspension from soils and construction activities) and long-range transported dust aerosols. It comprised 36 and 22% of the total mass in the coarse and fine fractions, respectively. It is necessary to highlight the high contribution of this source to the fine fraction since mineral matter commonly accumulates in the coarse fraction [Song *et al.*, 2012]. Some authors [Minguillón *et al.*, 2012; Perrone *et al.*, 2013; Cusack *et al.*, 2013] have identified mineral sources by applying PMF. However, none of them reported such high contributions to the fine fraction. This high contribution to the fine fraction may be ascribed to contamination of the source profile although the profile was not cleaner for other FPEAK values. The presence of SO₄²⁻ and C in the mineral PM₁ profile could be due to: 1)

Neutralization of sulfuric acid with available ions such as Ca^{++} and Na^+ (also present in the mineral PM_1 profile) and 2) Contamination by C due to condensations of organic precursors on large surface mineral particles. Using PMF analysis the contribution of mineral matter doubled the contribution calculated as $\Sigma \text{Al}_2\text{O}_3$, SiO_2 , CO_3 , Ca, Fe, Mg, K. Concerning the seasonality of this source, it showed a higher contribution to PM in summer than in winter probably connected with the higher frequency of African dust events during spring and summer and with the dryness of the soil which favor re-suspension processes.

- **Road dust:** The road dust source was slightly different for each size fraction. In PM_1 it was mainly characterized by carbonaceous particles and Sb (90% of the total variance of Sb) whereas in the coarse fraction it was typified by carbonaceous material and road tracers like Fe, Cu, Sn, Sb and Pb [Amato *et al.*, 2009b]. This source was predominantly in the coarse fraction, comprising 8% and 24% of the total fine and coarse PM, respectively. It presented a similar seasonality in both fractions with higher contribution to the coarse and fine mass in winter (48% and 11%, respectively) with respect to summer (12% and 7%, respectively) (Figure 4-5). The interpretation of this source is supported by wind sector analysis (Figure 4-6), since the polar plots show higher concentrations for low wind speeds and for southwesterly winds (in the direction of the highway). A similar contribution of road dust to PM_{10} was obtained in a traffic influenced site located in the northern part of the city [Amato *et al.*, 2013].

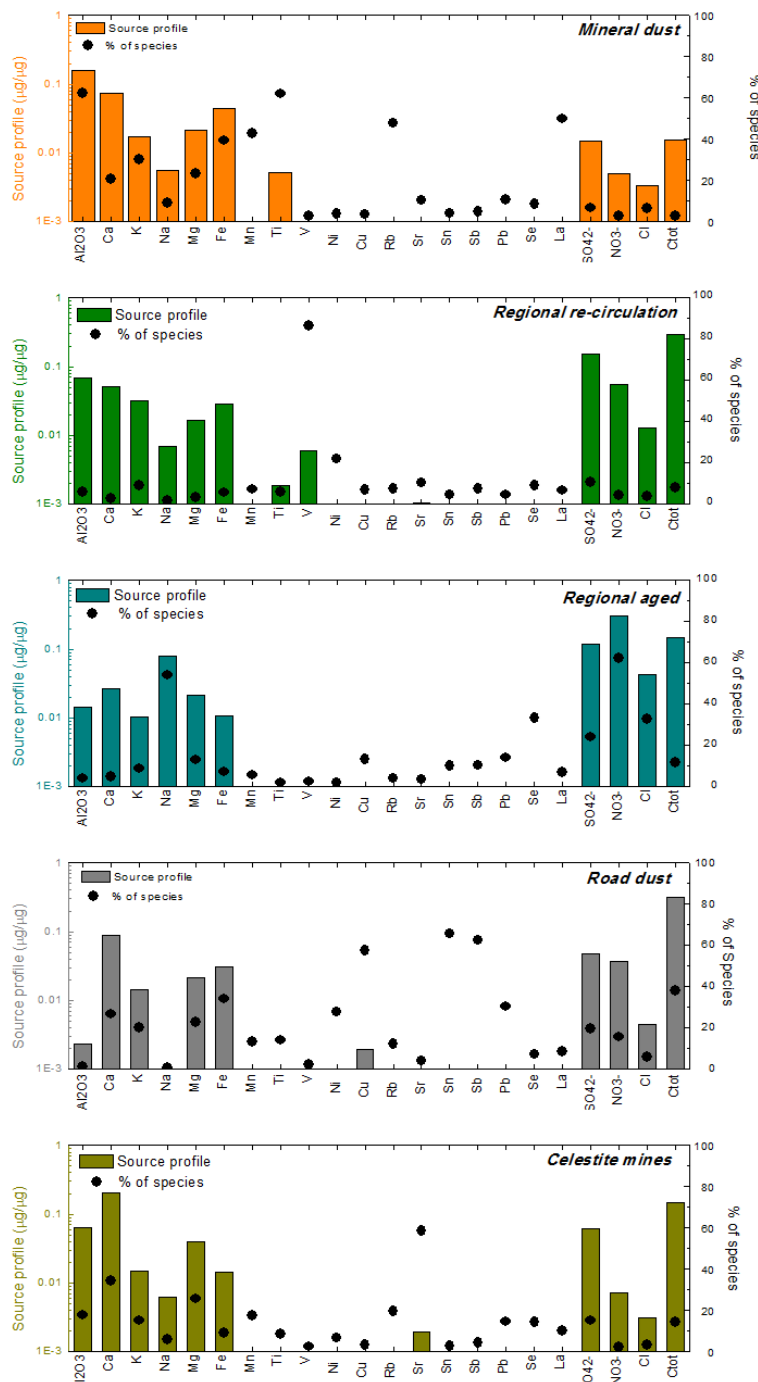


Figure 4-3: Source profiles found for the coarse fraction (PM_{10-1}) and percentage of ambient species concentration apportioned by each source.

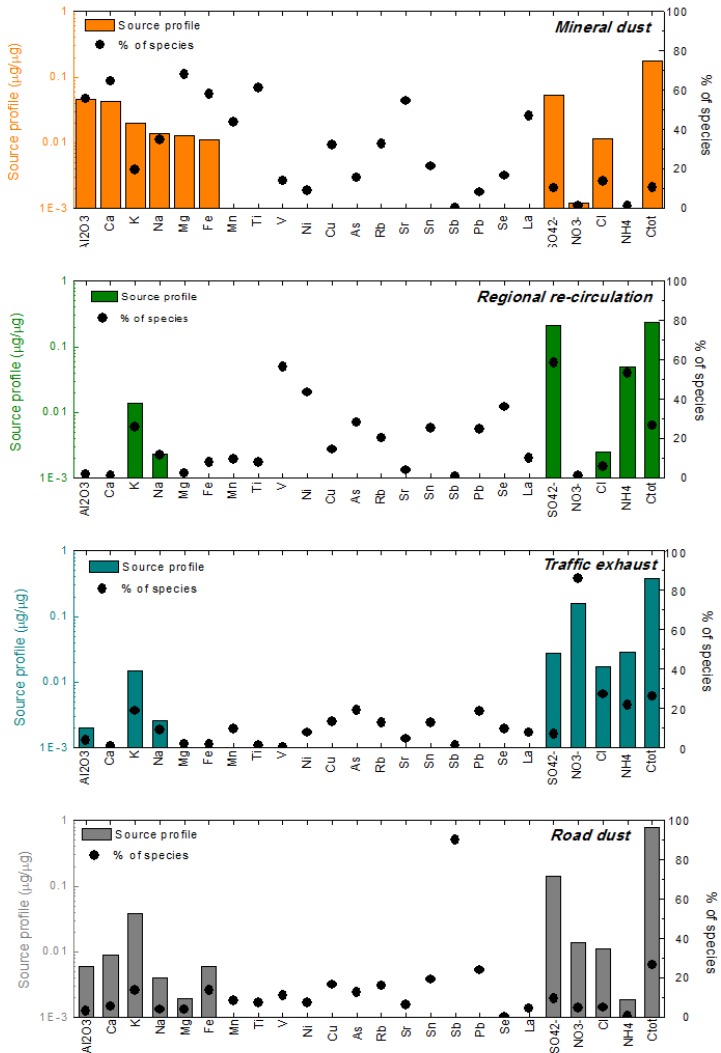


Figure 4-4: Source profiles found for the fine fraction (PM_1) and percentage of ambient species concentration apportioned by each source.

-Traffic exhaust: This source was only identified in the fine fraction and it was characterized by nitrate, ammonium and carbonaceous particles, comprising 29% of the fine mass. This source explained 86% of variance in nitrate that in urban environments is mainly attributed to vehicle exhaust [Almeida *et al.*, 2006]. The presence of some road tracers confirms the traffic

origin of this source. The higher contribution in winter can be connected with higher emissions together with lower mixing layer heights [*Granados-Muñoz et al.*, 2012] that favor accumulation of pollutants near the surface. In addition, fine nitrate concentrations could increase in winter due to the thermal stability of particulate nitrate. In this sense, it is important to have in mind that the formation of secondary products from primary emissions depends on the season and that primary products are not always transformed into the same compounds in the atmosphere. The polar plots (Figure 4-6) and the seasonality of this source and the road dust source are very similar, confirming a common source.

- **Regional re-circulation:** This source is traced by secondary sulphate (mainly in the form of ammonium sulphate), V and Ni. It is the most important source concerning PM₁ mass concentration, comprising 41% of the total mass in this fraction. Secondary sulphate, V and Ni are commonly associated with fuel-oil combustion and used as tracers for domestic heating and traffic sources [e.g. *Calvo et al.*, 2013]. In addition, high concentrations of V, Ni and sulphate, especially during summer season, are commonly reported in Mediterranean environments associated with re-circulation processes [*Pey et al.*, 2013]. The seasonality of the regional re-circulation source (Figure 4-5) with higher contribution in summer (9.5 µg/m³ in PM₁ and 2.0 µg/m³ in PM₁₀₋₁) compared to winter (4.0 µg/m³ and 1.1 µg/m³ in PM₁ and PM₁₀₋₁, respectively) suggests that an important part of this source may be ascribed to regional pollution and long range transport, especially in summer, although in winter it may be ascribed to domestic heating, being the PMF analysis unable to distinguish between both sources. In this sense, also the variations in the PM₁/PM₁₀ ratios of V and Ni in summer and winter (Figure 4-2) evidence differences in the sources contributing to these compounds depending on the season.

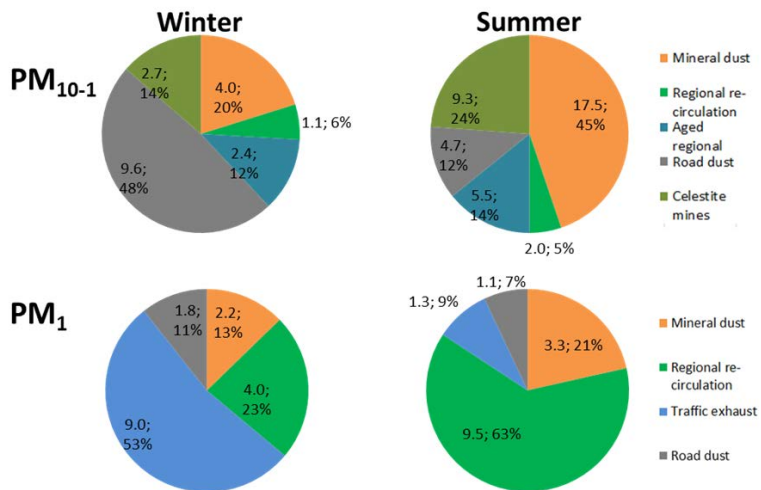


Figure 4-5: Contribution of sources to PM_{10.1} (upper panel) and PM₁ (lower panel) in winter (left) and summer (right) expressed in µg/m³ and corresponding percentage.

- **Aged regional:** This source was typified by nitrate, sulphate, Na, Cl, Se and Ct, and has been interpreted as aged regional, being only identified in the coarse fraction. Its seasonality is characterized by a relatively high contribution during the warm season (14%, 5.5 µg/m³) compared with winter (12%, 2.4 µg/m³). It is thought to be related with the interaction of secondary compounds (sulphates and nitrates) with mineral matter and marine aerosols. Regional re-circulation processes together with Saharan dust intrusions (both more frequent in summer season) may favor this interaction. In fact, the presence of coarse nitrate in this source (62% of the variance) is thought to be related with the aforementioned formation of Ca(NO₃)₂ during dust events due to the interaction of mineral dust with anthropogenic pollutants [Tobo *et al.*, 2010].

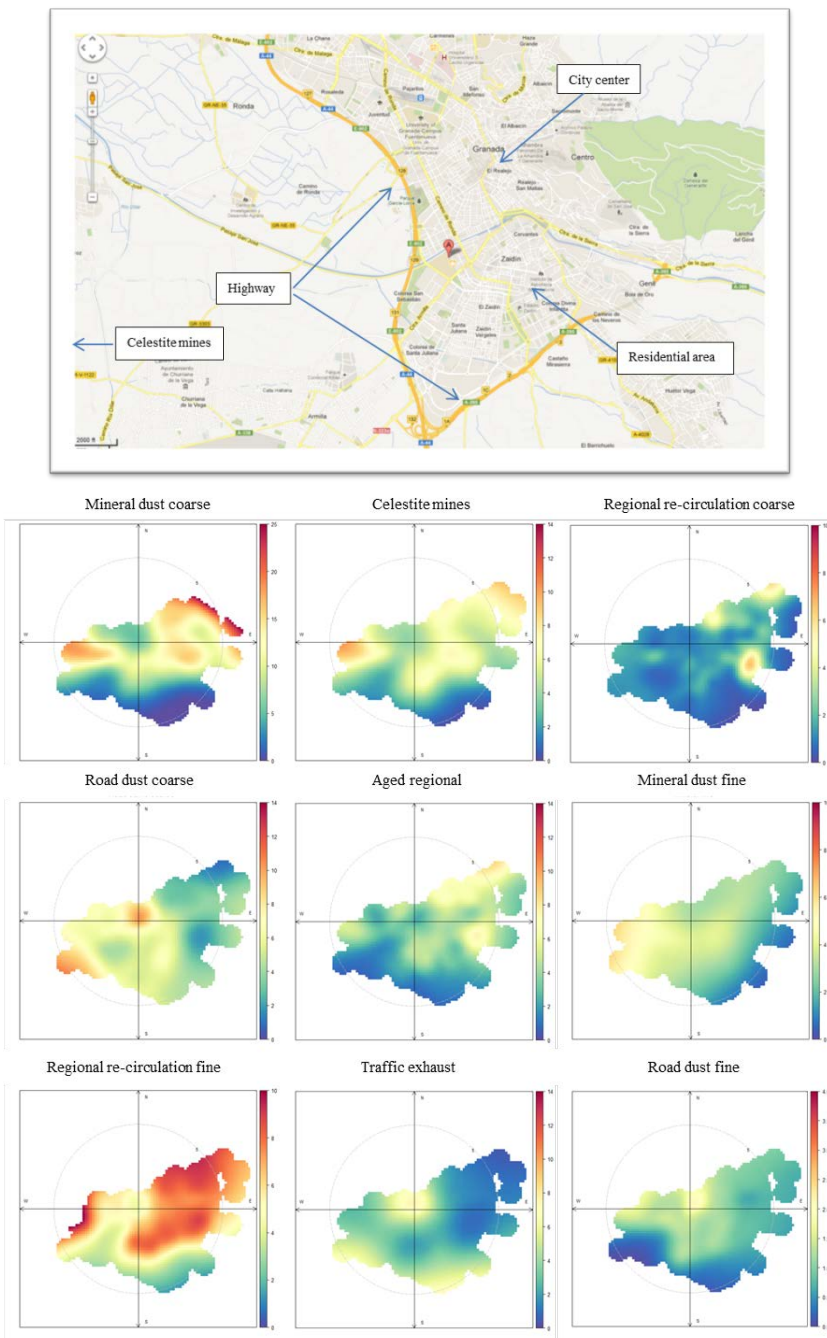


Figure 4-6: Location map (top) of the monitoring site and polar plots (bottom) of the PM source concentration in $\mu\text{g}/\text{m}^3$ (color scale) obtained with PMF according to wind direction.

- **Celestite mines:** The main tracers of this source were sulphate, strontium and crustal elements (mainly Ca and Mg). It was named as celestite mines because it was thought to be related with celestite mines located 20 km south-west of the city. Celestite (SrSO_4) is a mineral consisting of strontium sulphate and is the principal source of the element strontium, commonly used in fireworks and in various metal alloys. This source was only distinguished in the coarse fraction and its mass contribution to this fraction was 20%. This source displayed a seasonal pattern characterized by higher values in summer compared with winter, which could be explained since the mines are open-pit mines, so re-suspension is enhanced during summer. In addition, the fields surrounding the mines would be enriched in Sr, thus agricultural activities in the area will also favor re-suspension of this element. The highest concentration of this source was obtained for westerly and south-westerly winds, where the mines are located (Figure 4-6) although relatively high concentrations were also observed for winds from the east sector. This may be due to the contribution of other mineral compounds to this source as can be seen in Figure 4-3.

4.4 Working versus non-working days variability

The average contribution of the different sources for working days (from Monday to Friday), Saturday and Sunday is shown in Figure 4-7. For the coarse fraction a total of 92 data points are included in the average for Monday-Friday, 20 for Saturday and 18 for Sunday. In a similar manner for the fine fraction 119, 25 and 19 data points are included in the averages for Monday-Friday, Saturday and Sunday, respectively. It is important to take into account the sampling interval of the filters (24 hours starting at 7:00 GMT). In particular, filters collected on Sunday include partially the traffic peak of Monday morning.

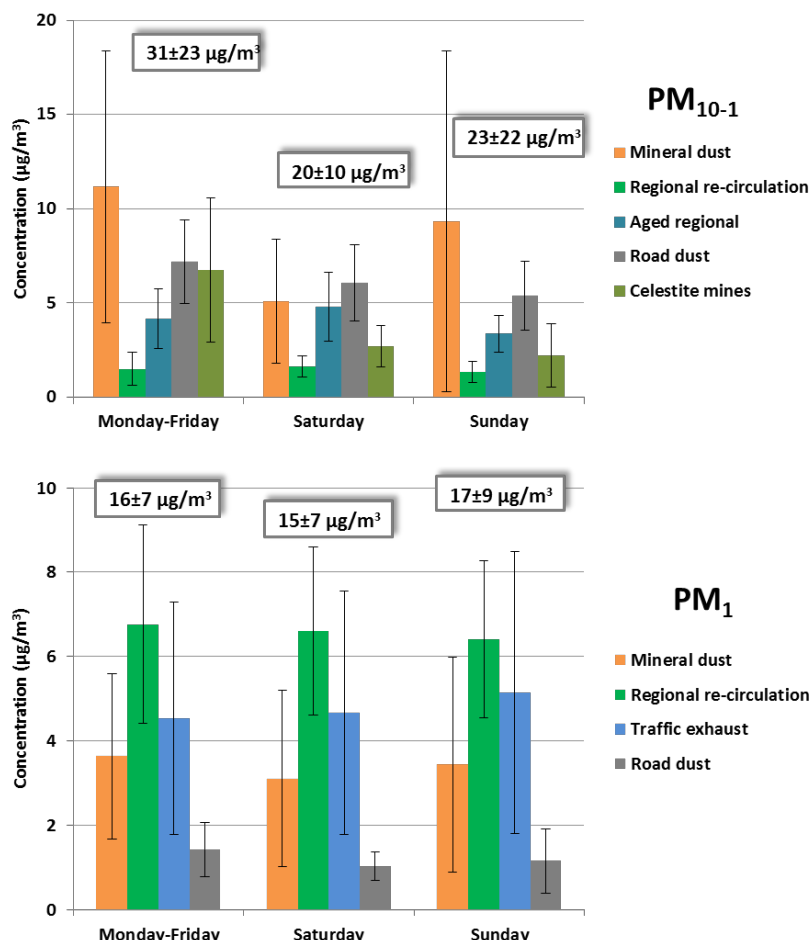


Figure 4-7: Average concentrations of each source for Monday to Friday, Saturday and Sunday, for the coarse fraction (upper panel) and for the fine fraction (lower panel). The error bars represent the standard deviations (SD). The average \pm SD measured PM mass concentration for each period is also shown in a box.

PM_{10-1} experienced a large decrease from weekdays ($31\pm23 \mu\text{g}/\text{m}^3$) to Saturdays ($20\pm10 \mu\text{g}/\text{m}^3$), showing also less variability on Saturdays. On Sundays, the average PM_{10-1} mass concentration increase compared to Saturdays, probably due to the contribution of traffic peak of Monday mornings. The largest decrease was observed for the mineral dust source that decreased from an average value of $11\pm7 \mu\text{g}/\text{m}^3$ on Monday-Friday to 5 ± 4

$\mu\text{g}/\text{m}^3$ on Saturdays. Celestite mines source also decreased considerably on Saturdays, denoting a reduction in the working activity of the mines during the weekend. Taking into account the standard deviations, the decrease observed in the contributions of the celestite mines source was more pronounced than in the mineral dust source. Road dust source experienced a slight decrease during the weekend whilst regional re-circulation and aged regional sources did not change significantly from weekdays to weekends. Concerning the fine fraction, PM_1 levels, as well as the concentrations of each source, did not vary between weekdays and weekends. It is necessary to mention that part of the variability between working and non-working days may be biased by the lower number of samples collected during Saturdays and Sundays. So, reducing anthropogenic activity (like it is supposed to occur on Saturdays) will have a positive impact in PM_{10} levels. However, in the short term the PM_{10} reduction was mainly observed in the coarse fraction, whereas the fine fraction remains at the same levels during the weekends.

4.5 Daily exceedances: natural or anthropogenic?

Air quality has been a cause of concern during the past decades throughout the world, especially in developed countries. In particular, PM has become a key pollutant due to its negative effects on human health and many countries have developed abatement strategies in order to control PM levels. Therefore, one of the main aims of source apportionment studies is to identify the causes of exceedance of the thresholds established by the European Directive (2008/50/EC for PM_{10} and $\text{PM}_{2.5}$; no regulation concerning PM_1). A total of 40 PM_{10} daily exceedances have been recorded during the study period, with most of them occurring during spring and summer seasons (15 and 12, respectively). From the 27 daily exceedances occurred in spring and summer, 22 occurred

during African dust events (www.calima.ws). On average, the ratio fine/coarse mass concentration was 0.5 during the exceedances occurred in spring and summer and the mineral dust source accounted for 24% of the measured PM₁ and 48% of PM₁₀₋₁. For the 13 days exceeding the PM₁₀ daily limit during autumn and winter, road dust and mineral dust sources comprised 42 and 29% of the coarse fraction; and traffic exhaust and regional re-circulation accounted for 55% and 23% of the total PM₁, respectively. The fine/coarse ratio was on average 0.9, during those days. Thus, exceedances associated with a natural origin were more frequent during spring and summer and presented a higher impact on the coarse fraction. On the other hand, exceedances related to anthropogenic origin predominantly affected the fine fraction and occurred more often during the cold seasons. With these results in mind, traffic is the main source to target in Granada throughout the year, but especially in winter. In this sense, *Qadir et al.* [2013] detected a decrease of 60% in the contribution of traffic source after the implementation of a low emission zone in Munich, evidencing that this kind of measures may help to reduce pollution levels in urban areas.

4.6 Conclusions

The chemical composition of fine and coarse particulate matter has been studied for the period 2006-2010 at an urban station in southern Iberian Peninsula. A significant decreasing trend in PM₁₀ levels has been observed related with a decrease in most of its constituents, specially marked in mineral matter levels and nmC. The concentrations of chemical constituents were found to undergo a clear seasonal behavior. The coarse fraction was mainly composed by mineral matter, which increased considerably during summer due to the drier conditions that favor re-suspension from roads and soils and the more frequency of African

dust events. Non-mineral carbon was the major contributor to the fine fraction and presented higher levels in winter than in summer mainly due to larger emissions during winter and lower mixing layer heights that favor accumulation of particles near surface.

Concerning the identification of sources, PMF analysis distinguished five sources in PM_{10-1} and four in PM_1 . The use of fine and coarse PM in the PMF analysis allows the identification of additional sources that could not be identified using only one size fraction. The mineral dust source was identified in both fractions and comprised 36 and 22% of the total mass in the coarse and fine fractions, respectively. This high contribution of the mineral source to the fine fraction may be due to contamination of the source profile. The regional recirculation source was traced by secondary sulphate, V and Ni. It was the most important source concerning PM_1 mass concentration being less important in the coarse fraction. Although V and Ni are commonly associated to fuel oil combustion the seasonality of this source with higher concentrations in summer compared with winter suggest that the most important part of this source can be ascribed to regional pollution episodes. The traffic exhaust source that was characterized by nitrate, ammonium and carbonaceous particles, comprised 29% of the fine mass. Finally, celestite mines source was traced by sulphate, strontium and crustal elements (mainly Ca and Mg) and it was only identified in the coarse fraction.

A reduction in PM_{10-1} levels from working to non-working days has been observed, especially due to reduction in the contribution of mineral dust, celestite mines and road dust sources. On the other hand, PM_1 levels and the contribution from the different sources remain fairly constant throughout the week. PM_{10} exceedances (2008/50/EC) associated with a natural origin were more frequent during spring and summer and presented a higher impact on the

coarse fraction, whereas exceedances related to anthropogenic origin predominantly affected the fine fraction and occurred more often during the cold seasons. Concluding, traffic seems to be the main source to target in Granada throughout the year, but especially in winter. Since no significant temporal trend or changes between working and non-working days have been observed in the fine fraction, it is clear that further investigation is needed concerning PM₁ fraction and its sources in order to establish future abatement strategies.

5 Relationship between aerosol optical properties and chemical composition

This chapter focuses on the investigation of the relationship between aerosol particles optical properties and their chemical speciation by means of the study of the aerosol mass efficiencies. To this end, aerosol optical properties, mass concentration and chemical composition measured at Granada from March 2006 to February 2007 were analysed. Aerosol particles light-scattering and absorption coefficients were measured with an integrating nephelometer and a Multi-Angle Absorption Photometer (MAAP), respectively. PM₁₀ and PM₁ samples were collected with two high volume samplers, and the chemical composition was investigated for all samples (refer to Section 3 for further information on the instrumentation and techniques). This chapter is adapted from “*Optical properties and chemical composition of aerosol particles at an urban location: an estimation of the aerosol mass scattering and absorption efficiencies*” by G. Titos, I. Foyo-Moreno, H. Lyamani, X. Querol, A. Alastuey and L. Alados-Arboledas. Published in Journal of Geophysical Research, vol. 117, D04206, 2012.

5.1 Methodology: aerosol mass efficiencies

The simultaneous measurements of aerosol mass concentration and scattering/absorption coefficients allowed the estimation of the mass scattering/absorption efficiencies (α_{sp} and α_{ap}). There are four basic approaches to estimate α_{sp} and α_{ap} [Hand and Malm, 2007]: (1) *Theoretical Method* consists in the application of Mie calculation based on measurements of size distributions of particle mass or number concentration and assumed refractive index [Ouimette and Flagan., 1982; White, 1986; Lowenthal et al., 1995]; (2) *Partial Scattering Method* estimates the change in extinction due to the removal or addition of a single species [Lowenthal et al., 1995] (3) *Measurement Method* defines the mass scattering efficiency of an aerosol population as the

ratio of the scattering coefficient corresponding to the mass concentration of that population; (4) *Multilinear Regression* (MLR) method consists in a multiple linear regression with measured scattering or absorption coefficients as the independent variable and measured mass concentrations for each species as the dependent ones [White *et al.*, 1994; Lowenthal *et al.*, 1995; Formenti *et al.*, 2001; Andreae *et al.*, 2002]. Due to the data available both the measurement and MLR methods were applied. Many authors have reported the limitations and requisites of MLR method [Ouimette and Flagan, 1982; White, 1986; Lowenthal *et al.*, 1995; Vasconcelos *et al.*, 2001; Hand and Malm, 2007]. The assumptions required in this method are that all the aerosol species contributing to extinction are included in the model and that the concentrations of the species are uncorrelated. In addition, the number of samples has to be large enough in order to obtain stable solutions. The mass efficiencies derived with this method are subject to a variety of errors. For example, for species with lower measurement uncertainties (e.g., sulphate) the mass scattering efficiencies obtained can be artificially high, while for species with larger measurement uncertainties (e.g., organic matter) may be artificially too low [White and Macias, 1987]. Furthermore, the apportionment of scattering by more than one species to total scattering depends on whether the aerosols are externally or internally mixed [White, 1986]. In this sense, when assuming an internal mixture the efficiencies obtained correspond only to the specific mass efficiencies of the mixed aerosol. Regarding the measurement method, the mass efficiencies derived also correspond to the specific mass efficiencies of the mixed aerosol and represent average conditions of an aerosol that could be changing because of variations (such as meteorology or composition) during the sampling period. The measurement method is the simplest one for computing

mass efficiencies and can be performed when no speciation or size resolved data are available.

5.2 Overview: Chemical composition and aerosol optical properties

During the study period (from March 2006 to February 2007), the average (\pm standard deviation) PM₁₀ and PM₁ mass concentrations at Granada were 44 \pm 19 $\mu\text{g}/\text{m}^3$ and 15 \pm 7 $\mu\text{g}/\text{m}^3$, respectively. The coarse (PM₁₀₋₁) mass concentration presented a mean value of 30 \pm 19 $\mu\text{g}/\text{m}^3$, ranging between 4 and 87 $\mu\text{g}/\text{m}^3$. Both coarse and fine mass concentrations presented a clear seasonality. The coarse mass concentration was high in spring and summer while the fine mass concentration presented high values in autumn and winter. These results are very similar to those obtained using long term dataset from 2006 to 2010 (see section Section 4.2).

Speciation data from PM₁₀, PM₁ and PM₁₀₋₁ fractions is presented in Table 5-1. Figure 5-1 shows the contribution of the different compounds to the coarse and fine fractions. Mineral matter was the major constituent in the PM₁₀ fraction with a mean value of 19 \pm 15 $\mu\text{g}/\text{m}^3$ (Table 5-1), contributing more than 43% to this fraction. The contribution of this constituent to the fine mode was much smaller (around 10%) than the contribution to the coarse mode (58%), as could be expected since the mineral dust has a dominant coarse grain size. During summer, when the re-suspension from the ground is higher and the dust outbreaks are more frequent the mineral matter contributed more than 68% to PM₁₀₋₁ fraction. Secondary inorganic aerosols, SIA, accounted for around 17% of PM₁₀ fraction with a mean concentration of 8 \pm 3 $\mu\text{g}/\text{m}^3$ (Table 5-1) and accounted for over 24% of PM₁ fraction (Figure 5-3). Non marine sulphate was predominantly in the fine fraction, contributing 5.9% and 14.0% to PM₁₀₋₁ and PM₁ fractions, respectively.

Table 5-1: Basic statistical summary (mean value, standard deviation, maximum and minimum values) of the mass concentrations (in $\mu\text{g}/\text{m}^3$) for the major chemical species measured in PM_{10} , PM_1 and PM_{10-1} in Granada. N is the number of samples analysed.

	PM_{10}			PM_1			PM_{10-1}			
	Mean \pm SD	Max	Min	Mean \pm SD	Max	Min	Mean \pm SD	Max	Min	
N		62			66			55		
PM	44 \pm 19	98	15	15 \pm 7	34	5	30 \pm 19	87	4	
SiO_2	7 \pm 7	34	0	0.5 \pm 0.5	1.9	0	7 \pm 7	34	0	
CO_3^{2-}	5 \pm 3	15	0	0.3 \pm 0.3	1.4	0	4 \pm 3	14	0	
Al_2O_3	2 \pm 2	11	0	0.2 \pm 0.2	0.6	0	2 \pm 2	11	0	
Ca	3 \pm 2	10	0	0.2 \pm 0.2	0.9	0	3 \pm 2	10	0	
K	0.8 \pm 0.4	1.8	0.2	0.3 \pm 0.2	0.9	0.1	0.5 \pm 0.3	1.6	0.1	
Mg	0.8 \pm 0.5	2.2	0.1	0.05 \pm 0.05	0.22	0	0.8 \pm 0.5	2.2	0.1	
Fe	0.9 \pm 0.6	3.3	0.1	0.06 \pm 0.05	0.22	0	0.9 \pm 0.6	3.3	0.1	
Na^+	0.5 \pm 0.3	1.4	0.1	0.05 \pm 0.02	0.1	0.02	0.5 \pm 0.3	1.4	0.1	
Cl^-	0.4 \pm 0.3	1.6	0.0	0.08 \pm 0.09	0.46	0.01	0.3 \pm 0.3	1.6	0.0	
$\text{SO}_4^{2-}_{\text{m}}$	0.1 \pm 0.1	0.4	0.0	0.01 \pm 0.01	0.03	0	0.1 \pm 0.1	0.4	0.0	
$\text{SO}_4^{2-}_{\text{nm}}$	4 \pm 2	10	2	2 \pm 1	5	1	2 \pm 1	8	0	
NH_4^+	0.6 \pm 0.4	1.8	0.1	0.5 \pm 0.3	1.6	0	0.1 \pm 0.3	1.0	0	
NO_3^-	3 \pm 2	8	1	1 \pm 1	6	0	2 \pm 1	5	0	
Mineral	19 \pm 15	69	2	2 \pm 1	6	0	19 \pm 15	69	1	
OM+EC	14 \pm 5	34	6	7 \pm 3	21	3	7 \pm 3	16	1	
Sea Spray	1.0 \pm 0.6	3.4	0.3	0.1 \pm 0.1	0.5	0.1	0.9 \pm 0.6	3.4	0.1	
SIA	8 \pm 3	15	3	3 \pm 2	11	1	4 \pm 2	12	1	
Metals	0.3 \pm 0.2	1.0	0.1	0.05 \pm 0.02	0.14	0.01	0.3 \pm 0.2	1.0	0	

Organic matter and elemental carbon, OM+EC, accounted for around 31% of PM_{10} fraction and for 43% of PM_1 fraction. This constituent is mainly in the fine fraction since its contribution to the coarse fraction (21.5%) is much lower than the contribution to the fine fraction. The contributions of OM+EC particles to both the fine and coarse fractions increased considerably during winter.

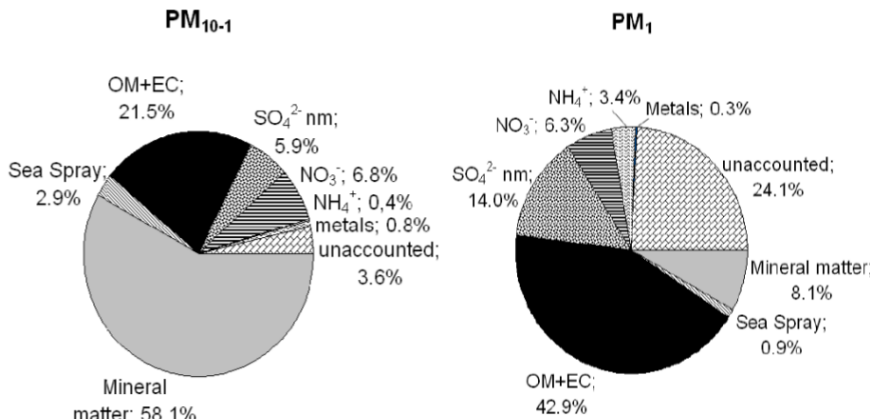


Figure 5-1: Annual mean composition in % of PM₁₀₋₁ and PM₁ fractions for the period from March 2006 to February 2007.

Figure 5-2 shows the daily variability of the light scattering and absorption coefficients for the period from March 2006 to February 2007. The relative humidity within the nephelometer chamber was below 50% during the study period. We have selected those days with simultaneous measurements of light scattering and absorption coefficients and PM₁₀ and PM₁ mass concentrations ($N = 47$). The data represent averages for the same periods over which the aerosol samples were collected. Table 5-2 presents a statistical summary of the aerosol optical properties obtained during the study period. The mean daily values of $\sigma_{sp}(550 \text{ nm})$ ranged between 25 and 128 Mm⁻¹ with a mean value and standard deviation of $61 \pm 25 \text{ Mm}^{-1}$ while $\sigma_{ap}(550 \text{ nm})$ was in the range 11–50 Mm⁻¹, with a mean value of $24 \pm 9 \text{ Mm}^{-1}$. These mean values are in accordance with previous results ($\sigma_{sp}(550 \text{ nm}) = 60 \pm 17 \text{ Mm}^{-1}$ and $\sigma_{ap}(670 \text{ nm}) = 21 \pm 10 \text{ Mm}^{-1}$) obtained in Granada during a longer study period [Lyamani *et al.*, 2010].

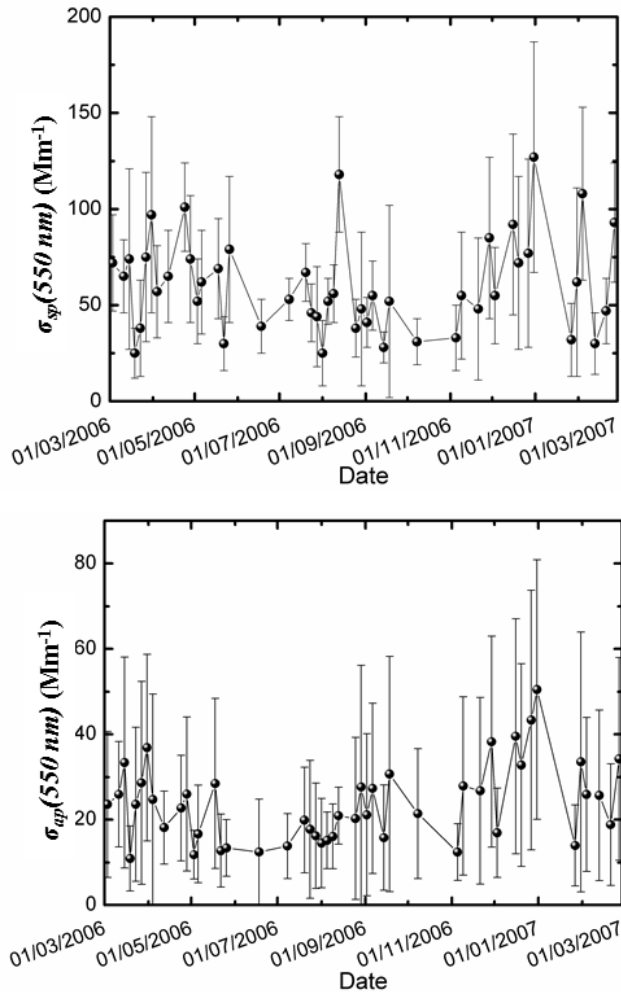


Figure 5-2: Daily mean value and standard deviation of $\sigma_{sp}(550 \text{ nm})$ and $\sigma_{ap}(550 \text{ nm})$ measured at $\text{RH} < 50\%$.

Both the scattering and the absorption coefficients were similar ($\sigma_{sp} = 60 \text{ Mm}^{-1}$; $\sigma_{ap} = 21 \text{ Mm}^{-1}$) to those measured at an urban-coastal site, Toulon (France), during 2005-2006 [Saha *et al.*, 2008]. The average scattering coefficient obtained in this study was larger than those obtained in the Eastern Mediterranean by Vrekoussis *et al.* [2005] ($50 \pm 23 \text{ Mm}^{-1}$ in Finokalia, Greece, and $45 \pm 22 \text{ Mm}^{-1}$ in Erdemli, Turkey). Pereira *et al.* [2011] obtained in Évora (Portugal) a mean value of $\sigma_{sp}(550 \text{ nm}) = 43 \text{ Mm}^{-1}$, which was also

considerably lower than the value obtained in the present study. It can be explained since Évora is a non-polluted small city and Erdemli and Finokalia are remote coastal sites with their highest σ_{sp} values linked to the presence of dust aerosols. A large $\sigma_{sp}(550 \text{ nm})$ of 75 Mm^{-1} [Andreae *et al.*, 2002] was measured at a remote site in the Negev desert of Israel affected by moderately polluted continental air masses.

Table 5-2: Summary of aerosol optical properties (mean value, standard deviation, median, maximum and minimum values and 25 and 75 percentiles).

Parameter	Mean±SD	Median	Min.	Max.	P25	P75
$\sigma_{sp}(550 \text{ nm}) (\text{Mm}^{-1})$	61 ± 25	55	25	128	43	74
$\sigma_{ap}(550 \text{ nm}) (\text{Mm}^{-1})$	24 ± 9	23	11	50	16	28
$\omega_0(550 \text{ nm})$	0.71 ± 0.07	0.71	0.54	0.85	0.66	0.76
SAE(450-700)	1.6 ± 0.3	1.7	0.6	2.2	1.4	1.9

The scattering coefficient showed a clear seasonal pattern. Large values were found in winter, with a mean value of $70\pm30 \text{ Mm}^{-1}$, and low one in summer ($53\pm24 \text{ Mm}^{-1}$). The same pattern was found for the absorption coefficient, with a mean value of $30\pm11 \text{ Mm}^{-1}$ during winter, whilst during summer the absorption coefficient presented a mean value of $18\pm4 \text{ Mm}^{-1}$. Also in winter, the standard deviations were larger than in summer, which could be related to the large day-to-day variability of the atmospheric conditions in winter. During this season, stable anticyclonic conditions that favour accumulation of particles near-surface alternate with the influence of Atlantic air masses that clean the air by advection and/or wet deposition processes. Similar seasonal variations of aerosol scattering and absorption coefficients at our site were also reported by Lyamani *et al.* [2010] from December 2005 to November 2007. These authors attributed this seasonality to seasonal changes in meteorological conditions and emissions.

The scattering Ångström exponent, $SAE(450-700)$, ranged from 0.6 to 2.2 with an average value of 1.6 ± 0.3 . During the study period, this parameter presented values larger than 1.3 in most cases, denoting a predominance of fine particles. The Ångström exponent exhibited large values in winter. This fact indicates an increase in the contribution of fine particles during the cold season related with the increase of the anthropogenic activity (domestic heating). As shown in Figure 5-3 there is a significant negative correlation ($R = -0.73$) between scattering Ångström exponent, $SAE(450-700)$, and PM_{10}/PM_1 ratio. In other words, $SAE(450-700)$ decreases when the contribution of fine particles to the total mass load decreases. A similar relationship between Ångström exponents (column and surface) and the ratio of accumulation mode volume concentration to total volume concentration was reported by *Hand et al.* [2004]. Significant negative correlations have been also observed between Ångström exponent and the ratio of nmC in PM_{10} / nmC in PM_1 during winter ($R = -0.63$) and between Ångström exponent and the ratio of mineral matter in PM_{10} / mineral matter in PM_1 during summer ($R = -0.69$).

The single scattering albedo represents a key parameter in the assessment of the direct effect of atmospheric aerosol particles in the radiative energy budget in terms of their cooling or warming effects. To determine ω_0 at 550 nm we have calculated σ_{ap} at 550 nm using the absorption coefficient at 637 nm measured with MAAP and Ångström exponent value of 1 that is considered appropriate for an urban atmosphere where black carbon (mainly emitted by vehicles) is the main light absorber [*Kirchstetter et al.*, 2004]. This parameter had a mean value at 550 nm of 0.71 ± 0.07 . It presented larger values in spring and summer than in autumn and winter, with a mean value for spring-summer of 0.73 ± 0.06 and for autumn-winter of 0.65 ± 0.06 . These results suggest a large contribution of absorbing particles in the study site, which are in

accordance with the chemical composition since the contribution of organic matter and elemental carbon, OM+EC, (containing absorbing particles) to PM₁ increased from 37.5% in summer to 54.4% in winter (Figure 5-1). As we mentioned before, the use of domestic heating in conjunction with a lower development of the convective mixing layer could favour the accumulation of carbonaceous particles near surface.

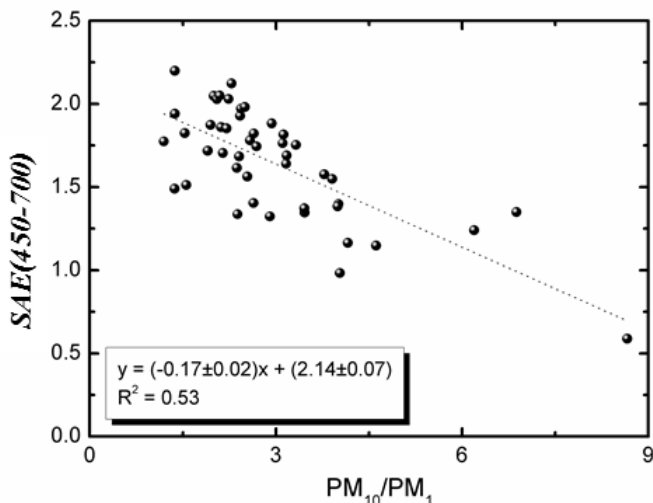


Figure 5-3: Scattering Ångström exponent calculated between 450-700 nm versus PM₁₀/PM₁ ratio.

5.3 Mass scattering and absorption efficiencies

5.3.1 Measurement Method

We have applied the measurement method to calculate the mass scattering and absorption efficiencies (α_{sp} ; α_{ap}) of the aerosol particles as the ratio between the scattering and the absorption coefficients, respectively, and PM₁₀ mass concentration. Since the nephelometer and MAAP do not have size cut-off, we used this method with the PM₁₀ mass concentration. The filters were weighted at RH of 50% and the RH within the nephelometer was also below 50%. The RH correction for the mass scattering efficiency requires knowledge of the

$f(\text{RH})$ curves used to “dry out” the scattering efficiency. Regarding the absorption efficiency is known that the effect of the RH on the absorption coefficient is not significant [Nessler *et al.*, 2005]. Thus, due to the measurement conditions ($\text{RH} \leq 50\%$) we do not consider that corrections are necessary.

During the period of study, α_{sp} was in the range $0.6\text{-}3.2 \text{ m}^2\text{g}^{-1}$, with a mean value of $1.5 \pm 0.5 \text{ m}^2\text{g}^{-1}$, which was almost three times the value of α_{ap} ($0.6 \pm 0.2 \text{ m}^2\text{g}^{-1}$). The mean α_{sp} obtained in this study was slightly lower than the average value ($1.7 \pm 1.1 \text{ m}^2\text{g}^{-1}$) reported by *Hand and Malm* [2007] for urban regions. A significantly higher value of $2.6 \pm 0.8 \text{ m}^2\text{g}^{-1}$ was estimated at Hyttiälä, Finland [Virkkula *et al.*, 2011], for PM₁₀ particles at dry conditions (RH within the nephelometer of $32 \pm 11\%$). *Jung et al.* [2009] obtained at Beijing, for relatively clean conditions, a scattering efficiency for PM₁₀ particles of $1.4 \pm 0.9 \text{ m}^2\text{g}^{-1}$, while for relatively polluted conditions these authors obtained α_{sp} of $3.1 \pm 0.9 \text{ m}^2\text{g}^{-1}$.

The seasonal variability of the PM₁₀ mass scattering and absorption efficiencies is shown in Table 5-3. Both of them exhibited larger values in winter ($\alpha_{sp} = 2.0 \pm 0.5 \text{ m}^2\text{g}^{-1}$ and $\alpha_{ap} = 0.9 \pm 0.1 \text{ m}^2\text{g}^{-1}$) than in summer ($\alpha_{sp} = 1.2 \pm 0.4 \text{ m}^2\text{g}^{-1}$ and $\alpha_{ap} = 0.4 \pm 0.1 \text{ m}^2\text{g}^{-1}$). Similar seasonality in the mass scattering efficiency was obtained in northern China, by *Yan* [2007]. Although the PM₁₀ mass concentration was larger in spring and summer, mainly due to the increase in mineral matter levels, these particles are less efficient in terms of scattering and absorbing radiation, than the aerosol particles that predominate in winter. Thus, mass scattering and absorption efficiencies seasonal patterns are closely related to differences in PM composition. During summer, dust aerosols (mainly coarse grain size) increase their contribution to the PM₁₀ fraction whilst during winter time, OM+EC particles are the major contributors.

Table 5-3 Seasonal and annual mean values of the PM₁₀ mass scattering and absorption efficiencies for the period from March 2006 to February 2007.

PM ₁₀ mass efficiencies	Spring	Summer	Autumn	Winter	Annual
α_{sp} (550 nm) (m ² g ⁻¹)	1.5±0.4	1.2±0.4	1.3±0.3	2.0±0.5	1.5±0.5
α_{ap} (550 nm) (m ² g ⁻¹)	0.5±0.2	0.4±0.1	0.7±0.2	0.9±0.1	0.6±0.2

5.3.2 Scattering and absorption efficiencies for coarse and fine particles applying MLR method

The importance of separating between sub- and super-micron particles is clear because these particles have very distinct sources, optical properties, chemical composition and atmospheric lifetime. To derive α_{sp} and α_{ap} of coarse and fine aerosols we have used the following formulas:

$$\sigma_{sp} = \alpha_{sp,C} \cdot [PM_{10-1}] + \alpha_{sp,F} \cdot [PM_1] + I_s \quad \text{Eq. 5.1}$$

$$\sigma_{ap} = \alpha_{ap,C} \cdot [PM_{10-1}] + \alpha_{ap,F} \cdot [PM_1] + I_a \quad \text{Eq. 5.2}$$

where σ_{sp} (σ_{ap}) is the aerosol scattering (absorption) coefficient (Mm⁻¹), $\alpha_{sp,C}$ and $\alpha_{sp,F}$ ($\alpha_{ap,C}$ and $\alpha_{ap,F}$) are the mass scattering (absorption) efficiencies of coarse and fine particles, $[PM_{10-1}]$ and $[PM_1]$ are the coarse and fine particulate mass concentrations (μg/m³), and I_s (I_a) is a constant representing contributions to scattering (absorption) not related to either coarse or fine aerosols (interception with the y-axis). The intercept was computed in the regressions; however it is not considered further because it tended to be close to zero and it has no radiative significance.

The coarse and fine mass scattering efficiencies calculated were 0.5±0.2 m²g⁻¹ and 2.5±0.4 m²g⁻¹ (correlation coefficient, $R = 0.76$), respectively, and the mass absorption efficiency for coarse and fine particles were 0.1±0.1 m²g⁻¹ and 0.8±0.2 m²g⁻¹ ($R = 0.62$), respectively. So, aerosol particles in the fine mode present higher mass scattering and absorption efficiencies compared to those in the coarse mode denoting that smaller particles extinct light more efficiently at

visible wavelengths. The mass scattering efficiencies obtained in this work were comparable to the values obtained by *White et al.* [1994] in Southwest USA ($2.4\text{-}2.5 \text{ m}^2\text{g}^{-1}$ for fine particles and $0.3\text{-}0.4 \text{ m}^2\text{g}^{-1}$ for coarse particles). Very similar values of α_{sp} ($2.5\pm0.6 \text{ m}^2\text{g}^{-1}$ and $0.6\pm0.2 \text{ m}^2\text{g}^{-1}$ for fine and coarse particles, respectively) were also reported by *Chow et al.* [2002] in Tucson (AZ, USA). Furthermore, the α_{sp} obtained in our study were in accordance with the average value proposed by *Hand and Malm* [2007] ($\alpha_{sp,F} = 2.3\pm0.8 \text{ m}^2\text{g}^{-1}$; $\alpha_{sp,C} = 0.6\pm0.3 \text{ m}^2\text{g}^{-1}$) for urban sites.

Several authors [*Vrekoussis et al.*, 2005; *Bryant et al.*, 2006; *Pandolfi et al.*, 2011] estimated the mass scattering efficiency of fine particles with the measurement method considering that the scattering process was mainly due to particles in the fine mode. Their results were slightly larger than the α_{sp} obtained in this work and in other studies that also applied the MLR method, suggesting that the measurement method can overestimate the mass scattering efficiencies derived. To obtain fine mass efficiencies with the measurement method, the total scattering is divided by the PM_1 mass concentration. With this approach, it is necessary to assume that particles in the coarse mode do not contribute to the scattering coefficient. This assumption led to an overestimation just because the total scattering coefficient is attributed to a fraction of the total mass concentration and not to the total mass concentration. It is important to highlight that, although fine particles are more efficient in terms of extinction of radiation, it is also necessary to quantify the effect of coarse particles.

5.3.3 Scattering and absorption efficiencies for chemical species applying MLR Method

To separate the effects of the different chemical components in the scattering process we have applied different regression models. The MLR analysis has been performed with the total scattering coefficient as the independent variable and the sulphate ion, nitrate, mineral matter, OM+EC and the residual fraction mass concentrations as the dependent ones. To account for the total scattering coefficient the species in the PM₁₀ fraction has been used in this analysis. It is remarkable that due to differences in the sampling and analysis methods the obtained efficiencies in different studies are not always directly comparable. For example, differences in the methods used to obtain the chemical composition, in the size cut or in the RH (sampling below 50% or at ambient RH) can contribute to differences in the mass efficiencies obtained. Our estimate of $\alpha_{sp}(\text{SO}_4^{2-}\text{nm}) = 7 \pm 1 \text{ m}^2\text{g}^{-1}$ was in the upper end of the range of values given by *Charlson et al.* [1999]. A similar value of $7 \pm 2 \text{ m}^2\text{g}^{-1}$ was reported for fine sulphate ion by *Formenti et al.* [2001] at the Negev Desert applying the MLR method. *Vrekoussis et al.* [2005] deduced the mass scattering efficiency for sulphate ion from the slope of the total scattering coefficient versus the SO₄²⁻nm mass concentration. They obtained an annual mean value of $5.9 \pm 1.7 \text{ m}^2\text{g}^{-1}$ at Erdemli and $5.7 \pm 1.4 \text{ m}^2\text{g}^{-1}$ at Finokalia. *Pandolfi et al.* [2011] obtained a mean $\alpha_{sp}(\text{SO}_4^{2-}\text{nm})$ of $15.6 \text{ m}^2\text{g}^{-1}$ with the measurement method. The mass scattering efficiency obtained for NO₃⁻ ($5 \pm 2 \text{ m}^2\text{g}^{-1}$) was also in the upper end of the range of values reported in the literature.

The PM₁₀ mineral matter mass scattering efficiency obtained in this study ($0.2 \pm 0.3 \text{ m}^2\text{g}^{-1}$) was in the lower end of the range of values reported by *Vrekoussis et al.* [2005] in the Eastern Mediterranean ($1 \text{ m}^2\text{g}^{-1}$ at Finokalia and $0.2 \text{ m}^2\text{g}^{-1}$ at Erdemli) with the measurement method during dust events. With

this same approach, *Pereira et al.* [2008] obtained in Portugal a value of $1.0 \pm 0.1 \text{ m}^2\text{g}^{-1}$, which was considerably higher than the $\alpha_{sp}(\text{mineral})$ obtained in Granada. A value of $0.9 \text{ m}^2\text{g}^{-1}$ was estimated for dust aerosols transported from the Sahara desert to Portugal by *Wagner et al.* [2009]. Furthermore, our value was also lower than the values obtained with the MLR method (ranging from 0.5 to $3.1 \text{ m}^2\text{g}^{-1}$) by *Hand and Malm* [2007]. It is necessary to remark that the studies we have compared with have been performed during important dust events and that in most cases the use of the measurement method can lead to an overestimation of the α_{sp} calculated. When computing the mineral mass scattering efficiency with the measurement method [*Vrekoussis et al.*, 2005; *Pereira et al.*, 2008; *Wagner et al.*, 2009] the total scattering coefficient is attributed to the mineral mass concentration and, therefore, assuming that other species contribute marginally to the total scattering.

Several authors [*Cheng et al.*, 2008; *Andreae et al.*, 2008] have reported the importance of EC particles in the absorption process, whilst organic matter (OM) contributes to both, the scattering and the absorption processes. The OM+EC (in PM_{10}) mass scattering efficiency obtained was $2.8 \pm 0.4 \text{ m}^2\text{g}^{-1}$. Here, the OM+EC concentration was calculated as explained in Section 3.5 assuming a carbon multiplier of 1.4. For direct comparison with other studies, we have normalized this value to a carbon multiplier of 1.8. Thus, we obtained a mass scattering efficiency for OM+EC particles of $2.2 \text{ m}^2\text{g}^{-1}$. This value was in the range $1.8 - 4.2 \text{ m}^2\text{g}^{-1}$ calculated by *Hand and Malm* [2007] for OM particles. *Quinn et al.* [2002] found scattering efficiency for OM of $1.4 \text{ m}^2\text{g}^{-1}$ at the Indian Ocean applying the MLR method. Our value was closed to that estimated by *Malm and Hand* [2007] for fine ($< 2.5 \mu\text{m}$) OM particles in Phoenix ($2.47 \text{ m}^2\text{g}^{-1}$) at RH of 0%. These results suggest that EC particles do

not contribute significantly to both the scattering coefficient and the total mass load.

In order to validate the mass scattering efficiencies obtained with the MLR model, we have used an extra dataset (9 days from April to June 2007) not included in the previous calculation. The scattering coefficient calculated multiplying the mass scattering efficiencies and the corresponding mass concentrations showed a significant correlation ($R = 0.94$) with the scattering coefficient measured with the nephelometer and a slope close to unity. Thus, the total scattering coefficient can be derived from PM_{10} speciation using the mass scattering efficiencies obtained in this study.

Finally, the MLR method was used to determine the mass absorption efficiencies of the different chemical species as we did to determine the mass scattering efficiencies previously. However, no satisfactory results were found. The nmC was the only species that correlates well with the absorption coefficient, so a simple linear fit has been used in this case (measurement method). Figure 5-4 shows the absorption coefficient at 550 nm versus nmC mass concentration in PM_{10} and the corresponding linear fit. These variables exhibit a good correlation ($R = 0.94$) denoting that carbonaceous matter dominate the absorption process. The nmC absorption efficiency was $1.9 \pm 0.1 \text{ m}^2\text{g}^{-1}$, considerably lower than the values found in the literature for EC particles [*Bond and Bergstrom, 2005; Cheng et al., 2008; Andreae et al., 2008; Pandolfi et al., 2011; Querol et al., 2013*]. This significant difference could be due to the low contribution of OC particles to the absorption process, although these particles contribute significantly to the total nmC mass load.

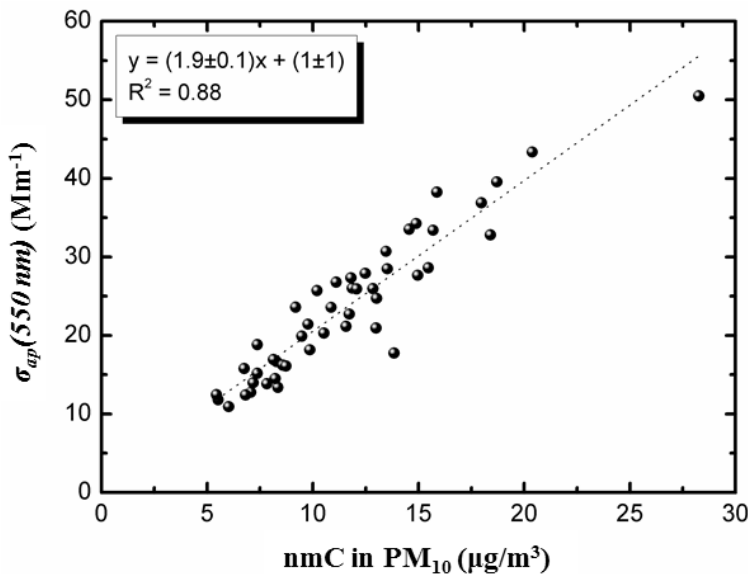


Figure 5-4: Absorption coefficient at 550 nm versus nmC mass concentration in the PM_{10} fraction and the corresponding linear fit.

5.4 Conclusions

From one year of measurements (from March 2006 to February 2007) performed at an urban site in Southern Spain (Granada), we have estimated different aerosol optical properties, mass concentration and chemical composition. The scattering and absorption coefficients were measured with no aerosol cut-off, and chemical speciation was obtained for PM_{10} and PM_1 . Among all the aerosol constituents, mineral matter was the major constituent in the PM_{10-1} fraction while OM+EC particles contributed the most to the PM_1 fraction. Larger PM_{10} concentrations were obtained during summer linked to the increase in the mineral matter levels. On the other hand, the fine mass concentration exhibited large values during spring and winter when the anthropogenic activity is the dominant source. The total scattering and absorption coefficients presented a mean value of $61 \pm 25 \text{ Mm}^{-1}$ and $24 \pm 9 \text{ Mm}^{-1}$, respectively, showing larger values in winter and lower in summer. Urban

aerosols present very low values of single scattering albedo (the mean single scattering albedo at 550 nm in Granada was 0.71 ± 0.07), denoting that these aerosol particles contain a large fraction of absorbing material. In this sense, urban aerosols could produce a positive radiative forcing. Furthermore, single scattering albedo seasonality denotes an absorption enhancement during the cold season that could be related to the increase in the anthropogenic activity (levels of OM+EC particles increased considerably during winter) and the predominance of low mixing layer heights at this time of the year. The scattering Ångström exponent presented a mean value of 1.7 ± 0.3 , suggesting a large fraction of fine particles at this site. Its seasonal variability indicates an increase in the contribution of fine particles during the cold season, an observation confirmed by the $\text{PM}_1/\text{PM}_{10}$ ratio.

The PM_{10} mass scattering efficiency presented a mean value of $1.5 \pm 0.5 \text{ m}^2\text{g}^{-1}$ (typical of urban areas), which was considerably larger than the PM_{10} mass absorption efficiency. The mass scattering and absorption seasonality show a similar trend to PM_1 and opposite to PM_{10-1} . This seasonality is therefore influenced by the variations on PM composition.

To obtain the contribution of fine and coarse particles to the total scattering and absorption coefficients we applied the MLR method. Although we obtained that fine particles extinct light more efficiently than coarse particles, results suggest that it is also necessary to quantify the effect of coarse particles. The mass scattering and absorption efficiencies calculated were in accordance with the results found in the literature. Regarding the chemical composition, the mass scattering efficiency of the different aerosol constituents in the PM_{10} fraction were also calculated applying the MLR method. Among all the species considered, $\text{SO}_4^{2-}\text{nm}$ exhibited the largest mass scattering efficiency ($7 \pm 1 \text{ m}^2\text{g}^{-1}$) and dust aerosols presented the lowest mass scattering efficiency

($0.2 \pm 0.3 \text{ m}^2 \text{g}^{-1}$), a value considerably lower if compared with the literature. The α_{sp} obtained for OM+EC particles was similar to the values reported for OM particles. Finally, we applied the MLR method with the absorption coefficient as the independent variable but no satisfactory results were obtained. Only nmC particles correlated well with the absorption coefficient so α_{abs} were determined with a simple linear fit. This fact suggests that the absorption process was mainly dominated by carbonaceous particles and that other species did not contribute significantly.

It is important to highlight that the MLR technique is useful for computing mass efficiencies and that the data requirements are not very restrictive. However, the method itself could contribute to the large variability obtained. On the other hand, the measurement method is the simplest one but the mass scattering and absorption efficiencies obtained with this technique only represent average conditions for the sampling periods. The mass scattering and absorption efficiencies obtained in this study can be used to estimate the scattering and absorption coefficients and, hence, the radiative effect of the aerosol particles.

6 Aerosol Hygroscopicity

6.1 Study of the relative humidity dependence of aerosol light-scattering at Granada

This section is devoted to the study of the effect of the relative humidity on the aerosol-light scattering coefficient. Aerosol particle optical properties were measured at Granada, Spain, during winter and spring seasons in 2013. Measured optical properties included particle light-absorption coefficient (σ_{ap}) and particle light-scattering coefficient (σ_{sp}) at dry conditions and at high relative humidity. The scattering enhancement due to water uptake was determined by means of a custom built humidifier system, which is described in Section 3.3. This chapter is adapted from “*Study of the relative humidity dependence of aerosol light-scattering in southern Spain*” by G. Titos, H. Lyamani, A. Cazorla, M. Sorribas, I. Foyo-Moreno, A. Wiedensohler and L. Alados-Arboledas. Published in Tellus B, 66, 24536, 2014.

6.1.1 Overview: Winter and spring campaigns

The winter campaign started on 22 January and lasted until 15 February 2013. It was characterized by low ambient temperatures with average campaign values of 9 ± 5 °C and ambient RH of $61\pm21\%$. Both variables presented clear diurnal patterns with high temperature and low RH values at midday. During the spring campaign (4 April - 10 May 2013) the mean ambient temperature was 16 ± 6 °C and the RH was $50\pm20\%$. From 13 to 19 April, the temperature increased considerably, reaching hourly values up to 30°C at midday. After this period, the temperature experienced a strong decrease being the period from 28 to 30 April characterized by very low temperatures (maximum temperature at midday below 10°C). Concerning the chemical composition of aerosol particles in the PM₁₀ size fraction, Figure 6-1 shows the chemical speciation for the winter and spring campaigns. During the winter campaign, elemental carbon (EC)

contributed 9% to the total mass and particulate organic matter (OM, calculated as 1.6*Organic Carbon) contributed around 40%. Mineral matter (calculated as the sum of Al_2O_3 , SiO_2 , CO_3 , Ca, Fe, Mg, K) represented 18% of the PM_{10} mass concentration. This last constituent doubled its contribution to PM_{10} mass concentration during the spring campaign whereas the contribution of OM and EC decreased to 24 and 6%, respectively. The contribution of SO_4^{2-} was slightly higher during the spring campaign while in the case of NO_3^- its contribution was higher during the winter campaign. In spite of the limited number of samples, the chemical speciation during the campaigns was in accordance with the results shown in Section 4.2 for the period 2006-2010 in Granada.

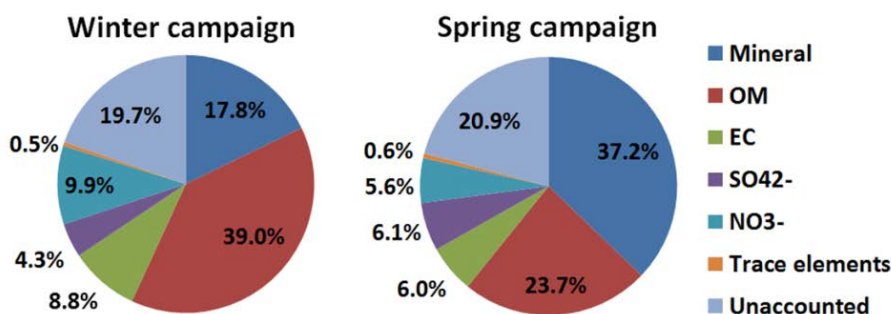


Figure 6-1: Chemical speciation of PM_{10} fraction during winter and spring campaigns expressed in percentage (%). The unaccounted mass fraction refers to the percentage of mass that was not determined by chemical analysis compared to the gravimetric PM_{10} mass. Mineral fraction was calculated as the sum of Al_2O_3 , SiO_2 , CO_3 , Ca, Fe, Mg, K, trace elements as the sum of Li, P, Sc, Ti, V, Cr, Mn, Co, Ni, Cu, Zn, Ga, Ge, As, Se, Rb, Sr, Cd, Sn, Sb, Cs, Ba, La, Ce, Lu, Hf, Ta, W, Tl, Pb, Bi, Th and U) and OM as $\text{OC} \times 1.6$.

In the winter campaign, the RH inside the reference nephelometer was on average $17 \pm 5\%$ and during the spring campaign it was $30 \pm 7\%$. These low RH values were attained with no need of drying. For those periods when both nephelometers measured at dry conditions ($\text{RH} < 50\%$), they showed a good agreement with each other in the measured scattering coefficients. In particular, the particle light scattering coefficient at 550 nm at dry conditions ($< 50\% \text{ RH}$) in the humidified nephelometer was around 8% ($R^2 = 0.99$) and 3% ($R^2 = 0.97$)

smaller than the measured in the reference nephelometer during the winter and spring campaigns respectively. Similar results were obtained for the other wavelengths. This difference could be related with sampling losses in the humidifier system and it was empirically corrected by applying the slopes of the regression between the reference and the humidified nephelometers when measuring at RH<50% as correction factors.

Figure 6-2a and Figure 6-3a show an overview of the measured dry particle light scattering and absorption coefficients, σ_{sp} (dry, 550 nm) and σ_{ap} (dry, 637 nm), during the winter and spring campaigns at Granada, respectively. The data shown represent hourly averaged data. Unfortunately, there are no data of the particle light absorption coefficient for around half of the winter campaign (since 8 February), because the instrument was shipped for the ACTRIS intercomparison workshop. Table 6-1 summarizes the mean (\pm SD) and median values of measured and derived variables for the two measurement periods.

Table 6-1: Statistical summary of the aerosol dry scattering and absorption coefficients, single scattering albedo, scattering Ångström exponent and scattering enhancement factor at 85% RH during the winter and spring campaigns.

	Winter Campaign		Spring Campaign	
	Mean \pm SD	Median	Mean \pm SD	Median
σ_{sp} (dry, 550 nm) (Mm $^{-1}$)	40 \pm 30	29	38 \pm 26	31
σ_{ap} (637 nm) (Mm $^{-1}$)	17 \pm 17	10	11 \pm 11	8
SAE(dry, 450-700)	1.8 \pm 0.4	1.9	1.8 \pm 0.3	1.8
ω_0 (637 nm)	0.70 \pm 0.09	0.70	0.73 \pm 0.11	0.75
f (RH=85%, 550 nm)	1.5 \pm 0.2	1.5	1.6 \pm 0.3	1.6

During the winter campaign, the hourly σ_{sp} (dry, 550 nm) ranged from 3 to 187 Mm $^{-1}$ and from 2 to 338 Mm $^{-1}$ during the spring campaign. The hourly σ_{ap} (dry, 637 nm) varied within the winter measurement period from 0.6 and 84 Mm $^{-1}$ with an average value of 17 \pm 17 Mm $^{-1}$. During the spring campaign, the

values of the σ_{ap} (dry, 637 nm) were slightly lower (average $11\pm11 \text{ Mm}^{-1}$), showing a strong day to day variability during both measurement periods. Intensive aerosol particle variables such as the single scattering albedo, ω_0 , and scattering Ångström exponent, SAE , were used to better understand the variability of the enhancement factor of the particle light scattering. On average, the differences between both campaigns when looking at ω_0 (dry, 637 nm) and SAE (dry, 450-700) were very small (Figure 6-2b and Figure 6-3b). According to the ω_0 (dry, 637 nm) values reported in Table 6-1, absorbing aerosol particles presented a significant contribution to the aerosol population over Granada in both campaigns. The scattering processes were dominated by fine particles (SAE (dry, 450-700) = 1.8), in agreement with previous studies performed at our station [Lyamani *et al.*, 2008; Lyamani *et al.*, 2010].

Figure 6-2c and Figure 6-3c show the temporal evolution of $f(\text{RH}=85\%, \lambda)$ for the winter and spring campaigns respectively. During most of the study period the RH of the humidified nephelometer was set to a constant value of 85% RH and for some time periods of 2-3 hours of duration the humidity was cycled from low to high RH. It is interesting to note that the actual RH measured inside the humidified nephelometer can differ in $\pm 10\%$ from the set point value of RH = 85% due to the thermal gradient between the outlet of the humidifier and the nephelometer chamber. Fierz-Schmidhauser *et al.* [2010a] encountered a similar issue in their humidified nephelometer. In our system, although the relative humidity downstream of the humidifier was almost constant in time, the RH inside the humidified nephelometer was not. In order to avoid a masked effect in the $f(\text{RH})$ due to RH fluctuations inside the humidified nephelometer, the $f(\text{RH})$ measured at RH values between 75-95% has been recalculated to the target value of RH = 85% using Eq. 6.1 that is based on Eq. 2.9 and assuming that it generally holds.

$$f(RH)_{target} = f(RH)_{measured} \left(\frac{1 - RH_{target}}{1 - RH_{measured}} \right)^{-\gamma} \quad \text{Eq. 6.1}$$

Mean campaign values of the fitting parameter γ calculated from the humidograms measured in the winter and spring campaigns (see section 6.1.3) were used for the calculation of $f(RH=85\%)$ in Eq. 6.1. For the winter and spring campaigns, the mean γ values were 0.27 and 0.40 respectively. The use of a mean γ in Eq. 6.1 contributes to the uncertainty in the reported $f(RH=85\%)$ values. However, since only $f(RH)$ values measured between 75 and 95% RH were recalculated to 85% RH small differences are expected. For example, if the measured $f(RH=75\%) = 1.5$ and $\gamma = 0.40$, a change of $\pm 20\%$ in the γ value when recalculating $f(RH)$ to 85% RH would cause an average difference of 4% in $f(RH=85\%)$, which is not very substantial. Hereafter, $f(RH)$ will refer to the 550 nm wavelength. The average $f(RH=85\%)$ values for both campaigns were very similar (1.5 ± 0.2 for winter and 1.6 ± 0.3 for spring campaigns). During the winter campaign, daily averaged values of $f(RH=85\%)$ ranged from 1.35 to 1.70 while during the spring campaign $f(RH=85\%)$ varied from 1.30 to 2. The average values reported in this study are in the range of values reported in the literature for urban and continental aerosols (see Table 6-2). Considerably higher values of $f(RH)$ have been measured in the Arctic [Zieger *et al.*, 2010] and in the free troposphere [Fierz-Schmidhauser *et al.*, 2010b].

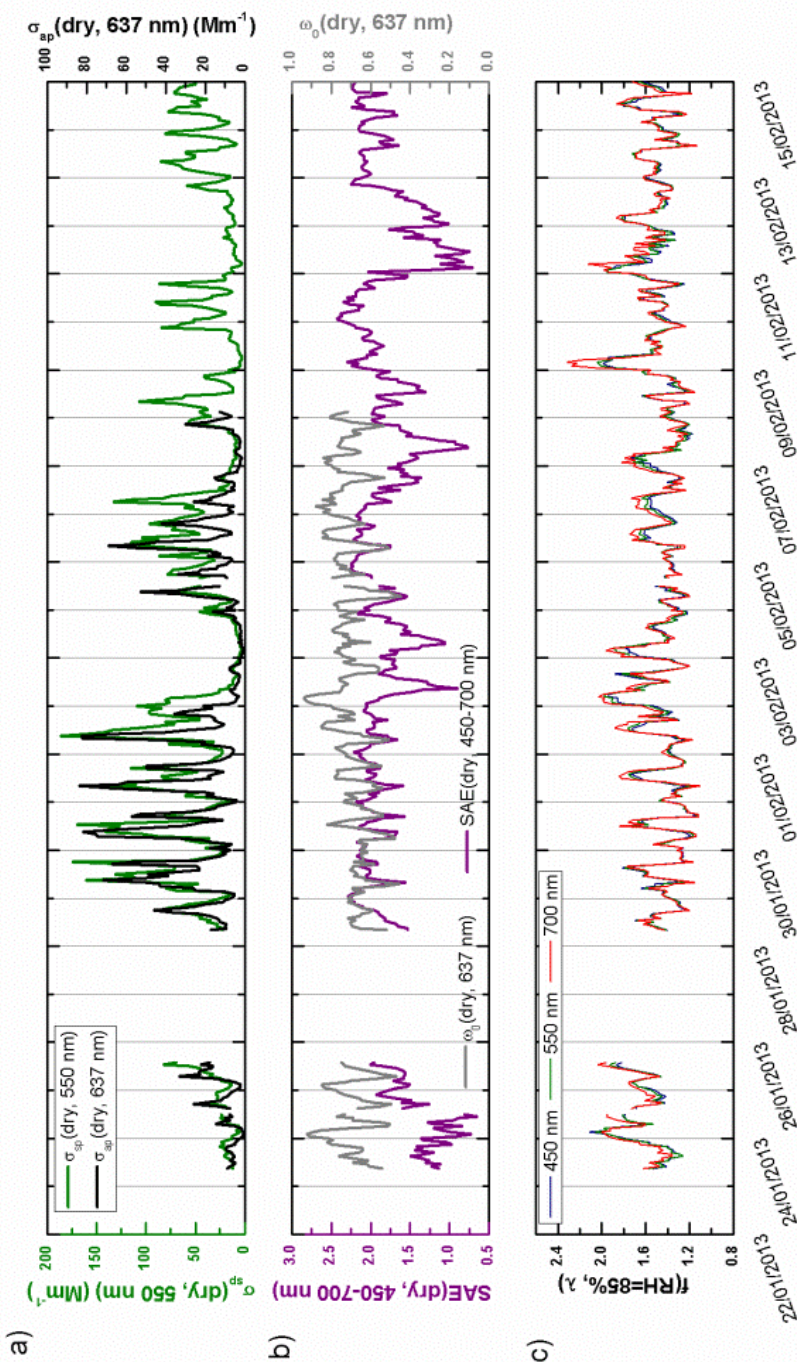


Figure 6-2: Time series of hourly average values of the scattering and absorption coefficients, single scattering albedo, scattering Ångström exponent and $f(\text{RH}=85\%)$ during the winter campaign.

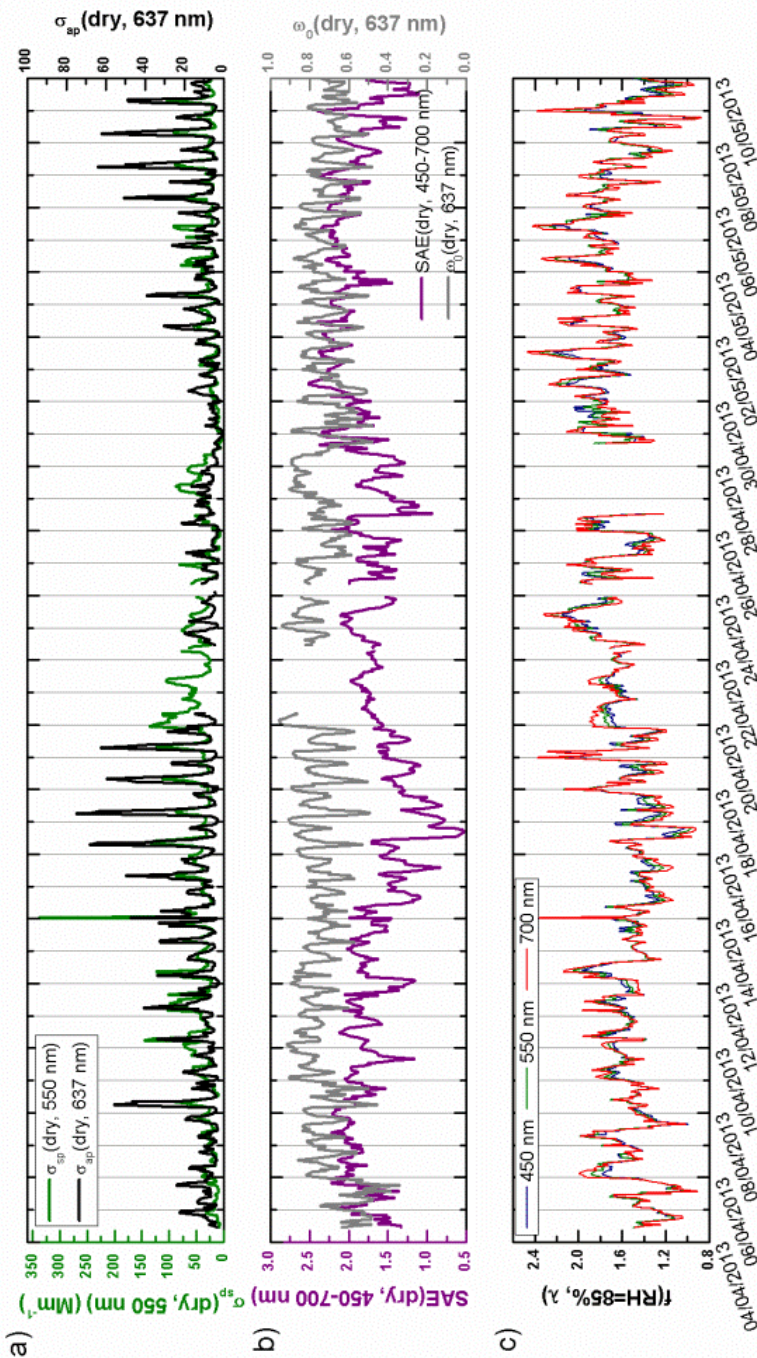


Figure 6-3: Time series of hourly average values of the scattering and absorption coefficients, single scattering albedo, scattering Ångström exponent and $f(\text{RH}=85\%)$ during the spring campaign.

Table 6-2: Hygroscopic growth factors from the literature measured for different aerosol types. The values of $f(RH)$ corresponds to the ratio of the aerosol light scattering coefficients (near 550 nm wavelength) at high RH and at dry conditions (RH<40%).

Observation site	Predominant aerosol type	$f(RH)$	Reference
Mace Head (Ireland)	clean marine	$f(RH=85\%)=2.2$	<i>Fierz-Schmidhauser et al. [2010c]</i>
Cabauw (The Netherlands)	maritime	$f(RH=85\%)=3$	<i>Zieger et al. [2011]</i>
Ny-Ålesund (Norway)	Artic	$f(RH=85\%)=3.5$	<i>Zieger et al. [2010]</i>
Southern Great Plains (OK, USA)	continental	$f(RH=85\%)=1.83$	<i>Sheridan et al. [2001]</i>
Bondville (IL, USA)	continental	$f(RH=82.5\%)=1.4-1.5$	<i>Koloutsou-Vakakis et al. [2001]</i>
Xin'An (China)	dust dominated	$f(RH=80\%)=1.2$	<i>Pan et al. [2009]</i>
Jungfraujoch (Switzerland)	dust dominated	$f(RH=85\%)=1.3$	<i>Fierz-Schmidhauser et al. [2010b]</i>
Southern Great Plains (OK, USA)	dust dominated	$f(RH=85\%)=1.59$	<i>Sheridan et al. [2001]</i>
Granada (Spain)	dust dominated	$f(RH=85\%)=1.3$	<i>This study</i>
Beijing (China)	urban	$f(RH=80-85\%)=1.26$	<i>Yan et al. [2009]</i>
Xin'An (China)	urban pollution	$f(RH=80\%)=1.57$	<i>Pan et al. [2009]</i>
Granada (Spain)	urban	$f(RH=85\%)=1.6$	<i>This study</i>

A Saharan dust event (SDE) of moderate intensity occurred during the spring campaign (14-19 April according to the backward trajectories ending in Granada at 500 m a.g.l.). This period was characterized by a strong decrease in the dry scattering Ångström exponent (see Figure 6-3b), which reached its minimum during 16 April, with a daily mean value close to 0.5, denoting an increase in the contribution of coarse mode aerosols. In coincidence with this decrease, the dry single scattering albedo at 637 nm increased to values up to 0.9. The $f(RH=85\%)$ also decreased during this period to values close to 1 denoting that dust particles have low hygroscopic enhancement. The $f(RH=85\%)$ daily mean value on 16 April was 1.3 ± 0.2 , which is in accordance with the values reported by *Pan et al.* [2009] of 1.2 at 80% RH during a dust episode near Beijing and by *Fierz-Schmidhauser et al.* [2010b] for dust aerosols in the free troposphere ($f(RH=85\%) = 1.3$).

6.1.2 Diurnal cycles

All the variables analyzed here had clear diurnal patterns (Figure 6-4) mainly governed by changes in local sources, especially road traffic emissions, and the meteorological conditions. *Lyamani et al.* [2010] performed a detailed analysis of the seasonal diurnal evolutions of σ_{sp} (dry, 550 nm), σ_{ap} (dry, 637 nm), SAE(dry, 450-700) and ω_0 (dry, 637 nm) in Granada during the period 2005-2007. The diurnal patterns observed in this study are in agreement with the previously reported by *Lyamani et al.* [2010]. Here, these diurnal cycles are used to support the interpretation of the diurnal cycle of the scattering enhancement factor.

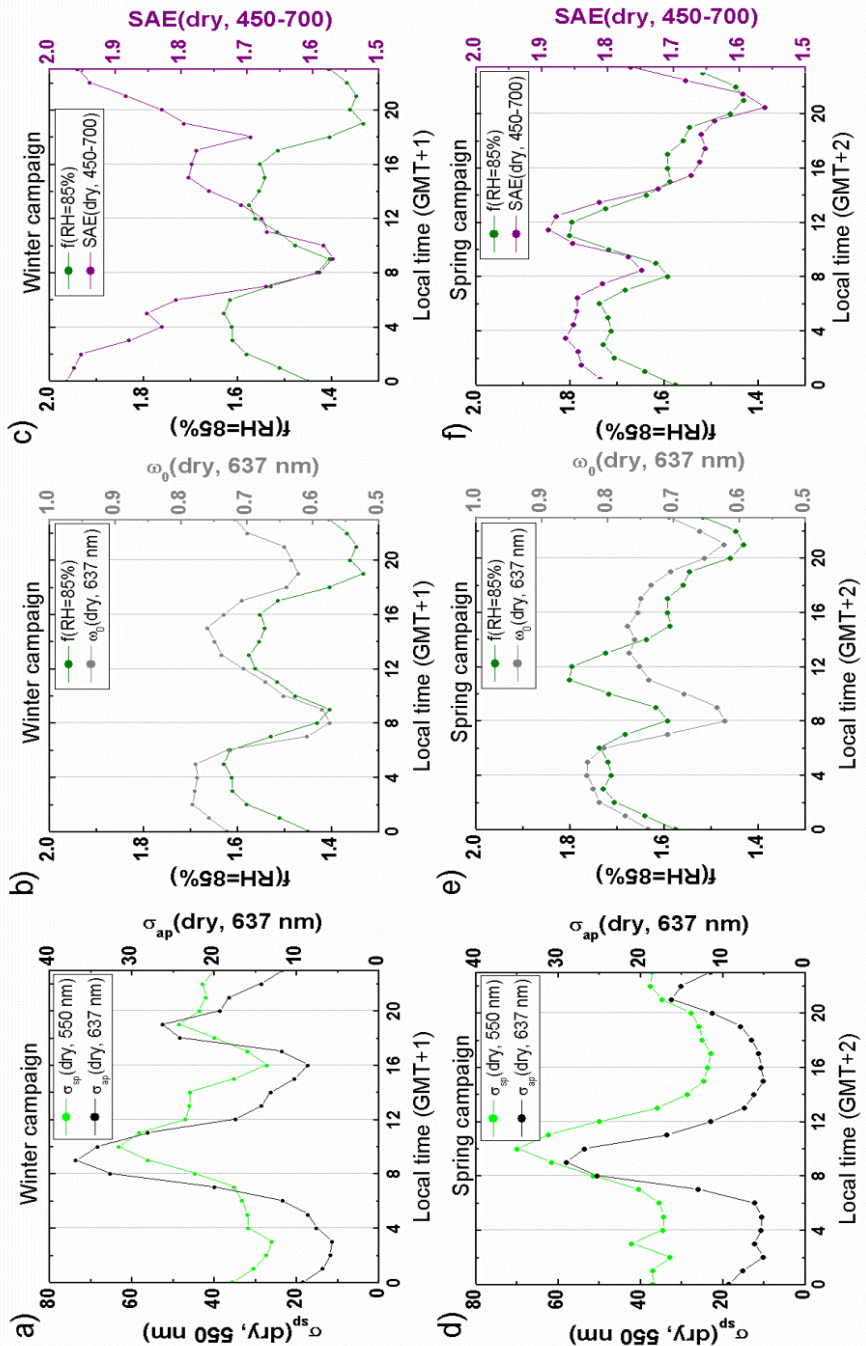


Figure 6-4: Diurnal evolution of the scattering coefficient at 550 nm, absorption coefficient at 637 nm, scattering enhancement factor at 85% RH and 550 nm, single scattering albedo at 637 nm and scattering Ångström exponent during the winter (upper panel) and spring (lower panel) campaigns.

During both campaigns, $f(\text{RH}=85\%)$ showed two minima during the morning and afternoon traffic rush hours. The two $f(\text{RH}=85\%)$ minima were probably connected to the relative increase of the non-hygroscopic particle fraction such as black carbon and road dust due to traffic emissions as indicated by a decrease in $\text{SAE}(\text{dry}, 450-700)$ and $\omega_0(\text{dry}, 637 \text{ nm})$ during the traffic rush hours. During the winter campaign, the diurnal cycle displayed by $f(\text{RH}=85\%)$ was very similar to the one presented by the single scattering albedo (Figure 6-4b). On the other hand, during the spring campaign, $f(\text{RH}=85\%)$ showed similar diurnal variation as $\text{SAE}(\text{dry}, 450-700)$. Thus, the diurnal behavior of $f(\text{RH}=85\%)$ seems to be driven by both the chemical composition and the size of the dry particles (related here with the single scattering albedo and the scattering Ångström exponent due to the lack of online chemical measurements). In Section 6.1.4 the relationship between $f(\text{RH}=85\%)$ and $\text{SAE}(\text{dry}, 450-700)$ and $\omega_0(\text{dry}, 637 \text{ nm})$ is analyzed in more detail.

6.1.3 Humidograms

During some time periods in both campaigns, the RH was scanned from low to high values (up to 90-95%). The RH measurement cycle started with a zero measurement and the RH was increased stepwise up to 90-95% in the humidified nephelometer within 30 min, and then decreased back to RH values around 40% or below during the second half of the hour. To perform these RH-cycles temporal windows in which the aerosol particle properties are thought to not change drastically (as usually occurred between the morning and evening traffic rush hours) were selected in order to avoid a strong effect of local traffic and easily characterize $f(\text{RH})$ changes connected with changes in the air masses affecting our site. Figure 6-5 shows the humidograms measured during the winter (a) and spring (b) campaigns. The data shown represent average values

in 2% RH size bins and the date and local time of each humidogram are shown in the legend.

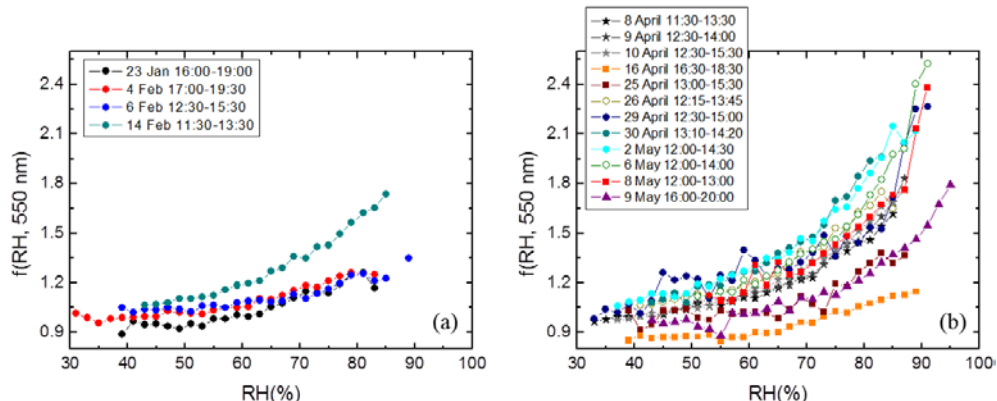


Figure 6-5: Aerosol light-scattering enhancement factor versus RH during different time periods in the winter (a) and spring (b) campaigns. Each point represents the average $f(\text{RH})$ value in 2% RH size bins.

No deliquescence behavior was observed during the study period, and in all the cases the $f(\text{RH})$ increased monotonically with RH. 5-days air mass back-trajectories arriving at Granada at 500 m a.g.l. were computed online (<http://ready.arl.noaa.gov/>) using HYSPLIT4 model to support the interpretation of the humidograms. Table 6-3 shows the mean and standard deviation of the particle light scattering and absorption coefficients, single scattering albedo, scattering Ångström exponent, $f(\text{RH}=85\%)$, and the air mass classification at 500 m a.g.l. for each scan period. As can be observed, SAE(dry, 450-700) and ω_0 (dry, 637 nm) values showed low variability within each scan (as indicated by the standard deviation) which suggests no significant changes in the aerosol composition and type during the scan.

Table 6-3: Mean and standard deviation of the dry scattering and absorption coefficients at 550 and 637 nm, respectively, single scattering albedo at 637 nm, scattering Ångström exponent for 450-700 nm, scattering enhancement factor at 85% RH and air mass classification during the humidograms (Med. Refers to Mediterranean air masses)

Day	σ_{sp} (Mm ⁻¹)	σ_{ap} (Mm ⁻¹)	$\omega_0(637 \text{ nm})$	SAE(450-700)	$f(\text{RH}=85\%)$	Air mass
23 Jan	17±4	6±2	0.69±0.05	1.3±0.2	1.17	Atlantic
4 Feb	48±16	14±10	0.73±0.08	2.0±0.1	1.25	Atlantic
6 Feb	25±8	6±2	0.76±0.03	1.8±0.2	1.23	Atlantic
14 Feb	61±10	--	--	2.2±0.1	1.74	Atlantic
8 Apr	34±12	11±5	0.71±0.04	2.0±0.1	1.62	N. Europe + Atlantic
9 Apr	39±8	5±1	0.85±0.02	1.8±0.1	1.69	Atlantic
10 Apr	57±9	7±2	0.86±0.03	2.1±0.1	1.69	Atlantic
16 Apr	31±1	4.8±0.8	0.86±0.02	0.6±0.1	1.12	N. Africa + Med.
25 Apr	10±3	4±1	0.66±0.05	1.6±0.3	1.32	Med.
26 Apr	50±11	13±2	0.74±0.03	2.0±0.1	1.65	Med.
29 Apr	9±3	4±2	0.61±0.07	1.9±0.4	1.71	Atlantic
30 Apr	25±3	10±2	0.64±0.03	2.4±0.1	1.96	Atlantic
2 May	37±9	5±2	0.83±0.05	2.3±0.1	2.15	Atlantic
6 May	35±16	10±4	0.73±0.03	2.0±0.2	1.98	Med.
8 May	38±13	14±6	0.69±0.03	1.8±0.2	1.73	Med. + Regional
9 May	24±4	10±6	0.7±0.1	1.3±0.2	1.37	Atlantic + Regional

During the winter campaign all the humidograms were very similar in shape and magnitude with the exception of 14 February that presented a higher scattering enhancement. On 23 January, 4 and 6 February the humidograms showed very little enhancement with values of $f(\text{RH}=85\%)$ below 1.25. However, on 14 February, $f(\text{RH})$ reached values up to 1.74 at 85% relative humidity. During this particular scan, $SAE(\text{dry}, 450-700)$ was larger (see Table 6-3), which suggest a predominance of fine and more hygroscopic aerosol particles. These differences between scans can be connected with different air masses arriving at the sampling location (and thus different aerosol type). During all the winter scans, the air masses arriving at 500 m a.g.l. at Granada were coming from the Atlantic Ocean and crossed Spain in their way to Granada. However, during 14 February the air masses were advected at very low levels, close to the ground, likely picking up pollutants, leading to an increase in the particle light scattering coefficient and $SAE(\text{dry}, 450-700)$. During the spring campaign most humidograms presented a similar shape and magnitude with the exception of those obtained on 16 and 25 April and 9 May (Figure 6-5b). The lowest scattering enhancement of the spring campaign was observed on 16 April. On this day, Granada was affected by air masses from the Sahara Desert. For this case, the average ($\pm SD$) $\omega_0(\text{dry}, 637 \text{ nm})$ was 0.86 ± 0.02 and the scattering Ångström exponent was 0.6 ± 0.1 , indicating a predominance of coarse particles. The enhancement of the particle light scattering coefficient with RH for this day was very small, with an average $f(\text{RH}=85\%)$ of 1.12. Furthermore, sampling losses in the humidifier system during this day were higher since there were $f(\text{RH})$ values below 1 at low RH. The shape and magnitude of the scattering enhancement observed under SDE conditions in this study was very similar to that reported by *Fierz-Schmidhauser et al.* [2010b] for dust aerosols ($f(\text{RH}=85\%)=1.3$). On 25 April, the air mass affecting Granada at

500 m a.g.l. was coming from the Mediterranean basin. The single scattering albedo observed was very low with an average value of 0.66 ± 0.05 at 637 nm. The high relative contribution of absorbing particles may explain the observed low hygroscopic enhancement of $f(\text{RH}=85\%)=1.32$ during 25 April scan. During 9 May, the air mass arriving at Granada at 500 m a.g.l. came from the Atlantic Ocean and was advected at very low levels and low speed, suggesting stagnant conditions, which led to an $\text{SAE}(\text{dry}, 450-700)$ value of 1.3 ± 0.2 , $\omega_0(\text{dry}, 637\text{nm})=0.7 \pm 0.1$ and $f(\text{RH}=85\%)$ value of 1.37. Higher scattering enhancements were observed on the rest of scans where fine particles predominated ($\text{SAE}(\text{dry}, 450-700)$ values around 2). The air masses at 500 m a.g.l. arrived from the North Atlantic Ocean (on 8, 9, 10, 29 and 30 April and 2 May) and the Mediterranean Sea (on 26 April and 6-8 May). In all these cases, the air masses were travelling at very low levels in their way to Granada, likely picking up pollutants. These results connect with those obtained for the winter campaign where air masses travelling at low levels experienced a higher scattering enhancement as occurred on 14 February.

6.1.4 Relationship between $f(\text{RH})$ and other measured variables

Figure 6-6 shows the frequency distribution of 1 minute $f(\text{RH}=85\%)$ values for the winter and spring campaigns. The $f(\text{RH}=85\%)$ frequency distributions presented different shape in each campaign. In the winter campaign, the most frequent values were comprised between 1.3 and 1.5 representing 40% of the data. On the other hand, during the spring campaign, the most frequent values were in the range 1.4-1.8 comprising around 52% of the data. In addition, cases of high scattering enhancement were more frequent during the spring campaign since 27% of the data had a $f(\text{RH}=85\%)>1.8$ while only 8% of the data were above 1.8 during the winter campaign.

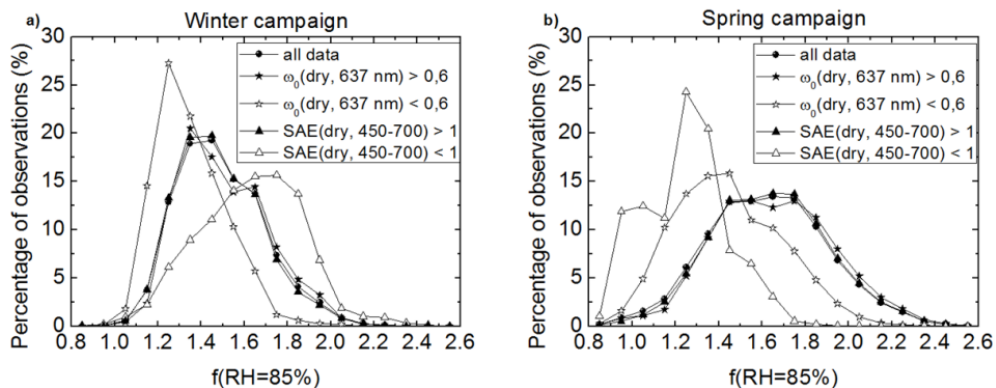


Figure 6-6: Frequency distribution of $f(\text{RH}=85\%)$ at 550 nm during the winter and spring campaigns. Data for periods where $\text{SAE}(\text{dry}, 450-700)$ was above and below 1 and $\omega_0(\text{dry}, 637 \text{ nm})$ was above and below 0.6 were extracted and plotted separately.

Observations of $f(\text{RH})$ when $\text{SAE}(\text{dry}, 450-700)$ was above and below 1 (indicating a significant contribution of small or large particles, respectively) and $\omega_0(\text{dry}, 637 \text{ nm})$ was above and below 0.6 (less or more absorbing aerosol particles, respectively), were extracted from the data set and plotted as frequency distributions in Figure 6-6. For both campaigns, the $f(\text{RH}=85\%)$ frequency distributions for $\omega_0(\text{dry}, 637 \text{ nm}) < 0.6$ were shifted towards lower $f(\text{RH}=85\%)$ values in comparison with those corresponding to $\omega_0(\text{dry}, 637 \text{ nm}) > 0.6$. This means that aerosols containing a larger fraction of absorbing particles were less hygroscopic. During the spring campaign, the $f(\text{RH}=85\%)$ frequency distribution for $\text{SAE}(\text{dry}, 450-700) < 1$ was shifted towards lower $f(\text{RH}=85\%)$ values. This suggests that the aerosol containing a higher proportion of large particles was less hygroscopic than the one containing a higher proportion of small particles ($\text{SAE}(\text{dry}, 450-700) > 1$) (Figure 6-6b). This behavior is connected with the large contribution of dust particles with low hygroscopicity [Fierz-Schmidhauser *et al.*, 2010b; Sheridan *et al.*, 2001] to the coarse mode during the spring campaign. As shown in Figure 6-1, mineral dust, which commonly occurs in the coarse fraction [Song *et al.*, 2012], contributed

around 37% to the total PM₁₀ mass concentration. During the winter campaign, the behavior observed was the opposite; the frequency distribution of $f(\text{RH}=85\%)$ for $\text{SAE}(\text{dry}, 450-700) < 1$ was shifted towards higher $f(\text{RH}=85\%)$ values (Figure 6-6a). This different behavior between seasons can be connected with differences in the chemical composition. During winter time, when fine particles predominated ($\text{SAE}(\text{dry}, 450-700) > 1$) the fine mode was mainly composed by non-hygroscopic material such as EC and OC that is thought to suppress or reduce hygroscopic growth [Carrico *et al.*, 2005], resulting in a lower hygroscopic enhancement for cases of $\text{SAE}(\text{dry}, 450-700) > 1$ than for cases of $\text{SAE}(\text{dry}, 450-700) < 1$.

In order to better understand the relationship between $f(\text{RH}=85\%)$ and other aerosol particle variables, a cross-correlation of the main in-situ aerosol particle variables and $f(\text{RH}=85\%)$ was performed. The scattering enhancement factor showed no correlation with the extensive parameters $\sigma_{sp}(\text{dry}, 550 \text{ nm})$, $\sigma_{bsp}(\text{dry}, 550 \text{ nm})$ and $\sigma_{ap}(\text{dry}, 637 \text{ nm})$. It was moderately correlated with $\omega_0(\text{dry}, 637 \text{ nm})$ showing a $R^2 = 0.3$ and 0.2 during the winter and spring campaigns, respectively. The backscatter fraction (b , ratio of the backscatter and the total scattering coefficients) was negatively correlated with $f(\text{RH}=85\%)$ during the winter campaign ($R^2 = 0.2$), but no correlation was found during the spring campaign. During the winter campaign, $f(\text{RH}=85\%)$ showed no correlation with $\text{SAE}(\text{dry}, 450-700)$ although during the spring campaign it showed a moderate correlation with $R^2 = 0.4$. The different correlations obtained for winter and spring campaigns again suggest differences in the chemical composition of the coarse and fine modes between campaigns and make very difficult to find a single equation that might be used to estimate the scattering enhancement using other optical variables at our site.

Concerning the chemical composition of aerosol particles, some authors have observed a relationship between the scattering enhancement and the chemical composition with special focus in the organic and inorganic content. In particular, *Quinn et al.* [2005] proposed a parameterization to predict $f(\text{RH})$ based on the fraction of particulate organic matter (POM) and *Garland et al.* [2007] showed that the $f(\text{RH}=80\%)$ varied linearly with the organic/inorganic content. In order to explore the relationship between $f(\text{RH})$ and the relative amount of OM and SO_4^{2-} mass concentrations, Figure 6-7 shows $f(\text{RH}=85\%)$ versus the ratio $\text{OM}/(\text{OM}+\text{SO}_4^{2-})$ in the PM_{10} fraction. For this analysis, $f(\text{RH}=85\%)$ values have been averaged over the sampling interval of the filters (24 hours starting at 7 GMT). A substantial decreasing trend of $f(\text{RH})$ for increasing OM mass fraction was found with $R^2 = 0.74$ (excluding the sample collected during the SDE).

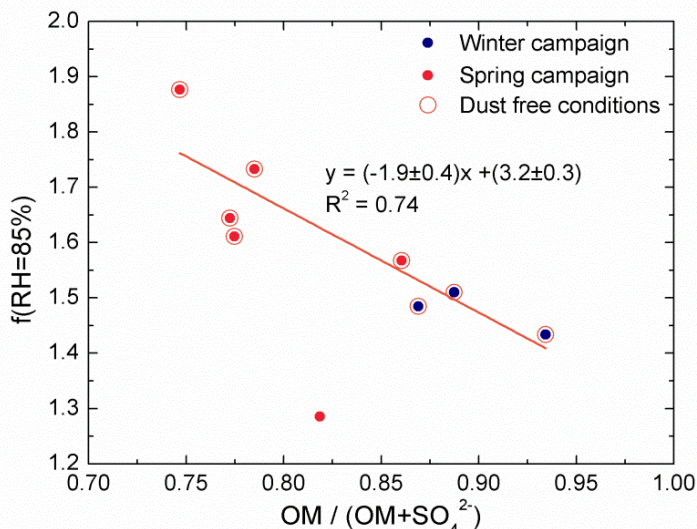


Figure 6-7: Scattering enhancement factor at 85% relative humidity versus the ratio $\text{OM}/(\text{OM}+\text{SO}_4^{2-})$ for the winter and spring campaigns. The linear fit refers to dust free conditions.

In spite of the limited number of samples, it seems that there is a significant relationship between the relative content of OM and the magnitude

of $f(\text{RH})$. In this sense, based on three measurement campaigns performed in India, Asia and the Northeast United States, *Quinn et al.* [2005] found out that aged aerosol particles presented a higher hygroscopicity and lower OM contribution than fresh aerosols connected with the degree of oxidation. A recent publication by *Zieger et al.* [2014] showed that the magnitude of $f(\text{RH})$ was clearly correlated with the inorganic mass fraction and pointed out that the chemical composition is the main factor determining the magnitude of the scattering enhancement. In this sense, an effort should be done in order to better constrain the factors affecting $f(\text{RH})$ at different environments.

6.1.5 Implication for climatic relevant variables

Since the particle light scattering coefficient changes with RH other derived variables such as the single scattering albedo or the backscatter fraction are also expected to change, being also the aerosol radiative forcing dependent on RH. Thus, to quantify the direct effect of aerosol particles in the energy budget it is necessary to transform the dry measurements to ambient conditions. To see the differences between ambient and dry aerosol properties, Figure 6-8 shows the ambient relative humidity (a), the single scattering albedo (b), the backscatter fraction (c) and the aerosol forcing efficiency (d) at ambient conditions, at RH=85% and at the reference RH for the spring campaign. The aerosol forcing efficiency, defined as the aerosol forcing per unit aerosol optical depth [*Sheridan and Ogren, 1999*], was calculated as follows [*Haywood and Shine, 1995*]:

$$\Delta F / \delta = -DS_0 T_{at}^2 (1 - A_C) \omega_0 \beta \cdot \left\{ \left(1 - R_s \right)^2 - \left(\frac{2R_s}{\beta} \right) \left[\left(\frac{1}{\omega_0} \right) - 1 \right] \right\} \quad \text{Eq. 6.2}$$

where D is the fractional day length, S_0 is the solar constant, T_{at} is the atmospheric transmission, A_c is the fractional cloud amount, δ is the aerosol optical depth, β is the upscatter fraction and R_s is the surface reflectance. The upscatter fraction is the fraction of light that is scattered into the upward hemisphere relative to the horizon, and hence, depends on the zenith angle and the particle size. In this thesis, β is parameterized as a function of the measured backscatter fraction (b) using the equation proposed by *Wiscombe and Grams [1976]*:

$$\beta = 0.0817 + 1.8495b - 2.9682b^2 \quad \text{Eq. 6.3}$$

Additionally, for the computation of the aerosol forcing efficiency, constant values of $D = 0.5$, $S_0 = 1370 \text{ W m}^{-2}$, $T_{at} = 0.76$, $A_c = 0.6$, and $R_s = 0.15$ [*Haywood and Shine, 1995*] have been assumed. This sub-section focuses on the spring campaign due to low data coverage during the winter campaign (no availability of MAAP data from 8 February to the end of the campaign and no ambient RH data from 31 January to the 7 February). The $\omega_0(550 \text{ nm})$ at ambient RH has been calculated assuming that the absorption coefficient does not change with RH [*Nessler et al., 2005*] and the change in the scattering coefficient from dry to ambient RH has been calculated using Eq. 6.1 and the corresponding γ parameter. The ω_0 at 550 nm has been calculated from the measured $\sigma_{ap}(637 \text{ nm})$ and assuming a λ^{-1} dependence. In this section all the variables refer to 550 nm wavelength.

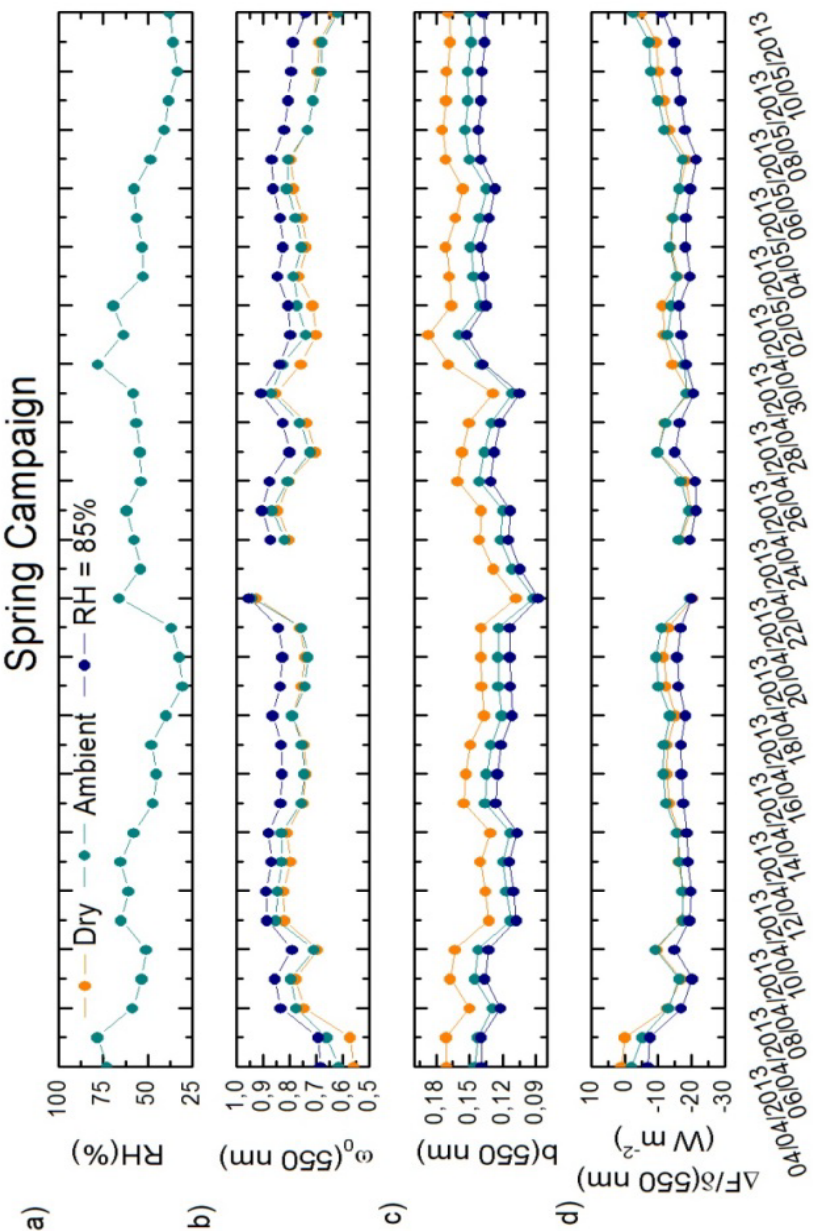


Figure 6-8: Time series of daily a) Ambient relative humidity, b) single scattering albedo at 550 nm, c) backscatter fraction at 550 nm and d) aerosol forcing efficiency at 550 nm at dry, ambient RH and RH = 85% during the spring campaign.

The ambient RH in Granada was very low during the spring campaign, with a daily average campaign value of 53%. Due to this low ambient RH, differences between dry and ambient optical properties were also very low. The single scattering albedo changed from a mean campaign value of 0.75 at dry conditions to 0.77 at ambient conditions. The mean campaign backscatter fraction at dry and at ambient conditions was 0.15 and 0.13, respectively. These small differences led to negligible differences in the calculated aerosol forcing efficiency, which was on average of -13 Wm^{-2} , both at dry and ambient conditions. During time periods characterized by a higher ambient RH, it can be observed that the aerosol forcing efficiency was higher at ambient RH compared to dry conditions. An important fact is that the forcing efficiency can change from positive to negative due to the effect of RH, as occurred on 4 and 5 April. At 85% relative humidity, the effect of water uptake by aerosols is of substantial importance, with an average aerosol forcing efficiency at 85% RH of -17 Wm^{-2} . During the study period, the impact of ambient RH in the aerosol particle optical properties was very small. However, for periods of elevated RH it is necessary to quantify the effect that ambient RH may have in the measured dry aerosol optical properties in order to obtain an appropriate estimation of the radiative forcing by aerosols.

6.1.6 Conclusions

Two measurement campaigns were conducted in Granada during winter and spring seasons to study the aerosol particle scattering enhancement due to water uptake. For the winter and spring campaigns, mean $f(\text{RH}=85\%)$ were 1.5 ± 0.2 and 1.6 ± 0.3 , respectively. Saharan dust event was characterized by a predominance of large particles (low SAE(dry, 450-700) values) with low hygroscopicity. All the variables analyzed presented a diurnal pattern. The two

$f(\text{RH}=85\%)$ minima were connected to the relative increase of the non-hygroscopic fraction (such as black carbon and road dust) due to traffic emissions as indicated by a decrease in $\text{SAE}(\text{dry}, 450\text{--}700)$ and $\omega_0(\text{dry}, 637 \text{ nm})$ during the traffic rush hours. For both campaigns, aerosols containing a larger fraction of absorbing particles were less hygroscopic. However, concerning particles mean size, the behavior in winter and spring campaigns was the opposite: coarse particles were more hygroscopic in the winter than in the spring campaign, which suggests that the chemical composition of the coarse mode during both campaigns was different. In spring, the coarse mode would be probably composed by dust particles that show a low hygroscopicity while during the winter campaign the contribution of mineral matter was much lower, showing a higher hygroscopicity. In spite of the apparent relationship observed between $f(\text{RH}=85\%)$ and $\text{SAE}(\text{dry}, 450\text{--}700)$ and $\omega_0(\text{dry}, 637 \text{ nm})$, these variables showed no substantial correlation with $f(\text{RH}=85\%)$. In terms of the chemical composition, a decreasing trend of $f(\text{RH}=85\%)$ for increasing mass fraction of particulate organic matter was found with a $R^2 = 0.78$. However, due to the limited number of samples, this last result needs to be confirmed with a longer data series. In order to quantify the impact of the relative humidity in the ambient optical properties, measurements taken at low $\text{RH} < 50\%$ were converted to ambient RH using the two-fit parameter equation and the mean γ parameter for each campaign (winter campaign: $\gamma = 0.27$ and spring campaign: $\gamma = 0.40$). Due to the ambient conditions in the experimental site, characterized by low RH values, the effect of the RH on the single scattering albedo, the backscatter fraction and, hence, the radiative forcing efficiency was almost negligible. The radiative forcing efficiency changed from -13 W m^{-2} at dry conditions to -17 W m^{-2} at $\text{RH}=85\%$. Thus, for situations of elevated RH this

Aerosol Hygroscopicity

effect should be taken into account in order to report an accurate estimation of the radiative effect of aerosols.

6.2 Aerosol light-scattering enhancement due to water uptake during the TCAP campaign

The relative humidity effect on the aerosol light-scattering coefficient is approached again in this section. This study was conducted in a marine environment where the atmospheric conditions greatly differ from the ones observed in Granada. The measurements were performed by the DOE/ARM (US Department of Energy Atmospheric Radiation Measurements) Program Mobile Facility during the Two-Column Aerosol Project (TCAP) campaign in Cape Cod, Massachusetts, from summer 2012 to summer 2013. The study site and the instrumentation are carefully described below. The main objective of this chapter is to analyze in detail the aerosol hygroscopic properties with regards to air mass origin and predominant wind sector, and to evaluate possible variables that might be used as proxies to estimate aerosol hygroscopicity. This section is adapted from “*Aerosol light-scattering enhancement due to water uptake during the TCAP campaign*” by G. Titos, A. Jefferson, P. J. Sheridan, E. Andrews, H. Lyamani, L. Alados-Arboledas, and J. A. Ogren. Published in Atmospheric Chemistry and Physics, 14, 7031–7043, 2014.

6.2.1 Site description

The measurements presented in this section were conducted by the DOE/ARM (US Department of Energy Atmospheric Radiation Measurements) Program Mobile Facility [Miller and Slingo, 2007; Mather and Voyles, 2013] during the Two-Column Aerosol Project (TCAP) campaign [Kassianov *et al.*, 2013] deployed at Cape Cod, Massachusetts. Cape Cod is a peninsula jutting out into the Atlantic Ocean in the easternmost portion of the state of Massachusetts, in the northeastern United States. The deployment was located in the northeastern

part of the cape ($41^{\circ}59'36''$ N, $70^{\circ}03'01''$ W, 20 m a.s.l.), inside the Cape Cod National Seashore, and relatively close to large urban agglomerations such as Providence and Boston. Thus, due to its location, the site is subject to both clean and polluted conditions. The campaign started in the summer of 2012 and lasted until the summer of 2013; however, due to problems with the humidifier system, measurements of the hygroscopic enhancement are only available for approximately half of the campaign (from late September to late October 2012 and then from January to mid June 2013).

6.2.2 Instrumentation

Air sampling for all the instrumentation used in this section was obtained from the top of a 10 m high sampling stack of 20.3 cm in diameter. Airflow through this main stack is about 800 lpm. From this flow, 150 lpm flow through a 5.1 cm diameter stainless steel pipe in the center of this larger flow that then is divided into five 30-lpm sample lines. One of these sample lines goes to the Aerosol Observing System (AOS) instruments and the other 4 spare sample lines go out through a blower. A more detailed description of the sampling system can be found in *Jefferson* [2011].

The experimental set-up consists of two integrating nephelometers (TSI, model 3563) operated in series and separated by a humidification system. Since no active drying of the aerosol sample is performed after humidification only the lower branch of the hysteresis curve can be captured with this set-up. The integrating nephelometer (TSI, model 3563) measures aerosol light-scattering (σ_{sp}) and hemispheric backscattering (σ_{bsp}) coefficients at three wavelengths (450, 550 and 700 nm). Instrument zero checks on filtered air were automatically performed hourly. Routine maintenance and instrument calibrations with CO₂ were performed 3 times; once in July, another in January

and again in June. The nephelometers are downstream of a switched impactor system which toggles the aerosol size cut between $1.0\text{ }\mu\text{m}$ (PM_1) and $10\text{ }\mu\text{m}$ (PM_{10}) aerodynamic particle diameters every 30 minutes. The first nephelometer measures the aerosol light-scattering coefficient at dry conditions ($\text{RH}<40\%$) while the second nephelometer measures the aerosol light-scattering coefficient at a controlled RH. The sampled aerosol was gently heated when necessary to achieve a low relative humidity (RH) of 40% or below. The mean \pm standard deviation of the temperature and relative humidity within the dry nephelometer for the whole measurement campaign were $T = 26\pm4\text{ }^{\circ}\text{C}$ and $\text{RH} = 30\pm13\text{ }%$. In order to minimize losses of volatile compounds the temperature of the sampled air was kept below 35°C [Bergin *et al.*, 1997; ten Brink *et al.*, 2000]. Only 0.5% of the 1-min observations occurred at temperatures above this value and these data were not further considered in the study. The humidifier consists of two concentric tubes: the inner one is a high-density porous polytetrafluoroethylene (PTFE) tube and the outer tube is a stainless steel tube wrapped in a tape heater and insulation. A closed loop of water circulates between the PTFE and the outer tube. As the water temperature increases, water vapor moves through the semi-permeable PTFE membrane causing the RH of the sample air to increase. The temperature of the water is regulated via a feedback system between the downstream RH sensor, the PID (proportional-integral-derivative) controller and the heater. Temperature and relative humidity sensors (Vaisala model HMP110, accuracy of $\pm3\text{ }%$ RH) are placed throughout the system: one of the sensors is placed upstream of the impactor box and the other two sensors are placed immediately downstream of the reference and humidified nephelometers. The internal nephelometer TSI RH sensors are not used because of their slower time response and uncertainty. For this reason, the RH inside the nephelometer was calculated from the dew point

temperature of the Vaisala sensor at the outlet of the humidified nephelometer and the internal nephelometer temperature. The instruments reported results at 1-Hz resolution, and the data were then averaged and recorded at 1 min resolution. The nephelometers operated at a volumetric flow rate of 30 lpm. Non-idealities due to truncation errors and the non-Lambertian light source were corrected according to *Anderson and Ogren* [1998]. The uncertainty in the aerosol light-scattering coefficient is about 7% [*Heintzenberg et al.*, 2006]. Every hour the RH measurement cycle started with a zero measurement and then in the humidified nephelometer the RH was increased stepwise to 80–85% within 30 min, and then decreased back to RH values of about 40% or below during the second half of the hour. The upward RH scan corresponded to the PM₁₀ size cut and the downward RH scan to PM₁. When both nephelometers measured at dry conditions (RH<40%) the two of them agreed well (PM₁₀: slope = 1.073 ± 0.001 , intercept = 0.48 ± 0.02 Mm⁻¹ and $R^2 = 0.99$; PM₁: slope = 0.971 ± 0.004 , intercept = 0.68 ± 0.04 Mm⁻¹ and $R^2 = 0.77$ (for the 550 nm wavelength)).

The aerosol light absorption coefficient was measured with a Particle Soot Absorption Photometer (PSAP). The method is based on the integrating plate technique in which the change in optical transmission of a filter caused by particle deposition on the filter is related to the light absorption coefficient of the deposited particles using Beer-Lambert Law. Here, a 3-wavelength version of the PSAP has been used, with nominal wavelengths of 467 nm, 531 nm, and 650 nm. The PSAP data were corrected according to *Bond et al.* [1999] and *Ogren* [2010]. The uncertainty of the PSAP absorption measurement, after application of the transmission and scattering correction, is 20–30% [*Bond et al.*, 1999]. The PSAP is also downstream of the switched impactors.

Ambient temperature, relative humidity, wind speed and direction were continuously monitored using the surface meteorological instrumentation (MET) data from the ARM AMF1 facility.

Air mass back trajectories were computed using the HYSPLIT4 model [Draxler *et al.*, 2013] version 4.9 and were used to support the interpretation of the data.

6.2.3 Methodology

Aerosol intensive properties, such as the single scattering albedo (ω_0), the hemispheric backscatter fraction (b), the submicron scattering fraction (R_{sp}) and scattering Ångström exponent (SAE), were calculated from the aerosol scattering and/or absorption coefficients. In order to determine ω_0 at 550 nm, the absorption coefficient measured with the PSAP was interpolated to the 550 nm wavelength using the Ångström formula (see Section 2.3). In this section, $\omega_0(550 \text{ nm})$, $b(550 \text{ nm})$ and SAE(450-700) refer always to dry conditions and to the PM₁₀ size fraction.

The submicron scattering fraction allows apportionment of light scattering into sub- and super-micrometer aerosol mode. It was calculated for the 550 nm wavelength as follows:

$$R_{sp}(\lambda) = \sigma_{sp(Dp < 1 \mu\text{m})}(\lambda) / \sigma_{sp(Dp < 10 \mu\text{m})}(\lambda) \quad \text{Eq. 6.4}$$

To quantify the effect of water uptake in the aerosol light scattering coefficient, the scattering enhancement factor $f(\text{RH})$ was used. The two-parameter equation (Eq. 2.9) [Clarke *et al.*, 2002; Carrico *et al.*, 2003] was used to describe the increase in aerosol scattering due to hygroscopic growth. To reduce the influence of instrument noise on the calculation, only values of the dry scattering coefficient above 5 Mm⁻¹ were considered in the calculation of $f(\text{RH})$. The constraints imposed for the fitting were a lower RH of 40%, a

minimum span of 30% RH in each scan, a minimum of 50% data coverage in each scan, the RH in the reference nephelometer had to be below 40% and a coefficient of determination (R^2) of the fit above 0.5. These criteria were applied for PM₁₀ and PM₁ size fractions, with each size fraction humidogram fitted separately. A total of 2952 (PM₁₀) and 1753 (PM₁) humidograms were successfully fitted for each size respectively. Additionally, for each scan, $f(RH)$ values were calculated at RH=80% using Eq. 2.9, enabling comparison of scan hygroscopicity.

6.2.4 Overview of the campaign

Mean ambient temperature and relative humidity during the campaign were 7 ± 6 °C and 80 ± 20 %. Both variables presented clear diurnal patterns with higher temperature and lower RH values at midday. The wind speed ranged from calm winds up to values close to 20 m/s during specific periods, showing a mean campaign value of 5 ± 3 m/s. Winds from the west direction occurred more frequently. Figure 6-9 shows an overview of the daily average aerosol light-scattering and absorption coefficients, σ_{sp} (550 nm) and σ_{ap} (531 nm), ω_0 (550 nm) and SAE(450-700) in the PM₁₀ fraction. For the entire campaign, the σ_{sp} (550 nm) had a mean \pm standard deviation values of 22 ± 15 Mm⁻¹ and the corresponding values for σ_{ap} (531 nm) were of 1.1 ± 0.9 Mm⁻¹. In general, the aerosol light absorption coefficient was very low during the measurement period, especially compared with the scattering coefficient; the ω_0 (550 nm) had a mean value of 0.94 ± 0.04 . On the other hand, daily-average ω_0 (550 nm) values ranged from 0.77 to 1.0, denoting periods where the contribution of absorption increased. The campaign-averaged SAE(450-700) was 1.8 ± 0.6 , which is quite high for a coastal environment compared with literature values [e.g., Carrico *et al.*, 1998; Fierz-Schmidhauser *et al.*, 2010b], and is an evidence of the

influence of anthropogenic aerosols at Cape Cod during the TCAP campaign. In fact, the $SAE(450\text{-}700)$ showed a high variability with daily values ranging from 0.6 to 3. The submicron scattering fraction reported similar information with values ranging from 0.02 to 1 indicating different atmospheric conditions dominated by different aerosol types (fine, coarse and mixed particles). Concerning the backscatter fraction, this variable had a mean campaign value of 0.13 ± 0.02 . The $SAE(450\text{-}700)$, $R_{sp}(550 \text{ nm})$ and $b(550 \text{ nm})$ report similar information since all three parameters are related to aerosol mean size [Fan et al., 2010]. In fact, the $SAE(450\text{-}700)$ had a strong correlation with $R_{sp}(550 \text{ nm})$ ($R^2 = 0.81$) and a moderate correlation with $b(550 \text{ nm})$ ($R^2 = 0.5$). For this reason, in the following sections we will focus on the scattering Ångström exponent as indicator of particle size.

None of the variables mentioned above showed a clear diurnal pattern, presenting very small changes throughout the day. In addition, no clear temporal trend was observed throughout the study period, although certain events of elevated $\sigma_{sp}(550 \text{ nm})$ were observed which were connected with high $\omega_0(550 \text{ nm})$ values and low $SAE(450\text{-}700)$ values. These events occurred under high wind speeds and were probably caused by sea salt particles (large particles with minimal absorption). As an example, on 9 March the $\sigma_{sp}(550 \text{ nm})$ reached its maximum value (daily average of 84 Mm^{-1}). On this day the $\omega_0(550 \text{ nm})$ had a mean value of 1 and the $SAE(450\text{-}700)$ was 0.75, suggesting that the aerosol optical properties were dominated by coarse, purely scattering particles.

Figure 6-10 shows the aerosol light scattering enhancement factor $f(\text{RH}=80\%)$ (upper panel) and the γ parameter (lower panel) calculated for the PM_{10} and PM_1 fractions at 550 nm (hereafter the wavelength will be omitted in the notation for simplicity). Over the period of measurement, $f(\text{RH}=80\%)$ had a mean value of 1.9 ± 0.3 , with daily-mean values ranging from 1.4 to 2.6 in the

PM_{10} fraction. In the PM_1 fraction, $f(\text{RH}=80\%)$ had a mean value of 1.8 ± 0.4 and ranged from 1.2 to 3.4.

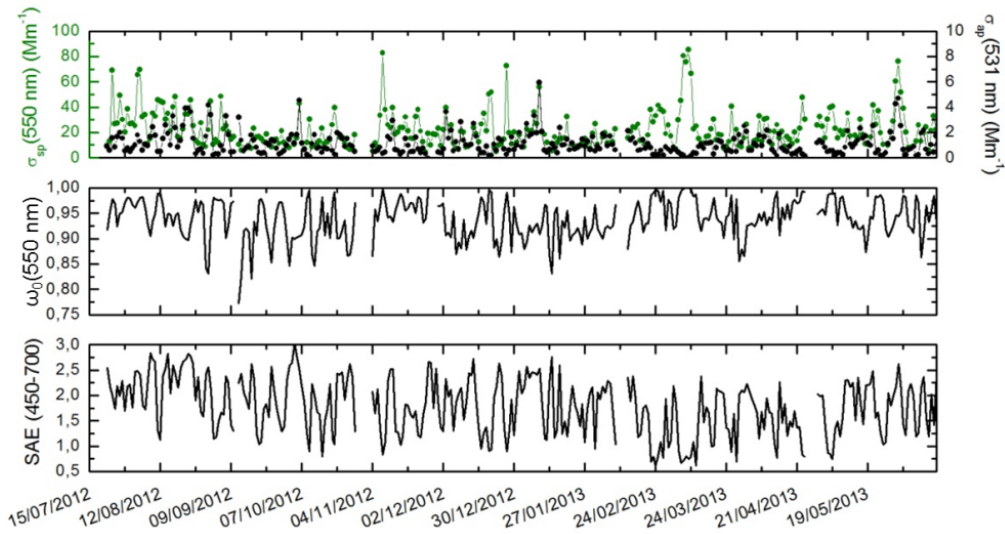


Figure 6-9: Temporal evolution of the daily dry scattering and absorption coefficients (upper panel), the single scattering albedo (middle panel) and the scattering Ångström exponent (lower panel). All the parameters correspond to the PM_{10} fraction. The date is in the format dd/mm/yyyy.

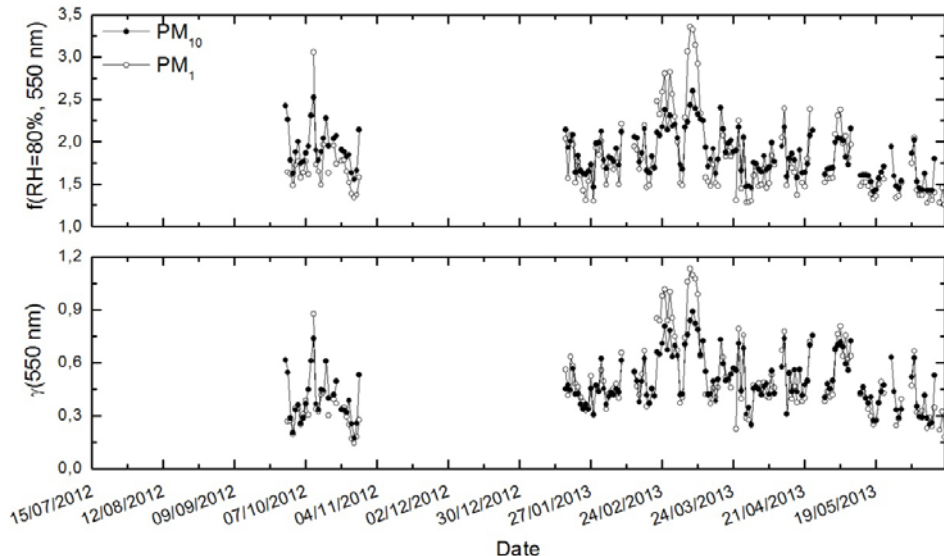


Figure 6-10: Temporal evolution of the daily scattering enhancement factor at 80% relative humidity (upper panel) and the fit parameter γ (lower panel), for PM_{10} and PM_1 fractions. The date is in the format dd/mm/yyyy.

Average γ values were 0.5 for both size fractions but were relatively more variable in the PM₁ fraction (daily γ values ranged from 0.1 to 1.1) than in the PM₁₀ fraction (daily γ values ranged from 0.2 and 0.9). The temporal trend of $f(\text{RH}=80\%)$ and γ was similar in both size fractions, however, larger differences between PM₁₀ and PM₁ were observed for specific events. Specifically, on 9 March this difference was considerably larger with a mean daily $f(\text{RH}=80\%)$ of 3.1 in PM₁ compared to 2.4 in PM₁₀. On this day, the air masses arriving at 500 m a.g.l. at the measurement station were coming from the Atlantic Ocean and traveled at low altitude for the last three days, likely picking up sea salt particles.

In order to investigate in more detail the differences in the magnitude of the scattering enhancement between the fine and coarse fractions, Figure 6-11 shows the hourly $f(\text{RH}=80\%)$ values in PM₁ versus $f(\text{RH}=80\%)$ values in PM₁₀. Data when SAE (at dry conditions and in the PM₁₀ fraction) was below and above 1, denoting a predominance of larger and smaller particles, respectively, were fitted separately. The graph shows that for situation dominated by sea salt aerosols (SAE<1) the scattering in the PM₁ fraction experienced a higher enhancement than in the PM₁₀ fraction. This same behavior was also found for the γ parameter (not shown). This indicates that small sea salt particles have a larger scattering enhancement compared to coarse sea salt particles. This result is supported by theoretical calculations of hygroscopic growth as a function of particle size for common aerosol salts and acids made by Zieger *et al.* [2013]. These authors showed that $f(\text{RH}=85\%)$ increases with decreasing particle size for all components studied, but increases more dramatically for NaCl, the largest component in sea salt. On the other hand, this behavior can be also explained by a shift in the size distribution to a scattering regime with a higher scattering efficiency when the SAE is greater than 1.

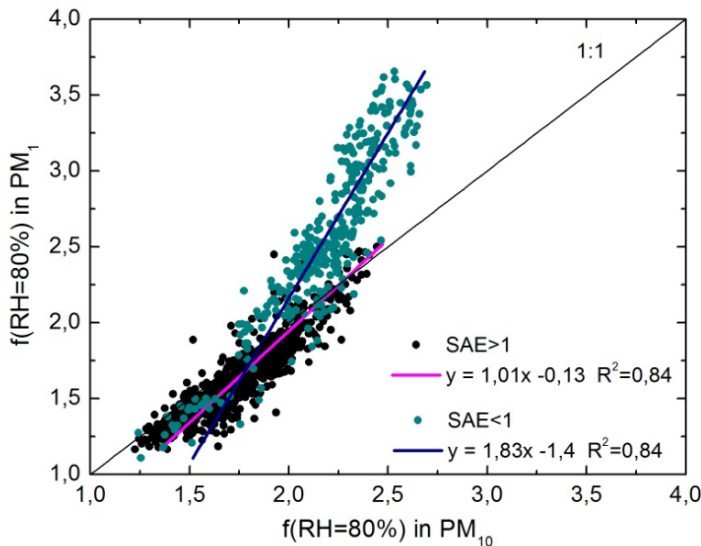


Figure 6-11: Scatter plot of the hourly average scattering enhancement factors at 80% relative humidity in the PM_1 fraction versus the same parameter in the PM_{10} fraction. Data when the scattering Ångström exponent was below and above 1 were fitted separately.

A total of 2952 and 1753 RH scans in PM_{10} and PM_1 fractions, respectively, were fitted according to the criteria explained in Section 6.2.3. Additional fits were performed for the RH ranges below and above 65%. The values of $\gamma_{>65\%}$ and $\gamma_{<65\%}$ were used to identify possible deliquescence transitions. Similar values of $\gamma_{>65\%}$ and $\gamma_{<65\%}$ indicate a monotonic growth for the entire RH range, while distinct values ($\gamma_{<65\%} \ll \gamma_{>65\%}$) indicate no significant enhancement below 65% and a large increase at a RH value above 65%. For those cases in which $\gamma_{<65\%} \ll \gamma_{>65\%}$ the fit using the entire RH range underestimated $f(\text{RH})$ values at both low and high RH and overestimated $f(\text{RH})$ at the transition RH (around 65-75% RH). To illustrate this, Figure 6-12a and Figure 6-12b show the daily average humidogram for two different cases dominated by deliquescent and non-deliquescent particles, respectively. Figure 6-12a shows 9 March daily average humidogram scan ($\gamma = 0.8$, $\gamma_{<65\%} = 0.4$ and $\gamma_{>65\%} = 1.1$) and Figure 6-12b shows the daily average humidogram scan of 31

May ($\gamma = 0.3$, $\gamma_{<65\%} = 0.3$ and $\gamma_{>65\%} = 0.4$). On 9 March the scattering enhancement for $RH > 65\%$ was almost three fold the enhancement for $RH < 65\%$. As mentioned before, during this day there was a predominance of non-absorbing coarse particles (mean $SAE(450-700) = 0.75$ and $\omega_0(550 \text{ nm}) = 1$), suggesting a clear contribution of deliquescent sea salt particles. On the other hand, on 31 May the scattering enhancement was similar for both RH ranges. Slightly darker, non-deliquescent fine mode particles dominated the aerosol on 31 May ($SAE(450-700) = 1.8$, $\omega_0(550 \text{ nm}) = 0.91$) compared with the previous case. Concerning the a parameter (intercept of the $f(RH)$ -RH fitting at $RH=0\%$, see Eq. 2.9), it varies with the aerosol transmission efficiency through the humidifier and goodness of the power law fit. Differences between the experimental and ideal value of a are expected since the a value will depend also on aerosol losses in the dry nephelometer and in the humidifier system. In this study, fitting the whole RH range for deliquescent aerosols seems to be inadequate. Nevertheless, fitting $f(RH)$ to multiple RH ranges offers information on aerosol deliquescence properties.

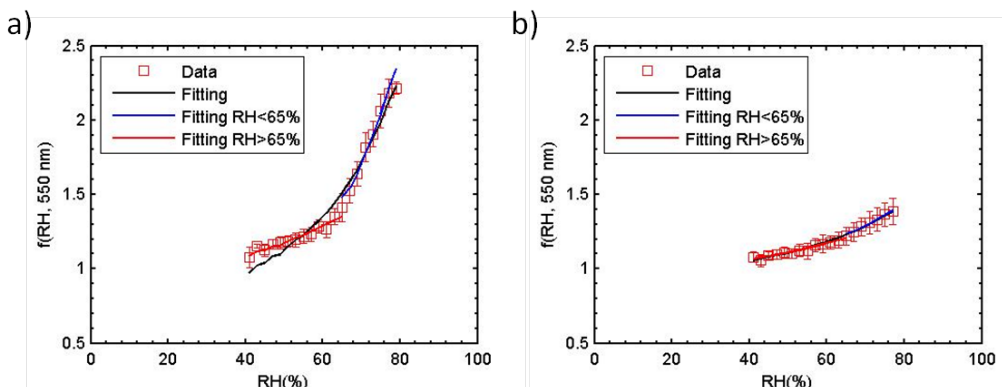


Figure 6-12: Example humidograms of the scattering enhancement factor, given as daily averages where the error bars represent the standard deviation for the 9th of March (a) and the 31st of May (b). The black line denotes the γ fit for the entire RH range ($RH > 40\%$), the blue line denotes the γ fit for $RH > 65\%$ and the red line the γ fit for the $RH < 65\%$.

6.2.5 Influence of wind speed and direction on the aerosol hygroscopicity

In order to evaluate the influence of wind speed and direction on aerosol hygroscopic properties, Figure 6-13 shows bivariate plots of $f(\text{RH}=80\%)$, γ , $\omega_0(550 \text{ nm})$ and $SAE(450-700)$ as a function of wind speed and direction. Both $f(\text{RH}=80\%)$ and γ increased with wind speed. $SAE(450-700)$ and $\omega_0(550 \text{ nm})$ have opposite trends to each other, with increasing $\omega_0(550 \text{ nm})$ values and decreasing $SAE(450-700)$ with wind speed. These plots show that for $225-315^\circ$ sector, the aerosol particles were characterized by lower $\omega_0(550 \text{ nm})$ and higher $SAE(450-700)$, probably due to the influence of anthropogenic air from the populated urban areas of Providence and Boston as can be seen in Figure 6-14. In contrast, for $0-180^\circ$ sector, the aerosol particles over our site were characterized by higher $\omega_0(550 \text{ nm})$ and lower $SAE(450-700)$, probably due to the predominance of marine aerosols from the North Atlantic ocean (Figure 6-14). According to these results, two wind sectors have been considered for further investigation: the marine sector ($0-180^\circ$) and the anthropogenically-influenced sector ($225-315^\circ$). For this analysis, only wind speed values above 5 m/s were considered in order to avoid local influences.

Table 6-4 summarizes the mean and standard deviation of the aerosol optical variables for each sector. There is a clear difference between both wind sectors when looking at the aerosol intensive properties. For anthropogenically-influenced sector, the aerosol particles were characterized by smaller and more absorbing particles with similar $f(\text{RH}=80\%)$ for both size fractions. Furthermore, for the anthropogenically-influenced sector, $\gamma_{>65\%}$ and $\gamma_{<65\%}$ were very similar denoting no distinct deliquescent behavior.

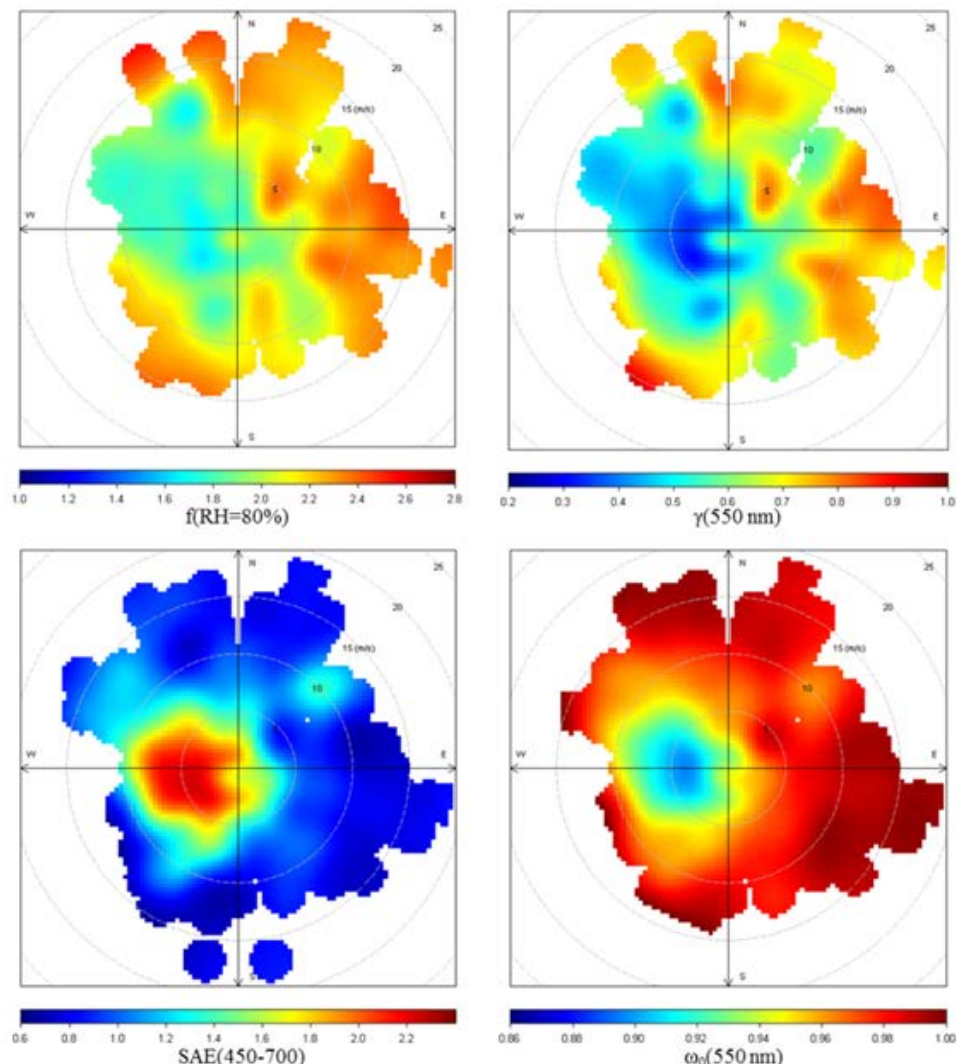


Figure 6-13: Bivariate plots of the scattering enhancement factor at 80% RH, the γ parameter, single scattering albedo and scattering Ångström exponent as a function of wind speed and direction.

The aerosol properties of the marine sector were very different to those of the anthropogenic sector. Larger and very weakly absorbing particles were observed for this sector (see Table 6-4). The $f(\text{RH}=80\%)$ was higher in the PM_1 than PM_{10} fraction, denoting a larger scattering enhancement in the fine mode. In addition, $\gamma_{>65\%}$ was considerably higher (0.9 ± 0.2) than $\gamma_{<65\%}$ (0.4 ± 0.1),

evidence of deliquescent aerosols. Carrico *et al.* [2000] also observed a higher scattering enhancement for clean marine conditions than for polluted situations (see Table 6-5) in Sagres (Portugal) which agrees with the results obtained in this section (Table 6-4) and those shown in Figure 6-11. The $f(RH)$ values reported here for clean and anthropogenically influenced marine aerosols are in agreement with the range of values reported in the literature for marine environments (Table 6-4).

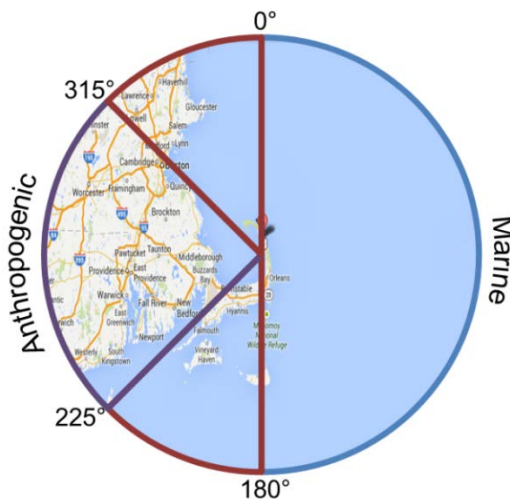


Figure 6-14: Wind sector separation super-imposed on a Google maps image centered in Cape Cod.

Table 6-4: Mean and standard deviation of single scattering albedo, scattering Ångström exponent, γ , $\gamma > 65\%$, $\gamma < 65\%$ and scattering enhancement factor at 80% RH for PM_{10} fraction and scattering enhancement factor at 80% RH for PM_1 fraction for the two wind sectors. All the variables refer to 550 nm except the scattering Ångström exponent that has been calculated between 450 and 700 nm.

Sector	ω_0	SAE	γ	$\gamma_{>65\%}$	$\gamma_{<65\%}$	$f(RH)$ PM_{10}	$f(RH)$ PM_1
Anthro-pogenic	0.93 ± 0.03	1.8 ± 0.5	0.4 ± 0.1	0.5 ± 0.2	0.4 ± 0.1	1.8 ± 0.2	1.7 ± 0.2
Marine	0.98 ± 0.02	0.9 ± 0.3	0.7 ± 0.1	0.9 ± 0.2	0.4 ± 0.1	2.2 ± 0.3	2.5 ± 0.6

Aerosol light-scattering enhancement due to water uptake during the TCAP campaign

Table 6-5: $f(\text{RH})$ values (near 550 nm wavelength) at RH of 85% unless noted (*RH = 82%, **RH=80%) reported in the literature for marine environments. Data correspond to a diameter, D_p , of 10 μm unless noted.

Source	Location	Year	$f(\text{RH})$	Notes
<i>Hegg et al. [1996]</i>	eastern North Pacific Ocean	1994	2.3**	No D_p cut Clean marine
<i>Li-Jones et al. [1998]</i>	Barbados, West Indies	1994	1.8**	Sea salt
<i>Carrico et al. [1998]</i>	Cape Grim, Tasmania	1995	1.98*	Clean marine
<i>McInnes et al. [1998]</i>	Sable Island, Canada	1996	2.7 1.7	$D_p < 1 \mu\text{m}$ Marine Polluted
<i>Kotchenruther et al. [1999]</i>	western North Atlantic Ocean	1996	1.81** 2.30**	$D_p < 4 \mu\text{m}$, "less anthropogenic" "more anthropogenic"
<i>Gassó et al. [2000]</i>	eastern North Atlantic Ocean	1997	2.0** 2.5** 1.69* 1.46*	$D_p < 2.5 \mu\text{m}$ Polluted Clean
<i>Carrico et al. [2000]</i>	Sagres, Portugal	1997	1.86* 1.48*	$D_p < 10 \mu\text{m}$ Clean Polluted $D_p < 1 \mu\text{m}$ Clean Polluted
<i>Sheridan et al. [2002]</i>	Indian Ocean North Central South	1999	1.55 1.69 2.07	$D_p < 1 \mu\text{m}$ Polluted Polluted Clean marine
<i>Carrico et al. [2003]</i>	Asia/Pacific region	2001	2.45* 2.24* 2.95* 2.52*	$D_p < 10 \mu\text{m}$ Marine Polluted $D_p < 1 \mu\text{m}$ Marine Polluted
<i>Fierz-Schmidhauser et al. [2010b]</i>	Mace Head, Ireland	2009	2.2 1.8	Clean Polluted
<i>Zieger et al. [2011]</i>	Cabauw, The Netherlands	2009	3	Maritime
<i>This study</i>	Cape Cod, MA	2012-2013	2.2** 1.8** 2.5** 1.7**	$D_p < 10 \mu\text{m}$ Clean marine Anthropogenic $D_p < 1 \mu\text{m}$ Clean marine Anthropogenic

6.2.6 Air-mass trajectories classification

A cluster analysis of 3-day air mass backtrajectories arriving at Cape Cod at 500 m a.g.l. at 00, 06, 12 and 18 GMT using HYSPLIT4 model [Draxler *et al.*, 2013] version 4.9 was performed to identify the main air masses types affecting the area and their respective aerosol optical properties. This method is based on the geometric distance between individual trajectories and it takes into account speed and direction of the trajectory and height at the arriving location. A total of 1344 backward trajectories were used in the analysis. The number of clusters was selected according to the percent change in total spatial variance (TSV). Large changes in the TSV were interpreted as the merging of significantly different trajectories into the same cluster. According to this criterion, the cluster analysis resulted in five clusters of backtrajectories for air masses arriving at Cape Cod at low level. Figure 6-15 shows the clusters obtained with this analysis and the average humidogram for each cluster. The humidograms represent $f(\text{RH})$ averages in 2% RH size bins and the error bars represent the standard deviation in the PM_{10} fraction. Table 6-6 shows, for each cluster, the mean and standard deviation of the optical parameters.

Table 6-6: Mean and standard deviation of single scattering albedo, scattering Ångström exponent, γ , $\gamma_{>65\%}$, $\gamma_{<65\%}$ and scattering enhancement factor at 80% RH for the five clusters. All the variables refer to PM_{10} unless specifically noted and to 550 nm except the scattering Ångström exponent that has been calculated between 450 and 700 nm.

Cluster	ω_0	SAE	γ	$\gamma_{>65\%}$	$\gamma_{<65\%}$	$f(\text{RH})$ in PM_{10}	$f(\text{RH})$ in PM_1
1	0.94 ± 0.04	1.9 ± 0.7	0.5 ± 0.2	0.6 ± 0.3	0.4 ± 0.1	1.9 ± 0.3	1.8 ± 0.4
2	0.95 ± 0.04	1.8 ± 0.6	0.5 ± 0.1	0.5 ± 0.2	0.4 ± 0.1	1.9 ± 0.3	1.8 ± 0.3
3	0.92 ± 0.04	1.9 ± 0.5	0.4 ± 0.1	0.6 ± 0.2	0.4 ± 0.1	1.7 ± 0.2	1.6 ± 0.3
4	0.92 ± 0.03	2.1 ± 0.5	0.4 ± 0.1	0.5 ± 0.2	0.4 ± 0.1	1.8 ± 0.2	1.7 ± 0.2
5	0.97 ± 0.03	1.1 ± 0.5	0.7 ± 0.2	0.9 ± 0.2	0.4 ± 0.1	2.1 ± 0.3	2.5 ± 0.6

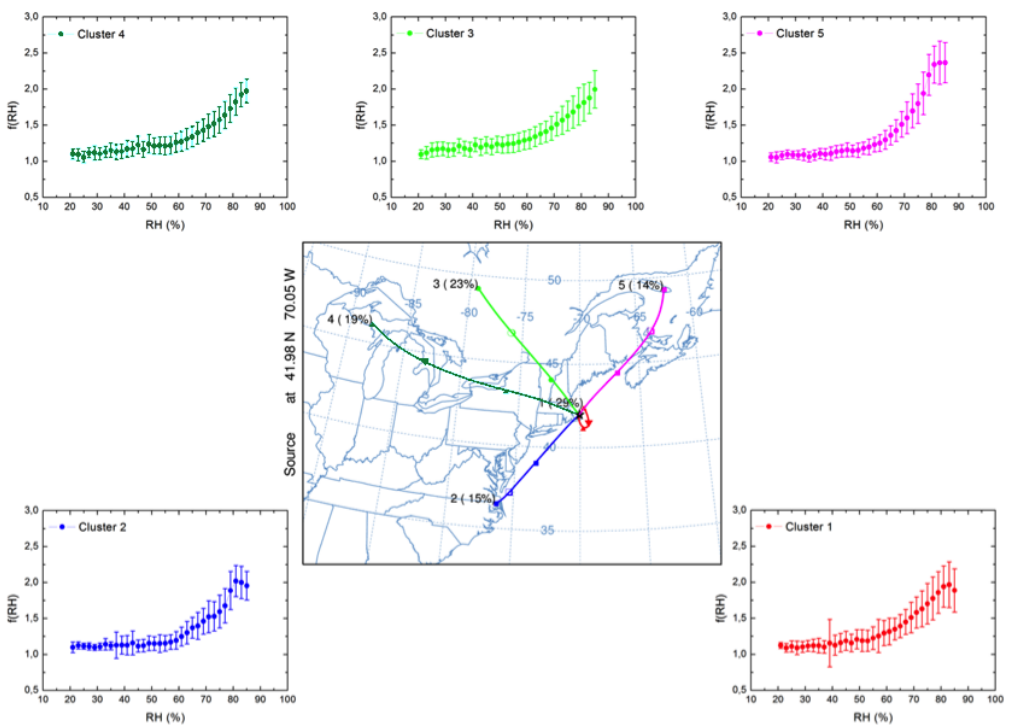


Figure 6-15: Clustering of 3-days air masses backtrajectories arriving at Cape Cod at 500 m a.g.l. at 00, 06, 12 and 18 GMT according to the HYSPLIT4 model (central panel) and average humidograms for each cluster. The error bars denote the standard deviation.

Clusters 1-4 exhibited similar aerosol optical properties with only small differences. Cluster 5 was characterized by small $SAE(450-700)$ and high $\omega_0(550 \text{ nm})$, as well as by high γ and $f(\text{RH}=80\%)$ values. The air masses included in this cluster came from the north-east, some of them originating as far away as Greenland, passing over sparsely-populated regions and the Atlantic Ocean. The high $SAE(450-700)$ for cluster 4 together with a lower $\omega_0(550 \text{ nm})$ denotes an anthropogenic influence. Clusters 3 and 4 had similar characteristics in terms of the aerosol optical properties (see Figure 6-15 and Table 6-6). Both clusters comprise continental air masses. Clusters 1 and 2 had hybrid properties: with a predominance of larger particles compared to cluster 3 and 4 and with higher $\omega_0(550 \text{ nm})$ values. This is probably because the air masses in clusters 1

and 2 passed over open Ocean but originated in polluted continental regions. The cluster to cluster variation in the aerosol optical properties can be explained by the degree of anthropogenic and marine influence in the air masses included in each cluster.

6.2.7 Relationship between γ and ω_0 and SAE

Predictive capability and global coverage of aerosol hygroscopicity for use in climate models would be enhanced if other aerosol parameters could be used as proxies to estimate hygroscopic growth. Toward this goal, we examined covariances between γ and aerosol intensive properties. Figure 6-16 shows the frequency distribution of γ in the PM₁₀ fraction for different SAE(450-700) and ω_0 (550 nm) ranges. Values of SAE(450-700) below 1 denote a higher predominance of coarse particles and lower ω_0 (550 nm) values indicate darker aerosols. From Figure 6-16b, it is clear that aerosols containing a higher fraction of absorbing particles (lower ω_0) are less hygroscopic since the frequency distribution is shifted towards lower γ values. In contrast, Figure 6-16a suggest that when coarse aerosols predominate ($SAE(450-700) < 1$) the hygroscopic enhancement is larger. In general, γ decreased as the contribution of coarse particles decreased, that is, as SAE(450-700) increased (the correlation coefficient of γ versus SAE(450-700) was $R = -0.77$). This result contrasts with the result of Zieger *et al.* [2010] that showed a decrease of γ for an increase in the contribution of coarse particles ($R=0.34$), probably connected with compensating effects of different varying aerosol properties during their study.

Because the γ frequency distribution segregates well between high and low values of ω_0 (550 nm) and SAE(450-700), these variables seem to be good candidates as proxies to estimate the scattering enhancement due to water

uptake. Based on the previous results, the following question arises: Can the aerosol hygroscopicity be predicted based on dry optical properties? To answer this question, Figure 6-17 (upper panel) shows γ versus $\omega_0(550 \text{ nm})$ where the color code represents the range of SAE(450-700). Figure 6-17a refers to γ in PM_1 and Figure 6-17b refers to γ in PM_{10} . In both γ graphs, SAE(450-700) and $\omega_0(550 \text{ nm})$ corresponds to the PM_{10} size fraction and to dry conditions. The $\text{PM}_1 \gamma$ was referenced to $\text{PM}_{10} \omega_0$ and SAE as a mean to make the fits applicable to surface measurements which may have only PM_{10} data and still differentiate the total and fine mode aerosol for models. As $\omega_0(550 \text{ nm})$ values increase the contribution of coarse particles also increases and these particles become more hygroscopic (bluish colors in Figure 6-17).

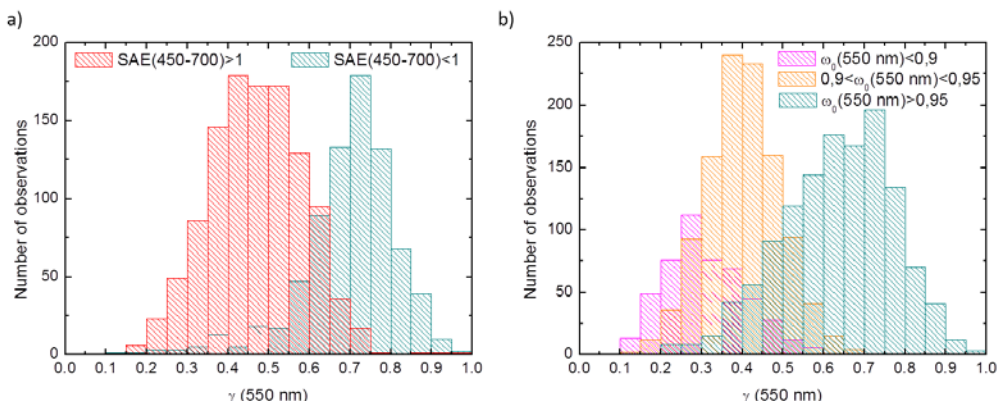


Figure 6-16: Frequency distribution of the γ parameter for different scattering Ångström exponent (a) and single scattering albedo (b) ranges in the PM_{10} size fraction.

The increase of γ with ω_0 in 550 nm wavelength is well described by the following exponential functions for the PM_1 (Eq. 6.5) and PM_{10} (Eq. 6.6) size fractions respectively:

$$\gamma = (3 \pm 5) \cdot 10^{-15} e^{\frac{\omega_0(550 \text{ nm})}{(0.030 \pm 0.001)}} + (0.31 \pm 0.01) \quad \text{Eq. 6.5}$$

$$\gamma = (4 \pm 3) \cdot 10^{-9} e^{\frac{\omega_0(550 \text{ nm})}{(0.054 \pm 0.002)}} + (0.26 \pm 0.01) \quad \text{Eq. 6.6}$$

The coefficient of determination was $R^2 = 0.76$ in PM_1 and $R^2 = 0.77$ in PM_{10} . The increase observed in γ for higher $\omega_0(550 \text{ nm})$ values is more pronounced in the PM_1 than in the PM_{10} size fractions. Figure 6-17 (lower panel) shows the frequency distribution of the residuals for the fit in PM_1 and in PM_{10} , respectively, in order to assess the quality of the regression. About 79% of the γ values in PM_1 and 92% in PM_{10} were estimated by the model with a difference of ± 0.15 in γ . The residuals did not exhibit any dependence on $\text{SAE}(450-700)$, suggesting that the exponential fit captures most of the covariance between $\text{SAE}(450-700)$ and $\omega_0(550 \text{ nm})$. The potential of this model lies in its simplicity, as the aerosol hygroscopicity can be estimated by a single parameter, the dry single scattering albedo.

Quinn et al. [2005] proposed a parameterization based on the aerosol chemical composition, in particular, in the fraction of particulate organic matter to predict $f(\text{RH})$. Also based on the chemical composition, *Garland et al.* [2007] reported that the $f(\text{RH}=80\%)$ varied linearly with the organic/inorganic content. However, measurements of aerosol chemical composition are commonly performed once a week and integrated over a 24 hour period whereas optical properties are continuously measured at high time resolution. In this particular study, the coarse mode was predominantly dominated by sea salt particles and the presence of other species that typically accumulate in the coarse fraction like dust particles was negligible. Due to the similar characteristics of sea salt and dust particles in terms of $\text{SAE}(450-700)$ and $\omega_0(550 \text{ nm})$, but the strong difference in the hygroscopic behavior, the parameterization proposed in this study would fail under the presence of both types of aerosols as pure dust aerosols does not experience significant hygroscopic growth. The Cape Cod study may be considered as representative of an aerosol from the Northern Atlantic coast with anthropogenic influence.

The same analysis needs to be applied to other regions and aerosol types to catalog exponential fit parameters of γ versus $\omega_0(550 \text{ nm})$ over a variety of aerosol types and atmospheric conditions.

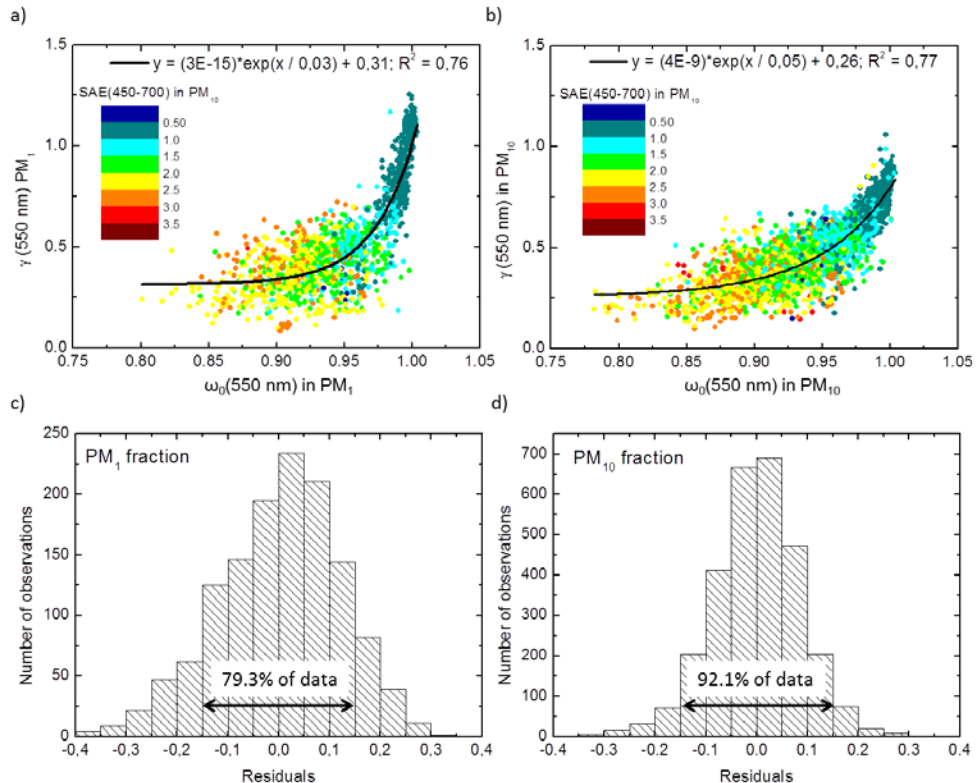


Figure 6-17: γ parameter in PM_1 (a) and PM_{10} (b) versus the single scattering albedo in PM_{10} . The color code corresponds to the scattering Ångström exponent in PM_{10} . An exponential fit has been added to the plot (black line). The residuals of these regressions are plotted as frequency distributions for PM_1 (c) and PM_{10} (d) size fractions.

6.2.8 Conclusions

During the study period, $f(\text{RH}=80\%)$ and the fit parameter γ in PM_{10} had a mean value of 1.9 and 0.5, respectively. Two distinct sectors were identified according to wind speed and direction. For the marine sector (wind speed above 5 m/s and wind direction between 0 and 180 degrees), the γ parameter had a mean value of 0.7 ± 0.1 for $\gamma_{>65\%}$, which was considerably higher than for $\gamma_{<65\%}$.

The sharp increase in $f(\text{RH})$ at an RH above 65% indicated the aerosol deliquescence. For the anthropogenically-influenced sector (wind speed above 5 m/s and wind direction between 225 and 315 degrees) the aerosol particles were characterized by a predominance of smaller and darker aerosols with lower hygroscopicity. The enhanced fine mode hygroscopic growth was more pronounced for the marine sector than for the anthropogenically-influenced sector. The air-mass trajectory classification analysis agreed with the wind sector analysis. Small differences were found between clusters, with the exception of cluster 5 that corresponds to clean marine air masses.

A clear relationship between the intensive parameters $\omega_0(550 \text{ nm})$ and $\text{SAE}(450-700)$ with γ was observed. The γ parameter increased for increasing $\omega_0(550 \text{ nm})$ and decreasing $\text{SAE}(450-700)$ values, that is, larger and less absorbing particles tended to be more hygroscopic. An exponential equation which fit γ to a single parameter (the single scattering albedo) was found to have a relatively low residual error, suggesting that $\omega_0(550 \text{ nm})$ was a good proxy of the aerosol scattering hygroscopic growth. The Cape Cod study represents aerosol from a Northern Atlantic coastal site with influence of marine and anthropogenic aerosols. The same analysis needs to be applied to other regions and aerosol types to catalog exponential fit parameters of γ versus $\omega_0(550 \text{ nm})$ over a variety of aerosol types and atmospheric conditions. This particular study had a strong covariance between $\omega_0(550 \text{ nm})$ and $\text{SAE}(450-700)$, which allowed a reduction in the γ fit to a single parameter, $\omega_0(550 \text{ nm})$. Other sites with smoke, dust or with strong differences in aerosol composition between the fine and coarse mode may require more fit parameters.

7 General conclusions and perspectives

This section presents the main conclusions reached in the development of this thesis.

The chemical composition of fine and coarse particulate matter has been studied for the period 2006-2010 in Granada. A significant decreasing trend in PM₁₀ levels has been observed related with a decrease in most of its constituents, specially marked in mineral matter levels and non-mineral carbon. The main sources contributing to the aerosol load were identified by means of the Positive Matrix Factorization technique. This analysis resulted in the identification of five sources in PM₁₀₋₁ and four in PM₁. In spite of being relatively uncommon, the use of fine and coarse PM in the PMF analysis separately was found to be very useful to discriminate additional sources. The regional re-circulation source was traced by secondary sulphate, V and Ni. It was the most important source concerning PM₁ mass concentration being less important in the coarse fraction. The traffic exhaust source that was characterized by nitrate, ammonium and carbonaceous particles, comprised 29% of the fine mass. Traffic related sources contribute around 64% to the fine fraction during winter time. PM₁₀₋₁ levels decreased from working to non-working days, especially due to reduction in the contribution of mineral dust, celestite mines and road dust sources. On the other hand, PM₁ levels and the concentrations of each source remained fairly constant throughout the week. PM₁₀ exceedances (2008/50/EC) with an anthropogenic origin predominantly affected the fine fraction and occurred more often during the cold seasons. As a concluding remark, traffic seems to be the main source to target in Granada throughout the year, but especially in winter.

In order to study the relationship between aerosol optical properties and the chemical composition, the total scattering and absorption coefficients and speciated PM₁₀ and PM₁ data were combined for a period of one year. Different

methodologies were applied to determine the mass scattering and absorption efficiencies. Fine particles were found to extinct light more efficiently than coarse particles, although extinction by coarse particles should not be neglected as previous works suggested. Among the different aerosol constituents, SO_4^{2-} -nm exhibited the largest mass scattering efficiency ($7\pm1 \text{ m}^2\text{g}^{-1}$), followed by nitrate ($5\pm2 \text{ m}^2\text{g}^{-1}$) and OM+EC particles ($2.8\pm0.4 \text{ m}^2\text{g}^{-1}$) whilst dust aerosols presented the lowest mass scattering efficiency ($0.2\pm0.3 \text{ m}^2\text{g}^{-1}$). Several previous works only considered sulphate when computing aerosol mass scattering efficiencies, however, from the results obtained in this thesis it is clear that other species play an important role in the scattering process that should be taken into account. On the other hand, the absorption process was found to be mainly dominated by carbonaceous particles. The mass scattering and absorption efficiencies obtained in this study can be used to estimate the scattering and absorption coefficients and, hence, the radiative effect of the aerosol particles from chemical composition data.

The aerosol scattering coefficient is highly influenced by the ability of particles to take up water, which results also in changes in the radiative forcing estimations. Since the aerosol scattering coefficient is typically measured at dry conditions, knowledge of the scattering enhancement due to water uptake is of great importance in order to convert dry measurements into more relevant ambient data. To this end, a humidification system was developed and built in the frame of this thesis for an integrating nephelometer. After successfully testing the humidifier in the laboratory, two measurement campaigns were conducted in Granada during winter and spring seasons. The scattering enhancement factor, $f(\text{RH}=85\%)$, was 1.5 ± 0.2 and 1.6 ± 0.3 during the winter and spring campaigns, respectively. It was found to undergo a clear diurnal pattern. The two $f(\text{RH}=85\%)$ minima were connected to the relative increase of

the non-hygroscopic fraction (such as black carbon and road dust) due to traffic emissions during the traffic rush hours. Differences in the chemical composition during both campaigns resulted in differences in the hygroscopic behavior of aerosol particles. A decreasing trend of $f(\text{RH}=85\%)$ for increasing mass fraction of particulate organic matter was found. Due to the low ambient RH values, the hygroscopic growth did not affect significantly the radiative forcing estimations. However, for situations of elevated RH this effect should be taken into account in order to report accurate estimations of the radiative effect of aerosols. The radiative forcing efficiency changed from -13 Wm^{-2} at dry conditions to -17 Wm^{-2} at 85% relative humidity.

At Cape Cod (Massachusetts, USA), the RH dependency of the scattering coefficient was found to be higher than at Granada due to the influence of marine aerosols. $f(\text{RH}=80\%)$ had a mean value of 1.9 ± 0.3 over the measurement period. Two wind sectors were clearly identified: one dominated by anthropogenic emissions and the other one dominated by clean marine aerosols. For the marine sector, a sharp increase in $f(\text{RH})$ at an RH above 65% was observed, indicating aerosol deliquescence. A clear relationship between the single scattering albedo, $\omega_0(550 \text{ nm})$, and the scattering Ångström exponent, $SAE(450-700)$, with aerosol hygroscopicity (γ) was observed. The γ parameter increased for increasing $\omega_0(550 \text{ nm})$ and decreasing $SAE(450-700)$ values, that is, larger and less absorbing particles tended to be more hygroscopic. An exponential equation which fit γ to the single scattering albedo was found to have a relatively low residual error, suggesting that ω_0 can be a good proxy of the aerosol scattering hygroscopic growth.

Future research will be necessary in order to continue with the advancement in the aspects developed in this thesis, making emphasis in some topics:

- A longer database of aerosol chemical composition (from 2006 to 2014) will allow determining to what extent the decrease observed in PM₁₀ levels has continued and to constraint the significance of this reduction. In this sense, the combination of this longer database of aerosol chemical composition with the aerosol optical properties database will provide additional information on aerosol temporal trends.
- Long-term aerosol hygroscopicity measurements at Granada will be of great interest since most published works focused on short measurement campaigns. In this sense, the relationship observed between the aerosol hygroscopicity and the relative content of organic material will be addressed with a higher statistical significance.
- The systematic analysis of $f(RH)$ versus RH (so-called humidograms) with scanning RH protocols will be used to better characterize aerosol hygroscopicity at Granada.
- The installation of the humidified nephelometer in a high altitude site in the Sierra Nevada range will allow us to validate lidar measurements without any assumptions of aerosol hygroscopic behavior at ambient RH.
- Study of the relationship between aerosol hygroscopicity and the single scattering albedo and the Ångström exponent at sites with different atmospheric conditions and aerosol characteristics will allow us to test the equation obtained in this thesis to estimate aerosol hygroscopicity from single scattering albedo data.

Conclusiones generales y perspectivas

En esta sección se presentan las principales conclusiones alcanzadas en el desarrollo de esta tesis doctoral.

La composición química de los modos fino y grueso del aerosol atmosférico se ha estudiado para el periodo 2006-2010 en Granada. En este periodo, se ha observado un descenso significativo en los niveles de PM₁₀ y de sus principales constituyentes. Las principales fuentes de aerosol atmosférico se han identificado y cuantificado con la técnica de factorización matricial positiva. Con esta técnica se identificaron cinco fuentes en el modo grueso y 4 en el modo fino, evidenciando que el uso de las fracciones fina y gruesa de forma independiente aporta información adicional sobre las fuentes de aerosol. La fuente relacionada con re-circulación regional estaba caracterizada por sulfato secundario, V y Ni. Esta fuente resultó ser la más importante en relación a la concentración del modo fino. Las fuentes de aerosol relacionadas con el tráfico rodado contribuyeron de forma muy significativa al PM₁, siendo esta contribución de hasta 64% durante el invierno. Se ha encontrado que los niveles de la fracción gruesa disminuyen los días no laborables respecto a los días de semana, debido fundamentalmente a una reducción en las fuentes relacionadas con el polvo mineral, las minas de celestita y el polvo del tráfico. Por otro lado, los niveles de la fracción fina y la contribución de las diferentes fuentes a los mismos se mantienen prácticamente constantes a lo largo de la semana. Las superaciones de los límites establecidos por la legislación (2008/50/EC) para los niveles de PM₁₀ relacionados con causas antropogénicas sucedieron de forma más frecuente durante el invierno. El tráfico se perfila como la principal fuente a regular en Granada a lo largo del año, pero especialmente en invierno, para reducir los niveles de PM.

Para estudiar la relación entre las propiedades ópticas de las partículas de aerosol atmosférico y su composición química, los coeficientes de dispersión

y absorción de aerosoles y la composición química de las fracciones PM₁₀ y PM₁ se han combinado durante un periodo de un año. Aplicando diferentes metodologías existentes, se ha obtenido que las partículas finas extinguen la radiación de forma más eficiente que las partículas gruesas, si bien la extinción causada por las partículas gruesas no es despreciable. Entre los principales constituyentes químicos del aerosol atmosférico, el sulfato de origen no marino es el que presenta una mayor eficiencia mísica de dispersión ($7\pm1 \text{ m}^2\text{g}^{-1}$) seguido por las partículas de nitrato ($5\pm2 \text{ m}^2\text{g}^{-1}$) y OM+EC ($2.8\pm0.4 \text{ m}^2\text{g}^{-1}$) mientras que el polvo mineral presenta la menor eficiencia mísica de dispersión ($0.2\pm0.3 \text{ m}^2\text{g}^{-1}$). Muchos trabajos previos sólo consideraron el sulfato a la hora de calcular las eficiencias mísicas de dispersión, sin embargo, en vista de los resultados obtenidos en esta tesis es evidente que otras especies juegan un papel muy importante en el proceso de dispersión que debe tenerse en cuenta. Por otro lado, el proceso de absorción se encuentra dominado por las partículas de tipo carbonoso. Las eficiencias mísicas de dispersión y absorción obtenidas en esta tesis pueden utilizarse para estimar los coeficientes de dispersión y absorción, y por tanto, el efecto radiativo de las partículas de aerosol atmosférico a través de datos de su composición química.

El coeficiente de dispersión de aerosoles está altamente influenciado por la habilidad de las partículas de captar agua, lo que afecta también las estimaciones de forzamiento radiativo. Puesto que el coeficiente de dispersión de aerosoles es medido normalmente en condiciones secas, conocer el realce en el coeficiente de dispersión debido al crecimiento higroscópico es de gran importancia para poder convertir las medidas secas en medidas ambiente, de mayor relevancia climática. Para ello, y en el marco de esta tesis doctoral, se ha desarrollado y construido un sistema de humidificación para el nefelómetro integrante. Después de verificar el correcto funcionamiento del humidificador

en el laboratorio, se llevaron a cabo dos campañas de medida durante invierno y primavera en Granada. El factor de realce en el coeficiente de dispersión, $f(RH=85\%)$, presentó un valor medio de 1.5 ± 0.2 y 1.6 ± 0.3 en las campañas de invierno y primavera, respectivamente. Durante el periodo de estudio, se ha encontrado que el factor $f(RH=85\%)$ tiene un marcado ciclo diurno, con dos mínimos en coincidencia con las horas de tráfico intenso. Estos mínimos están relacionados con el aumento de la fracción no higroscópica como el carbono negro y el polvo mineral durante esas horas debido al tráfico rodado. Diferencias en la composición química del aerosol atmosférico durante ambas campañas de medida explican las diferencias en las propiedades higroscópicas observadas en invierno y primavera. Además, el factor $f(RH=85\%)$ decrece conforme aumenta la fracción de materia orgánica, lo que evidencia la importancia de la composición química en la magnitud del factor $f(RH=85\%)$. Debido a la baja humedad relativa ambiente durante el periodo de medida, el crecimiento higroscópico no afectó significativamente a las estimaciones de forzamiento radiativo. Sin embargo, para situaciones de elevada humedad relativa este efecto sí debería tenerse en cuenta con objeto de realizar estimaciones precisas del forzamiento radiativo. La eficiencia de forzamiento radiativo varió de -13 Wm^{-2} en condiciones secas a -17 Wm^{-2} en condiciones de humedad relativa igual a 85%.

En Cape Cod (Massachusetts, EEUU), la dependencia del coeficiente de dispersión de aerosoles con la humedad relativa es mayor que en Granada debido fundamentalmente a la influencia de aerosol marino. $f(RH=80\%)$ presentó un valor promedio de 1.9 ± 0.3 durante el periodo de estudio. Se identificaron de forma clara dos sectores de viento: uno dominado por emisiones de tipo antropogénico y el otro caracterizado por condiciones marinas limpias. Para el sector marino, se observó un aumento brusco en el

factor $f(RH)$ a humedades relativas en torno al 65%, indicativo de aerosol de tipo delicuescente. En este estudio, se observó una clara relación entre el albedo de dispersión simple y el exponente de Ångström de dispersión con el factor de crecimiento higroscópico. Así mismo, se encontró una ecuación exponencial capaz de estimar de forma satisfactoria y con bajo error residual el realce en el coeficiente de dispersión debido al crecimiento higroscópico utilizando el albedo de dispersión simple.

Para continuar con el avance de los aspectos desarrollados en esta tesis, será necesaria realizar en el futuro una investigación más exhaustiva de ciertos aspectos puestos de manifiesto en este estudio. Así:

- Una base de datos más larga de la composición química de aerosoles (desde 2006 hasta 2014) permitirá determinar hasta qué punto el descenso observado en los niveles de PM₁₀ ha continuado hasta la actualidad y precisar la significación de este descenso. En este sentido, la combinación de esta base de datos larga de composición química combinada con la de propiedades ópticas de las partículas de aerosol proporcionará información adicional sobre posibles tendencias y cambios temporales.
- Medidas de la higroscopicidad de aerosoles a largo plazo en Granada será de gran interés ya que la mayoría de los trabajos publicados se centran en períodos de medida cortos. En este sentido, la relación observada entre la higroscopicidad y el contenido relativo de material orgánico se podrá abordar con una mayor significación estadística.
- El análisis sistemático de las curvas $f(RH)$ -RH (también llamados humidogramas) con medidas de $f(RH)$ escaneando la humedad relativa servirá para proporcionar una mejor caracterización de las propiedades higroscópicas del aerosol en Granada.

- La instalación del nefelómetro húmedo en un sitio en altura en Sierra Nevada permitirá validar las medidas lidar sin tener que realizar suposiciones sobre el coeficiente de dispersión en condiciones de humedad relativa ambiente.
- Estudiar la relación entre el albedo de dispersión simple, el exponente de Ångström de dispersión y la higroscopidad del aerosol atmosférico en diferentes sitios con condiciones atmosféricas diferentes y caracterizados por diferentes tipos de aerosol permitirá validar la ecuación propuesta en esta tesis para estimar la higroscopidad a través de valores de albedo de dispersión simple.

Quick finder

List of symbols and acronyms

ACTRIS	Aerosols, Clouds and Trace gases InfraStructure network
ADL	Above Detection Limit
a.s.l.	above sea level
a.g.l.	above ground level
AOS	Aerosol Observing System
ARM	Atmospheric Radiation Measurements
AR4	Fourth Assessment Report of the IPCC
AR5	Fifth Assessment Report of the IPCC
BC	Black carbon
CCN	Cloud Condensation Nuclei
CEAMA	Centro Andaluz de Medio Ambiente
DOE	Department Of Energy
DRH	Deliquescence Relative Humidity
EC	Elemental Carbon
ERH	Efflorescence Relative Humidity
ESRL	Earth System Research Laboratory
GFAT	Atmospheric Physics Group
GMT	Greenwich Mean Time
HTDMA	Humidified Tandem Differential Mobility Analyzers
HYSPLIT	Hybrid single-particle Lagrangian integrated trajectories
ICP-AES	Inductively Coupled Plasma Atomic Emission Spectrometry
ICP-MS	Inductively Coupled Plasma Mass Spectrometry
IISTA	Instituto Interuniversitario del Sistema Tierra de Andalucía
IMPROVE	Interagency Monitoring of PROtected Visual Environments
IPCC	Intergovernmental Panel on Climate Change
Lidar	light detection and ranging
lpm	liters per minute
MAAP	Multi-Angle Absorption Photometer
MLR	Multiple Linear Regression
NOAA	North Oceanic and Atmospheric Administration
OC	Organic Carbon
OM	Organic Matter
PCA	Principal Component Analysis
PID	Proportional-Integral-Derivative
PM	Particulate Matter
PMF	Positive Matrix Factorization

PMT	Photomultiplier tubes
PSAP	Particle Soot Absorption Photometer
PTFE	Polytetrafluoroethylene
RF	Radiative Forcing
RH	Relative Humidity
SD	Standard Deviation
SIA	Secondary Inorganic Aerosols
S/N	Signal to Noise ratio
TCAP	Two Column Aerosol Project
TROPOS	Leibniz Institute for Tropospheric Research
VOC	Volatile Organic Compound
α_{sp}	Aerosol particles mass scattering efficiency
α_{ap}	Aerosol particles mass absorption efficiency
b	backscatter fraction
β	upscatter fraction
C	Correction factor for the nephelometer
C_t	Total carbon
δ	Aerosol optical depth
D_p	Particle diameter
E	Residual matrix
γ	fitting parameter of the scattering enhancement factor
L	radiance
λ	wavelength
f(RH)	Scattering enhancement factor
F	Source profile
G	Source contribution
n	real part of the refractive index
nmC	non-mineral carbon
SO_4^{2-} nm	non-marine sulphate
Q	Objective function
R_{sp}	Submicron scattering fraction
SAE	Scattering Ångström Exponent
σ_{sca}	Total light-scattering coefficient
σ_{abs}	Total light-absorption coefficient
σ_{ext}	Total light-extinction coefficient
σ_{sp}	Aerosol particles light-scattering coefficient
σ_{bsp}	Aerosol particles backscattering coefficient
σ_{ap}	Aerosol particles light-absorption coefficient
σ_{rg}	Rayleigh scattering coefficient
σ_{ag}	Absorption coefficient by gas molecules

σ_{ij}	Elements of the uncertainty matrix
θ	Scattering angle
ω_0	Single scattering albedo
x	size parameter
X	Data matrix

List of figures

Figure 2-1: Idealized scheme of the distribution of particle surface area of an atmospheric aerosol. Principal modes, sources and particle formation and removal mechanisms are also indicated (Figure taken from Zieger [2011], originally adapted from Whitby and Cantrell, 1976; Seinfeld and Pandis, 1998; Heintzenberg et al., 2003].	22
Figure 2-2: Radiative forcing estimates in 2011 relative to 1750 and aggregated uncertainties for the main drivers of climate change taken from IPCC [2013]. Values are global average radiative forcing. The best estimates of the net radiative forcing are shown as black diamonds with corresponding uncertainty intervals; the numerical values are provided on the right of the figure, together with the confidence level in the net forcing (VH – very high, H – high, M – medium, L – low, VL – very low). Total anthropogenic radiative forcing is provided for three different years relative to 1750.	26
Figure 2-3: Attenuation of radiation	28
Figure 2-4: Rayleigh scattering and Mie scattering.	30
Figure 2-5: Diameter change of $(\text{NH}_4)_2\text{SO}_4$, NH_4HSO_4 , and H_2SO_4 particles as a function of relative humidity. D_{p0} is the diameter at 0% RH [from Seinfeld and Pandis, 1998].	32
Figure 2-6: Humidograph example of f(RH) versus RH for 7 May 2014 10:00-10:30 GMT. The RH was measured inside the nephelometer (RH_TSI refers to the original TSI RH sample sensor and RH_wet refers to the co-located Rotronic sensor).	43
Figure 3-1: Schematic representation of the TSI 3563 integrating nephelometer.	49
Figure 3-2: Schematic of the reference chopper	50
Figure 3-3: Schematic representation of the experimental set-up.....	53

Figure 3-4: Outer and inner tubes constituting the humidifier. The inner one is a high density porous PTFE (polytetrafluoroethylene) tube and the outer tube is made up of stainless steel.....	54
Figure 3-5: The outer stainless steel tube wrapped by a cable heater.....	54
Figure 3-6: Control box for the humidifier system (frontal, a, and upper, b, views).	55
Figure 3-7: Main screen of the NOAA LiveCPD software.	56
Figure 3-8: Optical sensor of the MAAP. Left: Position of the photodetectors at detection angles $\theta_0 = 0^\circ$, $\theta_1 = 130^\circ$ and $\theta_2 = 165^\circ$ with respect to the incident light beam. Right: Layout of the MAAP sensor unit, the arrows indicate the airflow through the sensor unit across the filter tape.....	58
Figure 3-9: Schematic representation of radiation processes considered in the two-layer system consisting of an aerosol loaded filter layer and the particle-free filter matrix.	59
Figure 4-1: Chemical composition of PM_{10-1} (lower panel) and PM_1 (upper panel) in winter and in summer expressed in $\mu\text{g}/\text{m}^3$ and percentage (%).72	72
Figure 4-2: PM_1/PM_{10} ratios of the major and some trace elements.	73
Figure 4-3: Source profiles found for the coarse fraction (PM_{10-1}) and percentage of ambient species concentration apportioned by each source.	78
Figure 4-4: Source profiles found for the fine fraction (PM_1) and percentage of ambient species concentration apportioned by each source.....	79
Figure 4-5: Contribution of sources to PM_{10-1} (upper panel) and PM_1 (lower pannel) in winter (left) and summer (right) expressed in $\mu\text{g}/\text{m}^3$ and corresponding percentage.....	81
Figure 4-6: Location map (top) of the monitoring site and polar plots (bottom) of the PM source concentration in $\mu\text{g}/\text{m}^3$ (color scale) obtained with PMF according to wind direction.....	82
Figure 4-7: Average concentrations of each source for Monday to Friday, Saturday and Sunday, for the coarse fraction (upper panel) and for the fine fraction (lower panel). The error bars represent the standard deviations (SD). The average \pm SD measured PM mass concentration for each period is also shown in a box.....	84
Figure 5-1: Annual mean composition in % of PM_{10-1} and PM_1 fractions for the period from March 2006 to February 2007.....	95
Figure 5-2: Daily mean value and standard deviation of $\sigma_{sp}(550 \text{ nm})$ and $\sigma_{ap}(550 \text{ nm})$ measured at RH<50%.	96
Figure 5-3: Scattering Ångström exponent calculated between 450-700 nm versus PM_{10}/PM_1 ratio.....	99

Figure 5-4: Absorption coefficient at 550 nm versus nmC mass concentration in the PM ₁₀ fraction and the corresponding linear fit.....	106
Figure 6-1: Chemical speciation of PM ₁₀ fraction during winter and spring campaigns expressed in percentage (%).The unaccounted mass fraction refers to the percentage of mass that was not determined by chemical analysis compared to the gravimetric PM ₁₀ mass. Mineral fraction was calculated as the sum of Al ₂ O ₃ , SiO ₂ , CO ₃ , Ca, Fe, Mg, K, trace elements as the sum of Li, P, Sc, Ti, V, Cr, Mn, Co, Ni, Cu, Zn, Ga, Ge, As, Se, Rb, Sr, Cd, Sn, Sb, Cs, Ba, La, Ce, Lu, Hf, Ta, W, Tl, Pb, Bi, Th and U) and OM as OC*1.6.	112
Figure 6-2: Time series of hourly average values of the scattering and absorption coefficients, single scattering albedo, scattering Ångström exponent and $f(RH=85\%)$ during the winter campaign.....	116
Figure 6-3: Time series of hourly average values of the scattering and absorption coefficients, single scattering albedo, scattering Ångström exponent and $f(RH=85\%)$ during the spring campaign.....	117
Figure 6-4: Diurnal evolution of the scattering coefficient at 550 nm, absorption coefficient at 637 nm, scattering enhancement factor at 85% RH and 550 nm, single scattering albedo at 637 nm and scattering Ångström exponent during the winter (upper panel) and spring (lower panel) campaigns....	120
Figure 6-5: Aerosol light-scattering enhancement factor versus RH during different time periods in the winter (a) and spring (b) campaigns. Each point represents the average $f(RH)$ value in 2% RH size bins.....	122
Figure 6-6: Frequency distribution of $f(RH=85\%)$ at 550 nm during the winter and spring campaigns. Data for periods where SAE(dry, 450-700) was above and below 1 and $\omega_0(\text{dry}, 637 \text{ nm})$ was above and below 0.6 were extracted and plotted separately.....	126
Figure 6-7: Scattering enhancement factor at 85% relative humidity versus the ratio OM/(OM+SO ₄ ²⁻) for the winter and spring campaigns. The linear fit refers to dust free conditions.....	128
Figure 6-8: Time series of daily a) Ambient relative humidity, b) single scattering albedo at 550 nm , c) backscatter fraction at 550 nm and d) aerosol forcing efficiency at 550 nm at dry, ambient RH and RH =85% during the spring campaign.	131
Figure 6-9: Temporal evolution of the daily dry scattering and absorption coefficients (upper panel), the single scattering albedo (middle panel) and the scattering Ångström exponent (lower panel). All the parameters correspond to the PM10 fraction. The date is in the format dd/mm/yyyy.	142

Figure 6-10: Temporal evolution of the daily scattering enhancement factor at 80% relative humidity (upper panel) and the fit parameter γ (lower panel), for PM ₁₀ and PM ₁ fractions. The date is in the format dd/mm/yyyy.	142
Figure 6-11: Scatter plot of the hourly average scattering enhancement factors at 80% relative humidity in the PM ₁ fraction versus the same parameter in the PM ₁₀ fraction. Data when the scattering Ångström exponent was below and above 1 were fitted separately.	144
Figure 6-12: Example humidograms of the scattering enhancement factor, given as daily averages where the error bars represent the standard deviation for the 9 th of March (a) and the 31 st of May (b). The black line denotes the γ fit for the entire RH range (RH>40%), the blue line denotes the γ fit for RH>65% and the red line the γ fit for the RH<65%.	145
Figure 6-13: Bivariate plots of the scattering enhancement factor at 80% RH, the γ parameter, single scattering albedo and scattering Ångström exponent as a function of wind speed and direction.	147
Figure 6-14: Wind sector separation super-imposed on a Google maps image centered in Cape Cod.	148
Figure 6-15: Clusterization of 3-days air masses backtrajectories arriving at Cape Cod at 500 m a.g.l. at 00, 06, 12 and 18 GMT according to the HYSPLIT4 model (central panel) and average humidograms for each cluster. The error bars denote the standard deviation.	151
Figure 6-16: Frequency distribution of the γ parameter for different scattering Ångström exponent (a) and single scattering albedo (b) ranges in the PM ₁₀ size fraction.	153
Figure 6-17: γ parameter in PM ₁ (a) and PM ₁₀ (b) versus the single scattering albedo in PM ₁₀ . The color code corresponds to the scattering Ångström exponent in PM ₁₀ . An exponential fit has been added to the plot (black line). The residuals of these regressions are plotted as frequency distributions for PM ₁ (c) and PM ₁₀ (d) size fractions.	155

List of tables

Table 3-1: Correction factors for total scattering as a function of the Angström exponent using $C = a + b \cdot SAE$ [Anderson and Ogren, 1998].	52
Table 4-1: Mean, standard deviation (SD), percentage of data above detection limit (% ADL) and uncensored signal-to-noise ratio (S/N) for the elements in the PM ₁₀₋₁ and PM ₁ fractions included in the PMF analyses.	69

Table 5-1: Basic statistical summary (mean value, standard deviation, maximum and minimum values) of the mass concentrations (in $\mu\text{g}/\text{m}^3$) for the major chemical species measured in PM_{10} , PM_1 and PM_{10-1} in Granada. N is the number of samples analyzed.....	94
Table 5-2: Summary of aerosol optical properties (mean value, standard deviation, median, maximum and minimum values and 25 and 75 percentiles).....	97
Table 5-3 Seasonal and annual mean values of the PM_{10} mass scattering and absorption efficiencies for the period from March 2006 to February 2007.	101
Table 6-1: Statistical summary of the aerosol dry scattering and absorption coefficients, single scattering albedo, scattering Ångström exponent and scattering enhancement factor at 85% RH during the winter and spring campaigns.	113
Table 6-2: Hygroscopic growth factors from the literature measured for different aerosol types. The values of $f(\text{RH})$ corresponds to the ratio of the aerosol light scattering coefficients (near 550 nm wavelength) at high RH and at dry conditions (RH<40%)......	118
Table 6-3: Mean and standard deviation of the dry scattering and absorption coefficients at 550 and 637 nm, respectively, single scattering albedo at 637 nm, scattering Ångström exponent for 450-700 nm, scattering enhancement factor at 85% RH and air mass classification during the humidograms (Med. Refers to Mediterranean air masses)	123
Table 6-4: Mean and standard deviation of single scattering albedo, scattering Ångström exponent, γ , $\gamma>65\%$, $\gamma<65\%$ and scattering enhancement factor at 80% RH for PM_{10} fraction and scattering enhancement factor at 80% RH for PM_1 fraction for the two wind sectors. All the variables refer to 550 nm except the scattering Ångström exponent that has been calculated between 450 and 700 nm.	148
Table 6-5: $f(\text{RH})$ values (near 550 nm wavelength) at RH of 85% unless noted (*RH = 82%, **RH=80%) reported in the literature for marine environments. Data correspond to a diameter, D_p , of 10 μm unless noted.	149
Table 6-6: Mean and standard deviation of single scattering albedo, scattering Ångström exponent, γ , $\gamma_{>65\%}$, $\gamma_{<65\%}$ and scattering enhancement factor at 80% RH for the five clusters. All the variables refer to PM_{10} unless specifically noted and to 550 nm except the scattering Ångström exponent that has been calculated between 450 and 700 nm.	151

References

- Albrecht BA. Aerosols, cloud microphysics, and fractional cloudiness, *Science*, 245(4923), 1227-1230, 1989.
- Almeida SM, Pio CA, Freitas MC, Reis MA, Trancoso MA. Source apportionment of atmospheric urban aerosol based on weekdays/weekend variability: evaluation of road re-suspended dust contribution. *Atmos. Environ.*, 40, 2058-2067, 2006.
- Amato F, Pandolfi M, Escrig A, Querol X, Alastuey A, Pey J, et al. Quantifying road dust resuspension in urban environment by multilinear engine: a comparison with PMF2. *Atmos. Environ.*, 43 (17), 2770-2780, 2009a.
- Amato F., Pandolfi M, Viana M, Querol X, Alastuey A, and Moreno T. Spatial and chemical patterns of PM10 in road dust deposited in urban environment, *Atmos. Environ.*, 43, 1650-1659, 2009b.
- Amato F, Pandolfi M, Moreno T, Furger M, Pey J, Alastuey A, et al. Sources and variability of inhalable road dust particles in three European cities. *Atmos. Environ.*, 45, 6777-6787, 2011.
- Amato F, Alastuey A, de la Rosa J, González-Castanedo Y, Sánchez de la Campa AM, Pandolfi M, et al. Trends of road dust emissions contributions on ambient PM levels at rural, urban and industrial sites in Southern Spain. *Atmos. Chem. Phys. Discuss.*, 13, 31933-31963, 2013.
- Anderson TL, and Ogren JA. Determining aerosol radiative properties using the TSI 3563 integrating nephelometer, *Aerosol Sci. Technol.*, 29, 57–69, 1998.
- Andreae TW, Andreae MO, and Ichoku C. Light scattering by dust and anthropogenic aerosol at a remote site in the Negev Desert, Israel. *J. Geophys. Res.*, 107 (D2), 4008, doi:10.1029/2001JD900252, 2002.
- Andreae MO, Schmid O, Yang H, Chand C, Yu JZ, Zeng L, and Zhang Y. Optical properties and chemical composition of the atmospheric aerosol in urban Guangzhou, China, *Atmos. Environ.*, 42, 6335-6350, 2008.
- Barmpadimos I, Keller J, Oderbolz D, Hueglin C, Prévôt ASH. One decade of parallel fine (PM2.5) and coarse (PM10-PM2.5) particulate matter measurements in Europe: trends and variability. *Atmos. Chem. Phys.*, 12, 3189-3203, 2012.
- Baron PA and Willeke K. *Aerosol Measurement: Principles, techniques and applications*, Wiley, New York, 2001.
- Bergin MH, Ogren JA, Schwartz SE, and McInnes LM. Evaporation of ammonium nitrate aerosol in a heated nephelometer: Implications for field measurements. *Environ. Sci. Technol.*, 31, 2878–2883, 1997.
- Bond TC, Anderson TL and Campbell D. Calibration and intercomparison of filter-based measurements of visible light absorption by aerosols. *Aerosol Sci. Technol.*, 30, 582– 600, 1999.

- Bond TC and Bergstrom RW. Light absorption by carbonaceous particles: An investigative review, *Aerosol Sci. Technol.*, 40(1), 27-67, doi:10.1080/02786820500421,521, 2005.
- Bryant C, Eleftheriadis K, Smolik J, Zdimal V, Mihalopoulos N, and Colbeck I. Optical properties of aerosols over the eastern Mediterranean, *Atmos. Environ.*, 40, 6229-6244, 2006.
- Calvo AI, Olmo FJ, Lyamani H, Alados-Arboledas L, Castro A, Fernández-Raga M and Fraile R. Chemical composition of wet precipitation at the background EMEP station in Víznar (Granada, Spain) (2002-2006). *Atmos. Res.*, 96, 2-3. 408-420, 2010.
- Calvo AI, Alves C, Castro A, Pont V, Vicente AM, Fraile R. Research on aerosol sources and chemical composition: Past, current and emerging issues. *Atmos. Res.*, 120-121, 1-28, 2013.
- Carrico CM, Rood MJ and Ogren JA. Aerosol light scattering properties at Cape Grim, Tasmania, during the First Aerosol Characterization Experiment (ACE 1), *J. Geophys. Res.*, 103, D13, 16565-16574, 1998.
- Carrico CM, Rood MJ, Ogren JA., Neusüb C, Wiedensohler A and Heintzenberg J. Aerosol optical properties at Sagres, Portugal during ACE-2, *Tellus*, 52B, 694-715, 2000.
- Carrico CM, Kus P, Rood MJ, Quinn PK. and Bates TS. Mixtures of pollution, dust, sea salt, and volcanic aerosol during ACE-Asia: Radiative properties as a function of relative humidity, *J. Geophys. Research.*, 108, D23, 8650, 2003.
- Carrico CM, Kreidenweis SM, Malm WC, Day DE, Lee T, Carrillo J, McMeeking GR and Collett JL. Hygroscopic growth behavior of a carbon-dominated aerosol in Yosemite National Park, *Atmos. Environ.*, 39, 1394–1404, 2005.
- Castillo S. Impacto de las masas de aire africano Sobre los niveles y composición del Material particulado atmosférico en Canarias y el NE de la península Ibérica, PhD Thesis, Centro Superior de Investigaciones Científicas, 2006.
- Cavalli F, Viana M, Yttri KE, Genberg J, Putaud JP. Toward a standardised thermal-optical protocol for measuring atmospheric organic and elemental carbon: the EUSAAR protocol. *Atmos. Meas. Tech.*, 3-1, 78-89, 2010.
- Charlson RJ, Schwartz SE, Hales JM, Cess RD, Coakley Jr JA, Hansen JE and Hofmann DJ. Climate forcing by anthropogenic aerosols, *Science*, 255(5043), 423-430, 1992.
- Charlson RJ, Anderson TL and Rodhe H. Direct climate forcing by anthropogenic aerosols: Quantifying the link between atmospheric sulphate and radiation, *Contrib. Atmos. Phys.* 72, 79-94, 1999.

- Cheng YF, Wiedensohler A, Eichler H, Su H, Gnauk T, Brüggemann E, Herrmann H, et al. Aerosol optical properties and related chemical apportionment at Xinken in Pearl River Delta of China, *Atmos. Environ.*, 42 6351–6372, 2008.
- Chow JC, Watson JG, Lowenthal DH and Richards LW. Comparability between PM_{2.5} and particle light scattering measurements, *Environ. Monit. Assess.*, 79, 29-45, 2002.
- Clarke AD, Howell S, Quinn PK, Bates TS, Ogren JA, Andrews E, Jefferson A, et al. INDOEX aerosol: A comparison and summary of chemical, microphysical, and optical properties observed from land, ship, and aircraft, *J. Geophys. Res.*, 107, 8033, 2002.
- Cook J and Highwood EJ. Climate response to tropospheric absorbing aerosols in an intermediate general-circulation model, *Quarterly Journal of the Royal Meteorological Society*, 130(596), 175-191, 2004.
- Covert DS, Charlson RJ and Ahlquist NC. A study of the relationship of chemical composition and humidity to light scattering by aerosols, *Journal of Applied Meteorology*, 11, 968-976, 1972.
- Cusack M, Alastuey A, Pérez N, Pey J, Querol X. Trends of particulate matter (PM_{2.5}) and chemical composition at a regional background site in the Western Mediterranean over the last nine years (2002-2010). *Atmos. Chem. Phys.*, 12, 8341-8357, 2012.
- Cusack M, Pérez N, Pey J, Alastuey A, Querol X. Source apportionment of fine PM and sub-micron particle number concentrations at a regional background site in the western Mediterranean: a 2.5 year study. *Atmos. Chem. Phys.*, 13, 5173-5187, 2013.
- Day DE, Malm WC and Kreidenweis SM. Aerosol light scattering measurements as a function of relative humidity. *J. Air & Waste Manage. Assoc.* 50:710-716, 2000.
- Delene DJ and Ogren JA. Variability of Aerosol Optical Properties at Four North American Surface Monitoring Sites. *J. Atmos. Sci.*, 59, 1135–1149, 2002.
- Draxler RR, Stunder B, Rolph G, Stein A and Taylor A. HYSPLIT4 User's Guide, NOAA Air Resources Laboratory (http://www.arl.noaa.gov/documents/reports/hysplit_user_guide.pdf, last access: February 2014), 2013.
- Drever JJ. The Geochemistry of Natural Waters. Prentice-Hall Inc, Englewood Cliffs, NJ, 437pp, 1982.
- Escríg A, Monfort E, Celades I, Querol X, Amato F, Minguillón MC, et al. Application of optimally scaled target factor analysis for assessing source contribution of ambient PM₁₀, *J Air Waste Manag Assoc.*, 59(11), 1296-307, 2009.

- Estéve AR, Ogren JA, Sheridan PJ, Andrews E, Holben BN and Utrillas MP. Sources of discrepancy between aerosol optical depth obtained from AERONET and in-situ aircraft profiles, *Atmos. Chem. Phys.*, 12, 2987-3003, 2012.
- Fan X, Chen H, Xia X, Li Z and Cribb M. Aerosol optical properties from the Atmospheric Radiation Measurement Mobile Facility at Shouxian, China, *J. Geophys. Res.*, 115, D00K33, doi:10.1029/2010JD014650, 2010.
- Fierz-Schmidhauser R, Zieger P, Wehrle G, Jefferson A, Ogren JA, Baltensperger U and Weingartner E. Measurement of relative humidity dependent light scattering of aerosols, *Atmos. Meas. Tech.*, 3, 39-50, 2010a.
- Fierz-Schmidhauser R, Zieger P, Gysel M, Kammermann L, DeCarlo PF, Baltensperger U and Weingartner E. Measured and predicted aerosol light scattering enhancement factors at the high alpine site Jungfraujoch, *Atmos. Chem. Phys.*, 10, 2319-2333, 2010b.
- Fierz-Schmidhauser R, Zieger P, Vaishya A, Monahan C, Bialek J, O'Dowd CD, Jennings SG, Baltensperger U and Weingartner E. Light scattering enhancement factors in the marine boundary layer (Mace Head, Ireland), *J. Geophys. Res.*, 115, D20204, 2010c.
- Formenti P, Andreae MO, Andreae TW, Ichoku C, Schebeske G, Kettle J, Maenhaut W, et al. Physical and chemical characteristics of aerosols over the Negev Desert (Israel) during summer 1996, *J. Geophys. Res.*, 106(D5), 4871-4890, 2001.
- Garland RM, Ravishankara AR, Lovejoy ER, Tolbert MA. and Baynard T. Parameterization for the relative humidity dependence of light extinction: Organic- ammonium sulphate aerosol, *J. Geophys. Res.*, 112, D19303, 2007.
- Gassó S, Hegg DA, Covert DS, Collins D, Noone KJ, Öström E, Schmid B et al. Influence of humidity on the aerosol scattering coefficient and its effect on the upwelling radiance during ACE-2, *Tellus*, 52B, 546-567, 2000.
- Granados-Muñoz MJ, Navas-Guzmán F, Bravo-Aranda JA, Guerrero-Rascado JL, Lyamani H, Fernández-Gálvez J, et al. Automatic determination of the planetary boundary layer height using lidar: One-year analysis over southeastern Spain, *J. Geophys. Res.*, 117, D18208, doi:10.1029/2012JD017524, 2012.
- Hand JL, Kreidenweis SM, Slusser J and Scott G. Comparisons of aerosol optical properties derived from Sun photometry to estimates inferred from surface measurements in Big Bend National Park, Texas, *Atmos. Environ.*, 38, 6813-6821, 2004.

- Hand JL and Malm WC. Review of aerosol mass scattering efficiencies from ground-based measurements since 1990, *J. Geophys. Res.*, 112, D16203, 2007.
- Harrison RM and Pio C. Size differentiated composition of inorganic aerosol of both marine and polluted continental origin. *Atmos. Environ.*, 17, 1733-1738, 1983.
- Haywood JM and Shine KP. The effect of anthropogenic sulphate and soot aerosol on the clear sky planetary radiation budget. *Geophys. Res. Lett.*, 22(5), 603-606, 1995.
- Hegg DA, Covert DS, Rood MJ. and Hobbs PV. Measurements of aerosol optical properties in marine air, *J. Geophys. Res.*, 101, D8, 12893-12903, 1996.
- Hegg DA, Covert DS, Crahan K and Jonssen H. The Dependence of Aerosol Light-Scattering on RH Over the Pacific Ocean. *Geophys. Res. Lett.*, 29(8):1219, doi:10.1029/2001GL014495, 2002.
- Hegg DA, Covert DS and Jonssond HH. Measurements of Size-Resolved Hygroscopicity in the California Coastal Zone. *Atmos. Chem. Phys.*, 8:7193-7203, 2008.
- Heintzenberg J. The angular calibration of the total scatter/backscatter nephelometer, consequences and applications. *Staub- Reinhaltung der Luft*, 38:62-63, 1978.
- Heintzenberg J, Raes F and Schwartz S. Atmospheric Chemistry in a Changing World: An Integration and Synthesis of a Decade of Tropospheric Chemistry Research: The International Global Atmospheric Chemistry Project of the International Geosphere-Biosphere Programme, Chapter 4: Tropospheric Aerosols, Springer Verlag, 2003.
- Heintzenberg J, Wiedensohler A, Tuch TM, Covert DS, Sheridan P, Ogren JA, Gras J et al. Intercomparisons and aerosol calibrations of 12 commercial integrating nephelometers of three manufacturers, *J. Atmos. Ocean. Tech.*, 23, 902-914, 2006.
- Henry RC. Multivariate Receptor Models, In: Receptor Modeling for Air Quality Management, P.K. Hopke, ed., Elsevier Science Publishers, Amsterdam, 117-147, 1991.
- Hopke PK. Receptor Modeling in Environmental Chemistry, John Wiley & Sons, Inc., New York, 1985.
- Hopke PK. Receptor Modeling for Air Quality Management, Elsevier Science, Amsterdam, 1991.
- IPCC. Contribution of Working Group I to the Fourth Assessment Report of the Intergovernmental Panel on Climate Change, edited by S. Solomon, D. Qin, M. Manning, Z. Chen, M. Marquis, K.B. Averyt, M. Tignor and H.L. Miller Cambridge University Press, 2007.

- IPCC. Contribution of Working Group I to the Fifth Assessment Report of the Intergovernmental Panel on Climate Change, in Summary for Policymakers in Climate Change, edited by T. F. Stocker, D. Qin, G.K. Plattner, M. Tignor, S. Allen, J. Boschung, A. Nauels, Y. Xia, V. Bex, and P. Midgley, Cambridge University Press, 2013.
- Jefferson A. Aerosol Observing System (AOS) Handbook, U. S. Department of Energy, DOE/SC-ARM/TR-014, (http://www.arm.gov/publications/tech_reports/handbooks/aos_handbook.pdf), 2011.
- Johnson BT, Shine KP and Forster PM. The semi-direct aerosol effect: Impact of absorbing aerosols on marine stratocumulus, Quarterly Journal of the Royal Meteorological Society, 130(599), 1407-1422, 2004.
- Jung J, Lee H, Kim YJ, Liu X, Zhang Y, Hu M and Sugimoto N. Optical properties of atmospheric aerosols obtained by in situ and remote measurements during 2006 Campaign of Air Quality Research in Beijing (CAREBeijing-2006), J. Geophys. Res., 114, D00G02, doi:10.1029/2008JD010337, 2009.
- Juntto S. and Paatero P. Analysis of daily precipitation data by positive matrix factorization, Environmetrics, 5, 127–144, 1994.
- Kassianov E, Barnard J, Pekour M, Berg LK, Fast J, Michalsky J, Lantz K and Hodges G. Temporal variability of aerosol properties during TCAP: Impact on radiative forcing, Proc. SPIE8890, doi:10.1117/12.2029355, 2013.
- Kasten F. Visibility forecast in the phase of pre-condensation, Tellus, 21(5), 631–635, 1969.
- Kirchstetter TW, Novakov T and Hobbs PV. Evidence that the spectral dependence of light absorption by aerosols is affected by organic carbon, J. Geophys. Res., 109, D21208, doi:10.1029/2004JD004999, 2004.
- Koloutsou-Vakakis S. Aerosol particle light scattering at a perturbed mid-latitude continental Northern Hemispheres site and its dependence on relative humidity, wavelength of light, particle size and composition PhD Thesis, Univ. of Illinois at Urbana-Champaign, 1996.
- Koloutsou-Vakakis S, Carrico CM, Kus P, Rood MJ, Li Z, Shrestha R, Ogren JA, et al. Aerosol properties at a midlatitude Northern Hemisphere continental site, J. Geophys. Res., 106, D3, 3019-3032, 2001.
- Kopp RE and Mauzerall DL. Assessing the climate benefits of black carbon mitigation. Proceedings of the National Academy of Sciences of the United States of America 107, 11703-11708, 2010.

- Kotchenruther RA and Hobbs PV. Humidification factors of aerosols from biomass burning in Brazil, *J. Geophys. Res.*, 103, D24, 32081-32089, 1998.
- Kotchenruther RA, Hobbs PV and Hegg DA. Humidification factors for atmospheric aerosols off the mid-Atlantic coast of the United States, *J. Geophys. Res.*, 104, D2, 2239-2251, 1999.
- Kus P, Carrico CM, Rood MJ and Williams A. Measured and Modeled Light Scattering Values for Dry and Hydrated Laboratory Aerosols, *Journal of Atmospheric and Oceanic Technology*, 21, 981-994, 2004.
- Larson TV, Ahlquist NC, Weiss RE, Covert DS and Waggoner AP. Chemical speciation of H_2SO_4 - $(\text{NH}_4)_2\text{SO}_4$ particles using temperature and humidity controlled nephelometry. *Atmos. Environ.*, 16(6):1587{1590, 1982.
- Li-Jones X, Maring HB and Propero JM. Effect of relative humidity on light scattering by mineral dust aerosol as measured in the marine boundary layer over the tropical Atlantic Ocean. *J. Geophys. Res.*, 103, D23, 31113-31121, 1998.
- Liu X, Cheng Y, Zhang Y, Jung J, Sugimoto N, Chang SY, Kim YJ et al. Influences of relative humidity and particle chemical composition on aerosol scattering properties during the 2006 PRD campaign, *Atmos. Environ.*, 42, 1525-1536, 2008.
- Lohmann U and Feichter J. Global indirect aerosol effects: a review, *Atmospheric Chemistry and Physics*, 5(3), 715-737, 2005.
- Lowenthal DH, Rogers CF, Saxena P, Watson JG and Chow JC. Sensitivity of estimated light extinction coefficients to model assumptions and measurement errors, *Atmos. Environ.*, 29, 751-766, 1995.
- Lyamani H, Olmo FJ and Alados-Arboledas L. Saharan dust outbreak over south-eastern Spain as detected by sun photometer, *Atmos. Environ.*, 39, 7276-7284, 2005.
- Lyamani H, Olmo FJ, Alcántara A, and Alados-Arboledas L. Atmospheric aerosols during the 2003 heat wave in south-eastern Spain II: Microphysical columnar properties and radiative forcing, *Atmos. Environ.*, 40, 6465-6476, 2006.
- Lyamani H, Olmo FJ and Alados-Arboledas L. Light scattering and absorption properties of aerosol particles in the urban environment of Granada, Spain, *Atmos. Environ.*, 42, 2630-2642, 2008.
- Lyamani H, Olmo FJ and Alados-Arboledas L. Physical and optical properties of aerosols over an urban location in Spain: seasonal and diurnal variability, *Atmos. Chem. Phys.*, 10, 239-254, 2010.

References

- Lyamani H, Olmo FJ, Foyo I, Alados-Arboledas L. Black carbon aerosols over an urbana rea in south-eastern Spain: Changes detected after the 2008 economic crisis. *Atmos. Environ.*, 45, 6423-6432, 2011.
- Lyamani H, Fernández-Gálvez J, Pérez-Ramírez D, Valenzuela A, Antón M, Alados I, et al. Aerosol properties over two urban sites in South Spain during an extended stagnation episode in winter season. *Atmos. Environ.*, 62, 424-432, 2012.
- Malm WC, Sisler J, Huffman D, Eldred R and Cahill T. Spatial and seasonal trends in particle concentration and optical extinction in the United States, *J. Geophys. Res.*, 99(D1), 1347–1370, doi:10.1029/93JD02916, 1994.
- Malm WC and Kreidenweis SM. The effects of models of aerosol hygroscopicity on the apportionment of extinction. *Atmos. Environ.*, 31, 13, 1965-1976, 1997.
- Malm WC and Hand JL. An examination of the physical and optical properties of aerosols collected in the IMPROVE program, *Atmos. Environ.*, 41, 3407-3427, 2007.
- Massling A, Leinert S, Wiedensohler A and Covert D. Hygroscopic growth of sub-micrometer and one-micrometer aerosol particles measured during ACE-Asia. *Atmos. Chem. Phys.*, 7, 3249–3259, doi:10.5194/acp-7-3249-2007, 2007.
- Massoli P, Bates TS, Quinn PK, Lack DA, Baynard T, Lerner BM, Tucker SC, et al. Aerosol optical and hygroscopic properties during TexAQS-GoMACCS 2006 and their impact on aerosol direct radiative forcing, *J. Geophys. Res.*, 114, D00F07, doi:10.1029/2008JD011604, 2009.
- Mather JH and Voyles JW. The Arm Climate Research Facility: A Review of Structure and Capabilities. *Bull. Amer. Meteor. Soc.*, 94, 377–392, doi: <http://dx.doi.org/10.1175/BAMS-D-11-00218.1>, 2013.
- McInnes L, Bergin M, Ogren JA and Schwartz S. Apportionment of light scattering and hygroscopic growth to aerosol composition, *Geophys. Res. Lett.*, 25, 4, 513-516, 1998.
- Meier J, Wehner B, Massling A, Birmili W, Nowak A, Gnauk T, Brüggemann E, et al. Hygroscopic growth of urban aerosol particles in Beijing (China) during wintertime: a comparison of three experimental methods. *Atmos. Chem. Phys.*, 9, 6865-6880, 2009.
- Menon S, Hansen J, Nazarenko L and Luo Y. Climate effects of black carbon aerosols in China and India, *Science*, 297(5590), 2250-2253, 2002.
- Miller MA and Slingo A. The ARM Mobile Facility and its first international deployment: Measuring Radiative Flux Divergence in West Africa. *Bull. Amer. Meteor. Soc.*, 88, 1299-1244, doi:10.1175/BAMS-88-8-1229, 2007.

- Minguillón MC, Querol X, Baltensperger U and Prévôt ASH. Fine and coarse PM composition and sources in rural and urban sites in Switzerland: Local or regional pollution?. *Sci. Total. Environ.*, 427-428, 191-202, 2012.
- Mircea M, Facchini MC, Decesari S, Cavalli F, Emblico L, Fuzzi S, Vestin A, et al. Importance of the organic aerosol fraction for modeling aerosol hygroscopic growth and activation: a case study in the Amazon Basin. *Atmos. Chem. Phys.*, 5, 3111-3126, 2005.
- Mladenov N, Alados-Arboledas L, Olmo FJ, Lyamani H, Delgado A, Molina A, Reche I. Applications of optical spectroscopy and stable isotope analyses to organic aerosol source discrimination in an urban area. *Atmos. Environ.*, 45, 11, 1960-1969, 2011.
- Müller T, Henzing JS, de Leeuw G, Wiedensohler A, Alastuey A, Angelov H, Bizjak M, et al. Characterization and intercomparison of aerosol absorption photometers: result of two intercomparison workshops. *Atmos. Meas. Tech.*, 4, 245-268, 2011.
- Nessler R, Weingartner E and Baltensperger U. Effect of humidity on aerosol light absorption and its implications for extinction and the single scattering albedo illustrated for a site in the lower free troposphere, *J. Aerosol Sci.*, 36, 958–972, 2005.
- Ogren JA. Comment on “Calibration and Intercomparison of Filter-Based Measurements of Visible Light Absorption by Aerosols”, *Aerosol Sci. Tech.*, 44:589-591, 2010.
- Orr Jr C, Hurd K and Corbett WJ. Aerosol size and relative humidity. *J. Coll. Sci.*, 13, 472-482, 1958.
- Ouimette JR and Flagan RC. The extinction coefficient of multicomponent aerosols, *Atmos. Environ.*, 16, 2405-2419, 1982.
- Paatero P and Tapper U. Positive matrix factorization: a nonnegative factor model with optimal utilization of error estimates of data values, *Environmetrics*, 5, 111–126, 1994.
- Paatero P. Least square formulation of robust non-negative factor analysis, *Chemometr. Intell. Lab. Syst.*, 3, 23–35, 1997.
- Paatero P, Hopke PK, Song X and Ramadan Z. Understanding and controlling rotations in factor analytic models, *Chemo metrics and Intelligent Laboratory Systems*, 60(1–2), 253–264, 2002.
- Paatero P and Hopke PK. Discarding or downweighting high noise variables in factor analytic models, *Anal Chim Acta*, 490, 277–289, 2003.
- Pan XL, Yan P, Tang J, Ma JZ, Wang ZF, Gbaguidi A and Sun YL. Observational study of influence of aerosol hygroscopic growth on scattering coefficient over rural area near Beijing mega-city, *Atmos. Chem. Phys.*, 9, 7519-7530, 2009.

- Pandolfi M, Viana M, Minguillón MC, Querol X, Alastuey A, Amato F, Celades I, et al. Receptor models application to multi-year ambient PM₁₀ measurements in an industrialized ceramic area: Comparison of source apportionment results. *Atmos. Environ.*, 42, 9007-9017, 2008.
- Pandolfi M, Cusack M, Alastuey A and Querol X. Variability of aerosol optical properties in the Western Mediterranean Basin, *Atmos. Chem. Phys.*, 11, 8189-8203, 2011.
- Pant P and Harrison RM. Critical review of receptor modeling for particulate matter: A case study of India. *Atmos. Environ.*, 49, 1-12, 2012.
- Pekour MS, Schmid B, Chand D, Hubbe JM, Kluzeck CD, Nelson DA, Tomlinson JM and Cziczo DJ. Development of a new airborne humidograph system. *Aerosol Science and Technology*, 47:2, 201-207, 2013.
- Pereira SN, Wagner F and Silva AM. Scattering properties and mass concentration of local and long range transported aerosols over the south western Iberian Peninsula, *Atmos. Environ.*, 42, 7623–7631, 2008.
- Pereira SN, Wagner F and Silva AM. Seven years of measurements of aerosol scattering properties, near the surface, in the southwestern Iberia Peninsula, *Atmos. Chem. Phys.*, 11, 17-29, 2011.
- Perrone MR, Becagli S, García-Orza JA, Vecchi R, Dinoi A, Udisti R, Cabello M, The impact of long-range-transport on PM₁ and PM_{2.5} at a Central Mediterranean site. *Atmos. Environ.*, 71, 176-186, 2013.
- Petzold A and Schönlinner M. Multi-angle Absorption photometry—a new method for the measurement of aerosol light absorption and atmospheric black carbon, *J. Aerosol Sci.*, 35, 421–441, 2004.
- Petzold A, Schloesser H, Sheridan PJ and Arnott WP. Evaluation of multi-angle Absorption photometry for measuring aerosol light absorption, *Aerosol Sci. Technol.*, 39(1), 40–51, 2005.
- Pey J, Pérez N, Castillo S, Viana M, Moreno T, Pandolfi M, et al. Geochemistry of regional background aerosols in the Western Mediterranean. *Atmos. Res.*, 94, 422-435, 2009.
- Pey J, Alastuey A and Querol X. PM₁₀ and PM_{2.5} sources at an insular location in the western Mediterranean by using source apportionment techniques. *Sci. Total Environ.*, 456-457, 267-277, 2013.
- Pilat MJ and Charlson RJ. Theoretical and optical studies of humidity effects on the size distribution of hygroscopic aerosol. *Journal de Recherches Atmosphériques*, 1:165-170, 1966.
- Pope CA and Dockery DW. Health effects of fine particulate air pollution: lines that connect. *J Air Waste Manage Assoc*; 56:709–42, 2006.
- Putaud JP, Van Dingenen R, Alastuey A, Bauer H, Birmili W, Cyrys J, Flentje H, et al. A European aerosol phenomenology-3: Physical and chemical

- characteristics of particulate matter from 60 rural, urban, and kerbside sites across Europe, *Atmos. Environ.*, 44, 1308–1320, 2010.
- Qadir RM, Abbaszade G, Schnelle-Kreis J, Chow JC and Zimmermann R. Concentrations and source contributions of particulate organic matter before and after implementation of a low emission zone in Munich, Germany. *Environmental Pollution*, 175, 158–167, 2013.
- Querol X, Alastuey A, Rodriguez S, Plana F, Ruiz CR, Cots N, et al. PM10 and PM2.5 source apportionment in the Barcelona Metropolitan area, Catalonia, Spain. *Atmos. Environ.*, 35, 6407–6419., 2001.
- Querol X, Alastuey A, Moreno T, Viana MM, Castillo S, Pey J, et al. Spatial and temporal variations in airborne particulate matter (PM10 and PM2.5) across Spain 1999–2005, *Atmos. Environ.*, 42:3964–3979, 2008
- Querol X, Alastuey A, Viana M, Moreno T, Reche C, Minguillon MC, Ripoll A, et al. Variability of carbonaceous aerosols in remote, rural, urban and industrial environments in Spain: implications for air quality policy. *Atmos. Chem. Phys.*, 13, 6185–6206, 2013.
- Quinn PK, Miller TL, Bates TS, Ogren JA, Andrews E and Shaw GE. A 3-year record of simultaneously measured aerosol chemical and optical properties at Barrow, Alaska, *J. Geophys. Res.*, 107(D11), 4130, 2002.
- Quinn PK, Bates TS, Baynard T, Clarke AD, Onasch TB., Wang W, et al. Impact of particulate organic matter on the relative humidity dependence of light scattering: A simplified parameterization, *Geophys. Res. Lett.*, 32, L22809, 2005.
- Quirantes A, Olmo FJ, Lyamani H and Alados-Arboledas L. Correction factors for a total scatter/backscatter nephelometer, *J. of Quantitative Spectroscopy and Radiative Transfer* 109, 1496–1503, 2008.
- Ramaswamy V, Boucher O, Haigh J, Hauglustine D, Haywood J, Myhre G, Nakajima T, et al. Radiative forcing of climate, *Climate change*, 349–416, 2001.
- Rood MJ, Larson TV, Covert DS and Ahlquist NC. Measurement of laboratory and ambient aerosols with temperature and humidity controlled nephelometry. *Atmos. Environ.*, 19(7):1181{1190, 1985.
- Rood MJ, Covert DS and Larson TV. Hygroscopic properties of atmospheric aerosol in Riverside, California. *Tellus*, 39B:383{397, 1987.
- Saha A, Mallet M, Roger JC, Dubuisson P, Piazzola J and Despiau S. One year measurements of aerosol optical properties over an urban coastal site: Effect on local direct radiative forcing, *Atmospheric Research*, 90, 195–202, 2008.

- Schauer JJ, Lough GC, Shafer MM, Christensen WF, Arndt MF and DeMinter JT. Characterization of metals emitted from motor vehicles. Health Effects Institute, 2006.
- Seinfeld JH and Pandis SN. Atmospheric Chemistry and Physics: From Air Pollution to Climate Change. Wiley, New York, 1326pp, 1998.
- Sheridan PJ and Ogren JA. Observation of the vertical and regional variability of aerosol optical properties over central and eastern North America. *J. Geophys. Res.*, 104(D14), 16793–16805, 1999.
- Sheridan PJ, Delene DJ and Ogren JA. Four years of continuous surface aerosol measurements from the Department of Energy's Atmospheric Radiation Measurement Program Southern Great Plains Cloud and Radiation Testbed site. *J. Geophys. Res.*, 106, D18, 20735-20747, 2001.
- Sheridan PJ, Jefferson A and Ogren JA. Spatial variability of submicrometer aerosol radiative properties over the Indian Ocean during INDOEX. *J. Geophys. Res.*, 107, D19, 8011, 2002.
- Sheridan PJ, Andrews E, Ogren JA, Tackett JL and Winker DM. Aerosol profiles of aerosol optical properties over central Illinois and comparison with surface and satellite measurements. *Atmos. Chem. Phys.*, 12, 11695-11721, 2012.
- Shinozuka Y, Johnson RR, Flynn CJ, Russell PB, Schmid B, Redemann J, Dunagan SE, et al. Hyperspectral aerosol optical depths from TCAP flights. *J. Geophys. Res.*, Accepted, doi: 10.1002/2013JD020596, 2013.
- Sjogren S, Gysel M, Weingartner E, Baltensperger U, Cubison MJ, Coe H, Zardini AA, et al. Hygroscopic growth and water uptake kinetics of two-phase aerosol particles consisting of ammonium sulphate, adipic and humic acid mixtures. *J. of Aerosol Sci.*, 38:157{171, 2007.
- Sloane CS. Optical properties of aerosols of mixed composition. *Atmos. Environ.*, 18:871{878, 1984.
- Song S, Wu Y, Jiang J, Yang L, Cheng Y and Hao J. Chemical characteristics of size-resolved PM_{2.5} at a roadside environment in Beijing, China. *Environmental Pollution*, 161, 215-221, 2012.
- Tang IN and Munkelwitz HR. Composition and temperature dependence of the deliquescence properties of hygroscopic aerosols. *Atmos. Environ.*, 27A, 467–473, 1993.
- Tang IN. Chemical and size effects of hygroscopic aerosols on light scattering coefficients. *J. Geophys. Res.*, 101, 19245-19250, 1996.
- Tauler R, Viana M, Querol X, Alastuey A, Flight RM, Wentzell PD and Hopke PK. Comparison of the results obtained by four receptor modelling methods in aerosol source apportionment studies. *Atmos. Environ.*, 43, 3989-3997, 2009.

- ten Brink HM, Khlystov A, Kos GPA, Tuch T, Roth C and Kreyling W. A high flow humidograph for testing the water uptake by ambient aerosol. *Atmos. Environ.*, 34, 4291–4300, 2000.
- Thompson M and Howarth RJ. Duplicate analysis in geochemical practice. Part I. Theoretical approach and estimation of analytical reproducibility. *Analyst* 101, 690–698, 1978.
- Thompson M. Variation of precision with concentration in an analytical system. *Analyst* 113 (10), 1579–1587, 1988.
- Thurston GD and Spengler JD. A quantitative assessment of source contributions to inhalable particulate matter pollution in metropolitan Boston. *Atmos. Environ.*, 19 (1), 9–25, 1985.
- Tobo Y, Zhang D, Matsuki A and Iwasaka Y. Asian dust particles converted into aqueous droplets under remote marine atmospheric conditions. *PNAS*, 107(42): 17905–17910, 2010.
- Toon OB, Pollack JB and Khare BN. Optical-constants of several atmospheric aerosol species - ammonium-sulphate, aluminium-oxide, and sodium-chloride. *J. Geophys. Res.*, 81(33):5733-5748, 1976.
- TSI. Model 3563 integrating nephelometer; operation and service manual. Technical report, TSI Incorporated, 2009.
- Turpin BJ, Saxena P and Andrews E. Measuring and simulating particulate organics in the atmosphere: Problems and prospects, *Atmos. Environ.*, 34, 2983–3013, doi:10.1016/S1352-2310(99)00501-4, 2000.
- Valenzuela A, Olmo FJ, Lyamani H, Antón M, Quirantes A and Alados-Arboledas L. Classification of aerosol radiative properties during African desert dust intrusions over southeastern Spain by sector origins and cluster analysis. *J. Geophys. Res.*, doi:10.1029/2011JD016885, 2012.
- Vasconcelos LA de P, Macias ES, McMurry PH, Turpin BJ and White WH., A closure study of extinction apportionment by multiple regression, *Atmos. Environ.*, 35, 151-158, 2001.
- Viana M, Pandolfi M, Minguillón MC, Querol X, Alastuey A, Monfort E, et al. Inter-comparison of receptor models for PM source apportionment: Case study in an industrial area, *Atmos. Environ.*, 42, 3820–3832, 2008a.
- Viana M, Kuhlbusch TAJ, Querol X, Alastuey A, Harrison RM, Hopke PK, et al. Source apportionment of particulate matter in Europe: a review of methods and results. *J. of Aerosol Sci.*, 39, 827–849, 2008b.
- Virkkula A, Backman J, Aalto PP, Hulkkoen M, Riuttanen L, Nieminen T, dal Maso M, et al. Seasonal Cycle, size dependencies, and source analyses of aerosol optical properties at the SMEAR II measurement station in Hyytiälä, Finland, *Atmos. Chem. Phys.*, 11, 4445-4468, 2011.

- Vrekoussis M, Liakakou E, Koçak M, Kubilay N, Oikonomou K, Sciare J and Mihalopoulos N. Seasonal variability of optical properties of aerosols in the Eastern Mediterranean, *Atmos. Environ.*, 39, 7083–7094, 2005.
- Wagner F, Bortoli D, Pereira S, Costa MJ, Silva AM, Weinzierl B, Esselborn M, et al. Properties of dust aerosol particles transported to Portugal from the Sahara desert, *Tellus*, 61B, 297–306, 2009.
- Wahlin P. COPREM – a multivariate receptor model with a physical approach, *Atmos. Environ.*, 37, 4861–4867, 2003.
- Wahlin P, Berkowicz R and Palmgren F. Characterization of traffic-generated particulate matter in Copenhagen. *Atmos. Environ.*, 40, 2151–2159, 2006.
- Wang J and Martin ST. Satellite characterization of urban aerls: Importance of including hygroscopicity and mixing state in the retrieval algorithms. *J. Geophys. Res.*, 112, D17203, doi:10.1029/2006JD008078, 2007.
- Weingartner E, Burtscher H and Baltensperger U. Hygroscopic properties of carbon and diesel soot particles. *Atmos. Environ.*, 31(15):2311{2327, 1997.
- Whitby K. and Cantrell B. Fine particles, in International Conference on Environmental Sensing and Assessment, Las Vegas, NV, Institute of Electrical and Electronic Engineers, 1976.
- White WH. On the theoretical and empirical basis for apportioning extinction by aerosols: A critical review, *Atmos. Environ.*, 20, 1659–1672, 1986.
- White WH and Macias ES. On measurement error and the empirical relationship of atmospheric extinction to aerosol composition in the non-urban west. In APCA Transactions 10: Visibility protection (edited by Bhardwaja PS). Air Pollution Control Association, Pittsburgh, PA; 1987.
- White WH, Macias ES, Nininger RC and Schorran D. Size-resolved measurements of light scattering by ambient particles in the southwestern U.S.A, *Atmos. Environ.*, 28, 909–921, 1994.
- Wiscombe WJ and Grams GW. The backscattered fraction in two-stream approximations. *J. Atmos. Sci.*, 33, 2440–2451, 1976.
- WMO/GAW. Aerosol measurement procedures guidelines and recommendations. GAWRep. 153, World Meteorol. Organ., Geneva, Switzerland, available at: <ftp://ftp.wmo.int/Documents/PublicWeb/arep/gaw/gaw153.pdf> (last access: February 2014), 2003.
- Wu A, Birmili W, Poulain L, Wang Z, Merkel M, Fahlbusch B, van Pinxteren D, et al. Particle hygroscopicity during atmospheric new particle formation events: implications for the chemical species contributing to particle growth. *Atmos. Chem. Phys.*, 13, 6637–6646, 2013.
- Yan H. Aerosol scattering properties in northern China, *Atmos. Environ.*, 41, 6916–6922, 2007.

- Yan P, Pan X, Tang J, Zhou X, Zhang R and Zeng L. Hygroscopic growth of aerosol scattering coefficient: A comparative analysis between urban and suburban sites at winter in Beijing. *Particuology*, 7, 52-60, 2009.
- Zieger P, Fierz-Schmidhauser R, Gysel M, Ström J, Henne S, Yttri K, Baltensperger U and Weingartner E. Effects of relative humidity on aerosol light scattering in the Arctic, *Atmos. Chem. Phys.*, 10(8), 3875–3890, doi:10.5194/acp-10-3875-2010, 2010.
- Zieger P, Weingartner E, Henzing J, Moerman M, de Leeuw G, Mikkilä J, Ehn M, et al. Comparison of ambient aerosol extinction coefficients obtained from in-situ, MAX-DOAS and LIDAR measurements at Cabauw, *Atmos. Chem. Phys.*, 11, 2603-2624, 2011.
- Zieger P. Effects of relative humidity on aerosol light scattering. PhD Thesis. Diss. ETH No. 19659, 2011.
- Zieger P, Kienast-Sjögren E, Starace M, von Bismarck J, Bukowiecki N, Baltensperger U, Wienhold F, et al. Spatial variation of aerosol optical properties around the high-alpine site Jungfraujoch (3580 m a.s.l.), *Atmos. Chem. Phys.*, 12, 7231–7249, doi: 10.5194/acp-12-7231-2012, 2012.
- Zieger P, Fierz-Schmidhauser R, Weingartner E and Baltensperger U. Effects of relative humidity on aerosol light scattering: results from different European sites. *Atmos. Chem. Phys.* 13, 10609-10631, 2013.
- Zieger P, Fierz-Schmidhauser R, Poulain L, Müller T, Birmili W, Spindler G, Wiedensohler A, et al. Influence of water uptake on the aerosol particle light scattering coefficients of the Central European aerosol. *Tellus B*, 66, 22716, <http://dx.doi.org/10.3402/tellusb.v66.22716>, 2014.

List of scientific contributions

Articles in peer-reviewed journals

- 2014 Study of the relative humidity dependence of aerosol light-scattering in southern Spain**
Tellus B, 66, 24536
Titos G., H. Lyamani, A. Cazorla, M. Sorribas, I. Foyo-Moreno, A. Wiedensohler and L. Alados-Arboledas
- 2014 Aerosol light-scattering enhancement due to water uptake during the TCAP campaign**
Atmospheric Chemistry and Physics, 14, 7031–7043.
Titos G., Jefferson A., Sheridan P. J., Andrews E., Lyamani H., Alados-Arboledas L. and Ogren J.A.
- 2014 Aerosol light-scattering enhancement due to water uptake during TCAP campaign**
Atmospheric Chemistry and Physics Discussion, 14, 3361-3393.
Titos G., Jefferson A., Sheridan P. J., Andrews E., Lyamani H., Alados-Arboledas L. and Ogren J.A.
- 2014 Identification of fine (PM1) and coarse (PM10-1) sources of particulate matter in an urban environment**
Atmospheric Environment, 89, 593-602.
Titos G., Lyamani H., Pandolfi, M., Alastuey A., and Alados-Arboledas L.
- 2014 Determination and analysis of spectral aerosol optical properties by a multi-instrumental approach**
Atmospheric Measurement Techniques, 7, 2373–2387
Segura S., V. Estellés, **G. Titos**, H. Lyamani, M.P. Utrillas, P. Zotter, A.S.H. Prévôt, G. Močnik, L. Alados-Arboledas, and J.A. Martínez-Lozano
- 2014 Determination and analysis of spectral aerosol optical properties by a multi-instrumental approach**
Atmospheric Measurement Techniques Discussion, 7, 2373–2387
Segura S., V. Estellés, **G. Titos**, H. Lyamani, M.P. Utrillas, P. Zotter, A.S.H. Prévôt, G. Močnik, L. Alados-Arboledas, and J.A. Martínez-Lozano.

2014 Hygroscopic growth of atmospheric aerosols based on active remote sensing and radiosounding measurements

Atmospheric Measurement Techniques Discussion, 7, 10293-10326.

Granados-Muñoz M. J., F. Navas-Guzmán, J. A. Bravo-Aranda, J. L. Guerrero-Rascado, H. Lyamani, A. Valenzuela, **G. Titos**, J. Fernández-Gálvez and L. Alados-Arboledas

2014 Aerosol scattering and absorption Ångström exponent as indicators of dust and dust-free days over Granada (Spain)

Atmospheric Research (accepted)

Valenzuela A, F.J. Olmo, H. Lyamani, M. Antón, **G.Titos**, A. Cazorla and L. Alados-Arboledas

2014 Study of mineral dust entrainment in the planetary boundary layer by lidar depolarization technique

Tellus B (submitted)

Bravo-Aranda J. A., **G. Titos**, M. J. Granados-Muñoz, J.L. Guerrero-Rascado, F. Navas Guzmán, A. Valenzuela, H. Lyamani, F.J. Olmo, J. Andrey, and L. Alados-Arboledas

2014 Study of aerosol microphysical properties profiles retrieved from ground-based remote sensing and aircraft in-situ measurements during a Saharan dust event

Atmospheric Chemistry and Physics (submitted)

Granados-Muñoz M. J., J.A. Bravo-Aranda, J.L. Guerrero-Rascado, D. Pérez-Ramírez, F. Navas Guzmán, I. Veselovskii, H. Lyamani, A. Valenzuela, F.J. Olmo, **G. Titos**, J. Andrey, A. Chaikovsky, O. Dubovik and L. Alados-Arboledas.

2013 Variability of carbonaceous aerosols in remote, rural, urban and industrial environments in Spain: implications for air quality policy

Atmospheric Chemistry and Physics, 13, 6185–6206

Querol, X., A. Alastuey, M. Viana, T. Moreno, C. Reche, M. C. Minguillon, A. Ripoll, M. Pandolfi, F. Amato, A. Karanasiou, N. Perez, J. Pey, M. Cusack, R. Vazquez, F. Plana, M. Dall’Osto, J. de la Rosa, A. Sanchez de la Campa, R. Fernandez-Camacho, S. Rodriguez, C. Pio, L. Alados-Arboledas, **G. Titos**, B. Artiñano, P. Salvador, S. Garcia Dos Santos, and R. Fernandez Patier

- 2013 Variability of carbonaceous aerosols in remote, rural, urban and industrial environments in Spain: implications for air quality policy**
Atmospheric Chemistry and Physics Discussion, 13, 6971–7019
Querol, X., A. Alastuey, M. Viana, T. Moreno, C. Reche, M. C. Minguillon, A. Ripoll, M. Pandolfi, F. Amato, A. Karanasiou, N. Perez, J. Pey, M. Cusack, R. Vazquez, F. Plana, M. Dall’Osto, J. de la Rosa, A. Sanchez de la Campa, R. Fernandez-Camacho, S. Rodriguez, C. Pio, L. Alados-Arboledas, **G. Titos**, B. Artíñano, P. Salvador, S. García Dos Santos, and R. Fernandez Patier
- 2012 Aerosol properties over two urban sites in South Spain during an extended stagnation episode in winter season**
Atmospheric Environment, 62, 424-432
Lyamani H., J. Fernández-Gálvez, D. Pérez-Ramírez, A. Valenzuela, M. Antón, I. Alados, **G. Titos**, F.J. Olmo and L. Alados-Arboledas
- 2012 Optical properties and chemical composition of aerosol particles at an urban location: An estimation of the aerosol mass scattering and absorption efficiencies**
Journal of Geophysical Research, 117, D04206.
Titos, G., I. Foyo-Moreno, H. Lyamani, X. Querol, A. Alastuey, and L. Alados-Arboledas

Books

- 2013 Medioambiente: partículas ultrafinas y sus instrumentos de medida**
Editorial INTA, ISBN 978-84-938932-1-1
Gómez-Moreno F. J., M. Sorribas, E. Alonso, B. Artíñano, V. Juncal Bello, M. Piñeiro Iglesias, P. López Mahía, N. Pérez, J. Pey, A. Alastuey, M. I. García, S. Rodríguez, **G. Titos**, H. Lyamani, L. Alados-Arboledas and B.A. de la Morena

Book chapters

- 2011 Aerosol chemical and optical properties in Granada: Analysis of the aerosol mass scattering and absorption efficiencies**
Book of extended abstracts of V Reunión Española de Ciencia y Tecnología de Aerosoles, ISBN: 978-84-7834-662-2
Titos G., Foyo-Moreno I., Lyamani H., Querol X., Alastuey A. and Alados-Arboledas L.

2010 Estimating absorption and scattering efficiencies for particulate matter PM10 at an urban site

Book of extended abstracts of IV Reunión Española de Ciencia y Tecnología de Aerosoles, ISBN: 978-84-693-4839-0

Titos G., Foyo-Moreno I., Lyamani H., Querol X., Alastuey A. and Alados-Arboledas L.

Conference proceedings

2014 Estimating aerosol light-scattering enhancement from dry aerosol optical properties at different sites

Oral. European Geosciences Union General Assembly, Vienna

Titos G., Jefferson A., Sheridan P. J., Andrews E., Lyamani H., Ogren J.A. and Alados-Arboledas L.

2014 Results of aerosol hygroscopicity during TCAP campaign in the frame of the NOAA network

Poster. NOAA-ESRL Global Monitoring Annual Conference. Boulder (Colorado)

Titos G., Jefferson A., Sheridan P. J., Andrews E., Alados-Arboledas L. and Ogren J.A.

2014 Determination and analysis of spectral aerosol optical properties by a multi-instrumental approach

Poster. International Aerosol Conference, Busan

Segura S., V. Estellés, **G. Titos**, H. Lyamani, M.P. Utrillas, P. Zotter, A.S.H. Prévôt, G. Močnik, L. Alados-Arboledas, and J.A. Martínez-Lozano

2014 The REDMAAS 2014 intercomparison campaign: cpc, smps, ufp and neutralizers

Poster. II Iberian Meeting on Aerosol Science and Technology. Tarragona

Gómez-Moreno F.J., E. Alonso, B. Artíñano, S. Iglesias Samitier, M. Piñeiro Iglesias, P. López Mahía, N. Pérez, A. Alastuey, B. A. De La Morena, M. I. García, S. Rodríguez, M. Sorribas, **G. Titos**, H. Lyamani, L. Alados-Arboledas, E. Filimundi And E. Latorre Tarrasa

2013 Measurements of aerosol light-scattering enhancement factors at the urban environment of Granada (Spain)

Poster. European Aerosol Conference. Prague

Titos G., H. Lyamani, A. Cazorla, Z.J. Wu, M. Sorribas, I. Foyo-Moreno, J. Cheng, H.J. Liu, A. Wiedensohler and L. Alados-Arboledas.

- 2013 Study of the diurnal evolution of the aerosol mass scattering and absorption efficiencies at the urban environment of Granada (Spain)**
Poster. European Aerosol Conference. Prague
del Águila A., **Titos G.**, Lyamani H., Cazorla A., and Alados-Arboledas L.
- 2013 Relating the wavelength dependency of the absorption coefficient and the aerosol type**
Poster. European Aerosol Conference. Prague
Cazorla A., **Titos G.**, Lyamani H., and Alados-Arboledas L.
- 2013 On the microphysical and optical aerosol properties during AMISOC-ARN campaign**
Poster. European Aerosol Conference. Prague
Sorribas M., C. Córdoba-Jabonero, H. Lyamani, **G. Titos**, J.A. Adame, R. Fraile, B.A. de la Morena, F.J. Olmo, L. Alados-Arboledas, O. Puentedura, and M. Gil.
- 2013 The Spanish network on environmental DMAs: the 2012 SMPS+UFP intercomparison campaign and study on particle losses in dryers**
Poster. European Aerosol Conference. Prague
Gómez-Moreno F.J., E. Alonso, B. Artíñano, V. Juncal Bello, M. Piñeiro Iglesias, P. López Mahía, N. Pérez, J. Pey, A. Alastuey, B. A. de la Morena, M. I. García, S. Rodríguez, M. Sorribas, **G. Titos**, H. Lyamani and L. Alados-Arboledas.
- 2013 Effects of relative humidity on aerosol light-scattering coefficient in Granada (Spain) during winter season**
Poster. I Iberian Meeting on Aerosol Science and Technology
Titos G., H. Lyamani, A. Cazorla, Z.J. Wu, M. Sorribas, I. Foyo-Moreno, J. Cheng, H.J. Liu, A. Wiedensohler and L. Alados-Arboledas.
- 2013 Relating the wavelength dependency of the absorption coefficient and the aerosol source with aethalometer**
Poster. I Iberian Meeting on Aerosol Science and Technology
Cazorla A., **Titos G.**, Lyamani H., and Alados-Arboledas L.

2013 Time and size resolved characterization of in-situ surface aerosol during AMISOC-ARN Campaign: Microphysical and optical aerosol properties

Poster. I Iberian Meeting on Aerosol Science and Technology

Sorribas M., C. Córdoba-Jabonero, H. Lyamani, **G. Titos**, J.A. Adame, R. Fraile, B.A. de la Morena, F.J. Olmo, L. Alados-Arboledas, O. Puentedura, and M. Gil.

2013 The REDMAAS 2012 SMPS+UFP intercomparison campaign

Poster. I Iberian Meeting on Aerosol Science and Technology

Gómez-Moreno F.J., E. Alonso, B. Artíñano, V. Juncal Bello, M. Piñeiro Iglesias, P. López Mahía, N. Pérez, J. Pey, A. Alastuey, B. A. de la Morena, M. I. García, S. Rodríguez, M. Sorribas, **G. Titos**, H. Lyamani and L. Alados-Arboledas.

2012 CLIMARENO 2011 campaign: a multi-instrumental characterization of a Saharan dust intrusion over the Iberian Peninsula by airborne and ground based instrumentation

Poster. European Aerosol Conference. Granada

Andrey J., Fernández-Gálvez J., Guerrero-Rascado J.L., Sorribas M., **Titos G.**, Corrales-Sierra A., Gil-Ojeda M., Cachorro V., de la Morena B., Olmo F.J. and Alados-Arboledas L.

2012 Calibration and intercomparison results in the Spanish network on environmental DMAs

Poster. European Aerosol Conference. Granada

Gómez-Moreno F. J., Artíñano B., Juncal Bello V., Piñeiro Iglesias M., López Mahía P., Pérez N., Pey J., Alastuey A., de la Morena B. A., García M. I., Rodríguez S. , Sorribas M., **Titos G.**, Lyamani H., and Alados-Arboledas L.

2012 CLIMARENO campaign 2011: Aerosol optical properties characterization from ground-based instrumentation

Poster. European Aerosol Conference. Granada

Bravo-Aranda J.A., Navas-Guzmán F., Andrey J., Granados-Muñoz M.J., Guerrero-Rascado J.L., Gil M., Lyamani H., Valenzuela A., **Titos G.**, Fernández-Gálvez J., Olmo F.J., and Alados-Arboledas L.

2012 Source apportionment of ambient PM₁₀₋₁ and PM₁ in Granada

Poster. European Aerosol Conference. Granada

Titos G., Lyamani H., Alastuey A., Pandolfi M., and Alados-Arboledas L.

- 2012 Monitoring of ultrafine particles at an urban environment in southern Europe**
Poster. European Aerosol Conference. Granada
Titos G., Lyamani H., Sorribas M., Foyo-Moreno I., and Alados-Arboledas L.
- 2012 Levels of carbonaceous aerosols in remote, rural, urban and industrial sites of Spain**
Oral. European Aerosol Conference. Granada
Querol X., Alastuey A., Viana M., Moreno T., Reche C., Minguillón M.C., Ripoll A., Pandolfi M., Amato F., Pérez N., Pey J., Cusack M., Vázquez R., de la Rosa J., Sánchez de la Campa A., Rodriguez S., Pío C., Alados-Arboledas L., **Titos G., Atíñano B., Salvador P., García Dos Santos S., and Fernández Patier R.**
- 2011 Optical and chemical properties of aerosol particles over an urban location. Estimating mass scattering and absorption efficiencies**
Poster. European Aerosol Conference. Manchester
Titos G., Foyo-Moreno I., Lyamani H., Querol X., Alastuey A. and Alados-Arboledas L.
- 2011 Aerosol chemical and optical properties in Granada: Analysis of the aerosol mass scattering and absorption efficiencies**
Poster. V Spanish Meeting on Aerosol Science and Technology. Madrid,
Titos G., Foyo-Moreno I., Lyamani H., Querol X., Alastuey A. and Alados-Arboledas L.
- 2010 Estimating absorption and scattering efficiencies for particulate matter PM10 at an urban site**
Poster. IV Spanish Meeting on Aerosol Science and Technology. Granada,
Titos G., Foyo-Moreno I., Lyamani H., Querol X., Alastuey A. and Alados-Arboledas L.